Experiments for Evaluating 3-D Effects on Cracks in Frozen Stress Models

Jason D. Hansen

Thesis submitted to the faculty of the Virginia Polytechnic Institute and State University
in partial fulfillment of the requirements for the degree of

Master of Science
in
Engineering Mechanics

Prof. N.E. Dowling
Prof. C.W. Smith
Prof. R.D. Kriz
Prof. S. Thangjitham

April 29, 2004
Blacksburg, VA

Keywords: Frozen Stress, Photoelasticity, Motor Grain, Fracture Mechanics

Experiments for Evaluating 3-D Effects on Cracks in Frozen Stress Models

Jason D. Hansen

Abstract

In the experimental work conducted, two cases have been considered for the six-finned internal star cylinder: the semi-elliptic natural crack and a machined V-cut crack extending the length of the cylinder, both originating from the axis of symmetry of the fin tip. The V-cut crack constitutes a plane strain approximation and is used in current design rationale. Results show that the normalized stress intensity factor (SIF) for the V-cut case are at least equal to, but in most cases are greater than, the natural crack cases. These results were compared to experimental results from Smith and his associates for motor grains having similar shaped off-axis cracks, and similar trends were achieved. Comparisons were also made between the natural crack models and the modified boundary element method of Guozhong, Kangda, and Dongdi (GKD) for a semi-elliptic crack in a circular cylinder and the V-cut crack models to the modified mapping collocation technique of Bowie and Freese (BF), which constitutes the plane strain solution to a circular cylinder with a crack extending the length of the bore. For both cases general trends were similar. Using the numerical results, a relation for estimating the plane strain SIF for the finned cylinder models was developed. The situation of a finned cylinder containing a crack the length of the bore constitutes the worst case scenario. Testing has shown, however, that under normal loading conditions this case is conservative. Penetration tests have shown that a crack penetrating the outer boundary retains its semi-elliptic shape, thus the use of a semi-elliptic crack in design more accurately represents reality.

Table of Contents

List of Figures

List of Tables

1 Introduction

Solid rocket propellant is used in a wide range of applications including Department of Defense/NASA launch vehicles (e.g., Titan V) and missiles of all sizes. Solid rocket motors are made of a composite consisting of a rubbery material suspended in a fuel/oxidizer matrix. This type of propellant is an attractive alternative when compared to its competition, liquid propelled rockets. This is due to their relative simplicity, low service requirements, and stability. However, once the propellant grain is cast, they are not easy to inspect prior to use, which can lead to performance issues and even failure.

Operational capabilities of solid rocket propellant are defined in terms of thrust. Factors that affect the thrust are geometric configuration and propellant material [7]. For a given material, the geometry determines the burn rate of the propellant. Over many years, the maximization of burn rate has led to several common configurations fulfilling many application needs. Figure 1.1 shows a schematic of typical grain configurations [32]. Of these geometries, the internal star configuration is common and fulfills many solid rocket application needs. This is due to its relatively neutral burn rate and the fact that it, to some extent, satisfies the conflicting relationship between burn rate and burning surface area.

As design work has been performed, the mechanical characteristics for different loading conditions, both 2- and 3-D, have been analyzed in order to avoid excessive stresses that cause failure [10, 24, 36]. The extension of mechanical analysis to fracture in propellant grains with surface cracks has had limited consideration. This is due to the fact that the problem becomes much more complicated when a crack is introduced into the grain, because the crack causes difficulty in predicting stress redistribution. Fracture, however, constitutes a very important problem in motor grain design, since propellant grains not only provide thrust, but also act as a structural member.

Grains with flaws have been found to work properly. As a result, conditions limiting performance and structural safety must be defined with the help of fracture mechanics in order to determine service life predictions. Conditions known to cause structural flaws are unsuitable grain design; low viscoelastic strength/elongation; imperfections in manufacturing; and accumulated stresses during storage, handling, and transportation.

During ignition, burning begins at the grain inner surface and proceeds in a somewhat linear fashion outward. High pressures are produced internally during this process. As a result, the affect of an internal flaw is 1) to provide greater surface area for burning, thus altering the burn pattern and the ballistics and/or 2) to rapidly grow under pressure until grain failure occurs. A third case is also possible. In this case, the crack size is sub-critical, and neither of the above failure conditions occurs. Therefore, a critical flaw size must be determined, where a critical flaw is defined as one adversely affecting ballistics. Determining what is or is not an acceptable flaw can result in considerable cost savings.

To date, analytic solutions to cracks in complex motor grain configurations are not available, and solutions that do exist to similar complex problems (cracks in a circular cylinder) need a means of validation. Therefore, experimental work plays an important role in the analysis of complex geometries such as motor grains. When studying a cracked body, the stress intensity factor (SIF) must be determined. Experimentally, a well-known 3-D method for accomplishing this is frozen stress photoelasticity. In later chapters, use of this method to determine the SIF of cracks in rocket motor grains will be described in detail.

For the experimental work conducted, two cases have been considered for the internal star circular cylinder. First is the symmetric (semi-elliptic) natural crack emanating from a fin tip, and second is a machined crack extending the length of the cylinder, also emanating from a fin tip. The second case constitutes a plane strain approximation and is used in current design rationale, even though computational analysis and tensile testing has shown that a crack is most likely to originate at the coalescence of the fin tip end radius with a small radius connecting the fin tip end radius

with the side of the fin [28]. A crack located at this location is known as an off axis crack. A schematic of the fin tip with cracks on and off the fin axis is shown in Figure 1.2.

The results obtained from the symmetric natural and machined cracks will be compared to experimental results from Smith and his associates for motor grains having similar shaped off axis cracks. Also, comparisons will be drawn from analytical solutions to both semi-elliptic cracks and through cracks in circular cylinders with similar crack aspect ratios, a/c, and radius ratios, R_o/R_i. From these results, current design rationale will be re-evaluated to determine if current criteria are acceptable.

2 Literature Review

Surface cracks are often found in cylindrical objects such as pressure vessels, pipes, and solid rocket motor grains. Therefore the determination of the SIF for use in failure analysis has practical importance. However, the 3-D geometric complexity of the problem makes finding an exact solution impossible. Many resulting analytical methods have been developed, providing adequate solutions to this problem. Some of these methods will be discussed in this chapter.

2.1 Analytical Methods for Determining Mode I SIF in Circular Cylinders

2.1.1 Weight Functions [19, 3, 25, 26, 38, 39]

A weight function is a property of a cracked geometry that is independent of loading [3, 25]. The weight function can be derived from relations between the stress intensity factor K and the strain energy release rate G. In general, the SIF in terms of the weight function $\underline{m}$ is

$$K_I^* = \int_\Gamma \underline{t} \cdot \underline{m} d\Gamma + \int_A \underline{f} \cdot \underline{m} dA \qquad 2.1$$

with

$$\underline{m} = m(x, y, a) = \frac{H}{2K} \frac{\partial \underline{u}}{\partial a} \qquad 2.2$$

where $\underline{u}$ is the displacement field, $\underline{t}$ is the stress vector acting on boundary Γ, $\underline{f}$ is the body force acting within the region A, a is the crack length, and H is a material constant.

Therefore, if the displacement field and a SIF are known for a reference loading situation, the weight function can be obtained, and the new SIF, K_I*, can be determined for any other loading situation. This is only true if the new loading case shares the same geometric symmetries as the reference loading.

Glinka and Shen [26] found that a general form of the weight function exists for many 1-D crack problems, which can be expressed as

$$m_A(x,a) = \frac{2}{\sqrt{2\pi(a-x)}}[1 + M_{1A}\left(1-\frac{x}{a}\right)^{1/2} + M_{2A}\left(1-\frac{x}{a}\right) + M_{3A}\left(1-\frac{x}{a}\right)^{3/2}] \qquad 2.3$$

where M_{1A}, M_{2A}, and M_{3A} are parameters that must be solved by using two known reference SIFs and a property of the weight function, namely

$$K_{R_iA} = \int_0^a m_A(x,a)\sigma_i(x)dx \qquad for \qquad i = 1,2 \qquad 2.4$$

and

$$\left.\frac{\partial^2 m_A(x,a)}{\partial x^2}\right|_{x=0} = 0 \qquad 2.5$$

This solution has been extended to determine the SIF of internal semi-elliptical surface flaws in thick-walled cylindrical bodies [38, 39]. The parameters (M_{iA}) were determined by simultaneously solving equations 2.4 and 2.5 with the reference SIF determined from finite element (FE) solutions of uniform and linearly varying stress fields (Figure 2.1a). The weight function was then used to determine the SIF of a cracked cylindrical body with internal pressure p subjected to the Lame tangential stress distribution σ_L shown in Figure 2.1b for crack geometries of R_i/t = 2 and 4, a/c ranging from 0.2 to 1.0, and a/t varying from 0 to 0.8. When compared to the finite element results of Atluri and Kathiresan [1] and the boundary element method results of Guozhong, Kangda, and Dongdi (GKD) [9], data are in good agreement for a/t less than 0.6. However,

discrepancies exist for a/t greater than 0.6, with the discrepancy growing larger as a/c approaches zero.

2.1.2 Finite Element Method (FEM) [19, 1, 23, 13]

The FEM is a technique in which a continuous geometry is replaced with discrete volume elements that are connected at nodal points [19]. Compatibility conditions are then imposed at these points, and equilibrium is satisfied using energy minimization techniques. FEM reduces the problem to one with a limited number of degrees of freedom as opposed to infinite degrees of freedom. In this method, material properties are used to determine individual element stiffness matrices, which in turn are combined into a global stiffness matrix. Boundary conditions are then imposed to find unknown forces and displacements, and the SIF is determined from derived stresses or displacements around the crack tip.

Atluri and Kathiresan [1] used a 3-D displacement-hybrid FEM to determine the SIF along the crack border for semi-elliptical cracks in thick-walled cylinders. The method uses a modified variationial principal of the total potential energy with arbitrary element interior displacements, interelement boundary displacements, and element boundary tractions as variables. In this method, the SIF is calculated directly by using the exact asymptotic solution for singular stresses and strains in elements near the crack boundary, while using regular polynomial type functions in elements far from the crack with interelement continuity maintained. The test geometry was as follows: a/c = 0.2 and 1, a/t = 0.5 and 0.8, Ro/Ri = 1.5 and 2.0, and $L/2a$ (and L/Ro) $\geq$ 3 with a Poisson's ratio of ν = 0.3. The maximum value of the SIF occurs where the crack front and inner wall meet. Comparisons to Kobayashi's 2-D results differ greatly for $\theta < \pi/4$, where θ is measured from the surface, but are in good agreement otherwise.

Raju and Newman [23] used a 3-D FEM with 6,500 degrees of freedom consisting of singular elements along the crack front and linear strain elements elsewhere. In their solution, the stress intensity variations along the crack front of an internal semi-elliptical crack in a circular cylinder were determined. The geometry used is as follows: a/c = 0.2 to 0.1, a/t = 0.2 to 0.8, and t/R_i = 0.1 and 0.25. SIF influence coefficients (G_j)

were determined for crack surfaces subjected to uniform, linear, quadratic, and cubic stress distributions. The SIF for a flawed circular cylinder subjected to internal pressure was obtained through direct superposition of the SIF influence coefficients with

$$K_I = \frac{PR_i}{t}\sqrt{\pi\frac{a}{Q}}F_i\left(\frac{a}{c},\frac{a}{t},\frac{t}{R_i},\phi\right) \qquad 2.6$$

where PR_i/t is the average hoop stress, F_i is the boundary correction factor, c is the half crack length, and Q is the square of the complete elliptic integral of the second kind (this will be defined and discussed in section 3.4). The expression for F_i as a function of G_j was obtained from the first four terms of a power series expansion of Lame's solution

$$F_i = \frac{t}{R_i}\left(\frac{R_o^{\,2}}{R_o^{\,2}-R_i^{\,2}}\right)\left(2G_0 - 2\left(\frac{a}{R_o}\right)G_1 + 3\left(\frac{a}{R_o}\right)^2 G_2 - 4\left(\frac{a}{R_o}\right)^3 G_3\right) \qquad 2.7$$

For the range of data presented, the normalized SIF varied very little as a function of position along the crack front for a given geometry. When data were compared to results from Helot's boundary integral equation, good agreement (±2%) was achieved. Atluri's [1] FEM results also have decent agreement (within 10%) with this difference, which can be attributed to the 2.5 times fewer degrees of freedom used.

Kirkhope, Bell, and Kirkhope [13] used the FEM program ASAS to determine SIF in long radial cracks along the internal bore of the cylinder subjected to internal pressure. The SIFs in the vicinity of the crack tip were evaluated by substituting the nodal displacements into the Westergaard equations for open-ended cylinders (plane stress), with $W = R_o/R_i = 1.5$ to 2.25 and $a/t = 0.05$ to 0.5. Figure 2.2 shows the variation of normalized SIF versus a/t for different values of W. When the normalized SIF is plotted versus *(a/t)/(W-1)*, the data reduce to a smooth curve, and a least squares fit results in

$$\frac{K_I}{P\sqrt{t}} = 5.714(\alpha)^{0.5} - 4.258(\alpha) + 5.615(\alpha)^{1.5} \qquad 2.8$$

where $\alpha = (a/t)/(W-1)$. This expression is accurate to within ±1% of the FEM results obtained. When compared to the results of Bowie and Freese [2], values differ by less than ±2% for $a/t < 0.7$ and $W > 1.5$ and are greater otherwise.

2.1.3 Integral Methods [19, 9, 32, 37]

The boundary integral equation (BIE) and boundary element method (BEM) are integral methods as opposed to being differential methods like the FEM. As a result, BIE/BEMs are inherently more accurate than the FEM [19]. The advantages of these methods over the FEM are:

- Smaller systems of equations are generated, since only the boundary is discretized instead of the entire volume, resulting in more accurate interior stresses.
- Solutions are obtained at a limited number of points and can be concentrated to regions of interest such as a crack front.
- Two- and three-dimensional formulations are identical.
- Boundary conditions are satisfied automatically.

A procedure outlined by Tan and Fenner [32] consists of satisfying appropriate boundary conditions for displacements u_i and tractions t_i on the boundary of the body. Somigliana's integral equation is then used to relate surface displacements and tractions at a point Q to displacements at any interior point p with

$$u_i(p) = \int_S t_j(Q) U_{ij}(p,Q)\, dS - \int_S u_j(Q) T_{ij}(p,Q)\, dS \qquad 2.9$$

where U_{ij} and T_{ij} are displacements and tractions respectively at some surface point Q due to unit loading applied at point p with the subscript ij being the typical summation convention. If point p is taken to be a point on the boundary P not located at Q, the BIE becomes

$$\frac{1}{2}\delta_{ij} u_j(\mathrm{P}) + \int_S u_j(Q) T_{ij}(\mathrm{P},Q)\, dS = \int_S t_j(Q) U_{ij}(\mathrm{P},Q)\, dS \qquad 2.10$$

which is the BIE constraint relating boundary displacements to boundary tractions. Solving equation 2.10 yields the solution to tractions and displacements everywhere on

the boundary. When used with equation 2.9, displacements at any interior location can be determined. Thus, the stress state at any point can be determined by differentiating equation 2.9 with respect to the coordinates x_j at point p by

$$\sigma_{ij}(p) = \int_S t_k(Q) \frac{\partial U_{ki}(Q,p)}{\partial x_j}\bigg|_p dS - \int_S u_k(Q) \frac{\partial T_{ki}(Q,p)}{\partial x_j}\bigg|_p dS \qquad 2.11$$

These three equations are then solved numerically by discretizing the surface, resulting in a set of linear algebraic equations for the unknowns at nodal points. The SIF is then determined at the crack tip using the appropriate equations.

Tan and Fenner [32] used crack-opening displacement to determine the SIF at points along the semi-elliptical crack front. For their analysis, plane strain was assumed everywhere along the crack front except where it intersects the inner surface, at which point plane stress is assumed. Normalized SIFs were determined for R_o/R_i = 2.0 and 3.0, a/t = 0.2 to 0.8, a/c = 0.8, and a half cylinder length $L = 2.5t$ and are shown in Table 2-1. The material model assumed a Poisson's ratio ν of 0.3. Figure 2.3 shows the variation of the normalized SIF versus a/t at the center of the crack geometry, $\alpha = 0$, along with the geometry used. When compared to the Cruse-Meyers method, values differed by less than 1.5%.

GKD [9] used a hybrid BEM incorporating a dual BIE method, wherein two BIEs were used to determine the SIF around a semi-elliptical crack front. The first BIE is the same as equation 2.9. The second relates surface displacements and tractions at a point Q to tractions at any interior point p. Conformal mapping of the crack front from the circle plane is then employed to determine the SIF around the semi-elliptic crack front. GKD determined normalized SIFs for ratios of t/R_i = 0.5, 1.0, and 2.0; a/t = 0.2 to 0.8, a/c = 0.25 to 1.0; and c/L = 0.1. These values are shown in Table 2-2. The material model assumed a Poisson's ratio ν of 0.3. Figure 2.4 shows the variation of the normalized SIF versus a/t for different values of a/c, with t/R_i = 0.5, 1.0, and 2.0 along with the geometry used. From these plots, local maximums of the normalized SIF at the extreme values of a/t with a trough in-between are observed. Also, the magnitudes of the maximums increase for increasing t/R_i, with the trough being more pronounced as well. When

compared to recent publications using the body force method (BFM) and FEM, accuracies within 3% were obtained.

The BEM employing dual BIEs was again utilized by Yan and Dang [37]. In this case,for the plane strain state corresponding to a long crack in a circular cylinder running the length of the bore, the SIFs are considered by solving the identical problem of a cracked circular ring (plane stress). This is valid as long as the length of the cylinder is much greater than the other characteristic dimensions of the cylinder. The SIF was determined using the J-integral method for values of R_o/R_i = 1.25, 1.5, 1.75, 2.0, 2.25, and 2.5 and a/R_i = 0.0 to 1.4. When compared to boundary collocation techniques [2], errors of less than 5% were achieved except for cylinders with small R_o/R_i ratios containing cracks near boundaries (a/t approaching 0 or 1).

2.1.4 Boundary Collocation [19, 2]

Boundary collocation is a numerical technique used to obtain solutions to boundary value problems [19]. This method consists of applying an exact series solution to the governing equation, and truncating the series. This is accomplished by setting certain coefficients to zero based on geometry and symmetry conditions. The remaining constants are then solved from a set of linear equations that satisfy known boundary conditions. In most instances, the resulting series solutions exactly satisfy prescribed interior conditions while approximating boundary conditions.

Bowie and Freese [2] proposed a method for determining SIF for long cracks in cylinders (plane strain) by solving the identical problem of a cracked circular ring (plane stress). In this analysis, boundary collocation and Muskelishvili conformal mapping techniques were used for mapping stresses from the circle plane to the crack plane, where traction free conditions were imposed on the crack along with appropriate boundary conditions. The SIFs were computed for R_o/R_i = 1.25, 1.5, 1.75, 2.0, 2.25, and 2.5. Typical values of the normalized SIF versus $a/(R_o-R_i)$ are shown in Figure 2.5.When compared to BIE results [37] and FEM results [13], the accuracy is better than 5% except for large R_i/R_o with cracks near boundaries.

2.1.5 Summary of SIF Determination in Circular Cylinders

Various methods for determining SIF for internal surface cracks in circular cylinders with internal pressure have been presented for both part-through (semi-elliptic) and through cracks. Table 2-3 summarizes the geometry, method, and type of crack in order to compare the working range of each application.

It is apparent that GKD and Bowie & Freese have the greatest working geometry ranges for part-through and through cracks respectively. Also, each includes the geometry used in the experimental tests in their geometry ranges, allowing for direct comparison with experimental data.

2.2 SIF and the Internal Star Cylinder [7, 8, 34, 28, 29]

Limited SIF data are available for internal star cylinder configurations due to the complex geometry of the problem. Francis et al. [7, 8] performed 2-D experimental testing and FEM analysis to evaluate crack behavior for pressure loadings where pressure was applied directly to the crack surface. The test specimen geometry was that of an internal star cylinder cast from brittle epoxy with R_o = 7" and R_i = 1.59". Thin slices (0.250") were sawed from the cylinder, and small cracks were inserted at 30° from the star tip. Pressure was then applied over the cut faces of the model and at the inner bore. It was observed that upon propagation, the crack trajectory went straight to the outer boundary and was parallel to the fin axis.

Smith and his associates [34, 28, 29] have conducted tests using frozen-stress photoelasticity (discussed in chapter 3.3) to analyze semi-elliptic cracks located at critical locations around fin tips in internal star circular cylinders. In their analysis, cracks were grown under internal pressure, and the SIFs around the crack front for both symmetric and off-axis cracks were determined. Two specimen geometries were used. The first has R_o/t = 2 and 4, R_o = 50.6mm, and L = 304.8mm. The second has R_o/t = 2, R_o = 75.8mm, and L = 376mm. Schematics of these two geometries are shown in Figure 2.6.

For the first geometry, symmetric cracks originating from the fin axis under mode I loading were studied using the above-mentioned optical method. For these tests, all cracks were grown to similar depths with *a/c* = 0.44 to 0.50 and *a/t* = 0.62 to 0.74. The data show very little variation, ±3, in normalized SIF versus θ for any given crack. This tends to agree with the data obtained by Newman and Raju [23] for their 3-D finite element solution.

For the second geometry, off-axis cracks were studied using the same above-mentioned optical method. The cracks were started in two ways: normal to the fin surface or parallel to the fin axis. These experiments showed that the off-axis cracks start out with mixed mode loading (mode I & II), but during growth turn to eliminate the shear mode, becoming a mode I crack whose growth is parallel to the axis of the fin. The off-axis cracks were grown to varying depths with a/c = 0.59 to 0.78 and a/t = 0.21 to 0.34. Normalized SIFs were computed assuming the cracks were semi-elliptic and planar. This is more accurate for the off-axis cracks parallel to the fin surface, because minimal turning was required to eliminate the shear modes present. Values of normalized SIF versus a/t for off-axis cracks parallel to the fin surface are shown in Figure 2.7. As shown, the data scatter is within the 6% experimental accuracy.

3 Mathematical Formulation

3.1 The Stress Optic Law [4, 14]

To interpret fringe patterns, a relationship between applied stresses and the optical effect observed must be obtained. Photoelasticity is the study of just such a relationship.

At any point in the stressed material, three mutually perpendicular principal stresses (σ_1, σ_2, and σ_3) can be obtained. Also, if the material is photoelastic in nature, it is referred to as optically anisotropic, and three principal indices of refraction (n_1, n_2, and n_3) can be defined.

In a photoelastic material, the theory relating the indices of refraction to the state of stress in the material is the stress optic law. The stress optic law discovered by Maxwell [14], states that the changes in the indices of refraction are linearly proportional to the applied loads such that

$$\begin{aligned} n_1 - n_0 &= c_1\sigma_1 + c_2(\sigma_2 + \sigma_3) \\ n_2 - n_0 &= c_1\sigma_2 + c_2(\sigma_3 + \sigma_1) \\ n_3 - n_0 &= c_1\sigma_3 + c_2(\sigma_1 + \sigma_2) \end{aligned} \qquad 3.1$$

where n_0 is the index of refraction of the unstressed material, n_1, n_2, and n_3 are the principal indices of refraction in the stressed state associated with the principal directions, and c_1 and c_2 are the stress optic coefficients. It can be seen from equation 3.1, that if the three indices of refraction and their directions can be determined, the complete state of stress at that point can be determined.

Since experimentally determining the principal indices of refraction and their direction is difficult in the 3-D case, plane stress is used to simplify practical applications. For the plane stress case, equation 3.1 reduces to

$$n_1 - n_0 = c_1\sigma_1 + c_2\sigma_2$$
$$n_2 - n_0 = c_1\sigma_2 + c_2\sigma_1 \qquad 3.2$$

It is now convenient to eliminate n_0 from equation 3.2 and represent the stresses in terms of the relative index of refraction ($c = c_2 - c_1$) as opposed to the absolute change of index of refraction. Therefore,

$$n_2 - n_1 = (c_2 - c_1)(\sigma_1 - \sigma_2) = c(\sigma_1 - \sigma_2) \qquad 3.3$$

with c being a positive constant.

A photoelastic material sliced for data collection can be thought of as a wave plate (discussed in section 0); therefore, the relative indices of refraction can be related to the phase shift Δ by

$$\Delta = \frac{2\pi h}{\lambda}(n_2 - n_1) \qquad 3.4$$

where h is the thickness of the photoelastic slice, and λ is the wavelength of light transmitted through it. This equation is only valid if the slice is oriented such that two of the principal stresses are parallel to the plane formed by the slice face, and the third principal stress is aligned perpendicular to the direction of propagation of a beam of plane polarized light. Substituting equation 3.3 into 3.4, the phase shift through the specimen slice becomes

$$\Delta_s = \frac{2\pi hc}{\lambda}(\sigma_1 - \sigma_2) \qquad 3.5$$

It is convenient to express this equation as

$$\sigma_1 - \sigma_2 = \frac{Nf_\sigma}{h} \quad (\mathrm{N/m^2}) \tag{3.6}$$

where N is the relative retardation in terms of a complete cycle of retardation,

$$N = \frac{\Delta_s}{2\pi} \tag{3.7}$$

and f_σ is the material fringe value, which is a property of the material for a given wavelength of light, such as

$$f_\sigma = \frac{\lambda}{c} \tag{3.8}$$

For a given material fringe value f_σ and relative retardation N, the difference between the principal stresses $(\sigma_1 - \sigma_2)$ can be determined. In practice, N (the measured fringe order) is determined with a polariscope, and f_σ is determined by some calibration means, both of which will be discussed later.

3.2 The Polariscope [4, 21, 15, 16]

Two main types of polariscope exist -- linear and circular. A linear polariscope shows both isoclinic fringe patterns (fringes along the principal stress directions) and isochromatic fringe patterns (fringes of constant principal stress difference $\sigma_1 - \sigma_2$). The circular polariscope used in the ESM Photoelasticity and Fracture (P&F) Lab preserves isochromatic fringes while extinguishing isoclinic fringes. In this section the components of the circular polariscope will be discussed briefly along with their mathematical consequences.

The circular polariscope consists of two linear polarizers and two quarter-wave plates in series with a light source shown in Figure 3.1. The optical element closest to the light source is called the polarizer. Next are the first and second quarter-wave plates and

then the analyzer. Specimen slices are loaded between the two quarter wave plates when being analyzed.

Mathematically, the light source can be represented as a sinusoidal wave of amplitude A. The function of the polarizer (and analyzer) is to resolve the light vector into two mutually perpendicular components. The component of light vibrating parallel to the axis of polarization is transmitted (A_t) while the component perpendicular is blocked, A_b, (Figure 3.2a). For example, a light wave emerging from a polariscope oriented with its axis of polarization in the y-direction is expressed as

$$A_t = ke^{i\omega t} \tag{3.9}$$

where k is a constant, ω the circular frequency, and t the time.

A quarter-wave plate is a transparent optical element that resolves the incident light vector into two perpendicular components, each transmitted through the wave plate with different velocities. One component is transmitted along the fast axis with velocity c_1 and the other along the slow axis with velocity c_2 where $c_1 > c_2$. The fast and slow axes have indices of refraction n_1 and n_2 respectively. The difference in index of refraction and therefore transmission velocity is due to the optical anisotropy associated with the wave plate. The result is a relative angular retardation (Δ) developed between the emerging light vectors. The angle formed by the fast axis of the wave plate and the axis of the polarizer is β. Circularly polarized light is produced by selecting a wave plate with $\delta = \lambda/4$ ($\Delta = \pi/2$) and $\beta = \pi/4$, hence the name quarter-wave plate (Figure 3.2b). The light components emerging from the first quarter wave plate are

$$\begin{aligned} A_{t1} &= \frac{\sqrt{2}}{2} ke^{i\omega t} \\ A_{t2} &= -i\frac{\sqrt{2}}{2} ke^{i\omega t} \end{aligned} \tag{3.10}$$

The light components then strike the specimen slice. The slice acts as a wave plate and decomposes the light vectors into components along the principal stress directions (Figure 3.3). Upon emergence from the specimen, a relative retardation (Δ_s) is developed between the light vectors. Recall

$$\Delta_s = \frac{2\pi hc}{\lambda}(\sigma_1 - \sigma_2) \qquad 3.11$$

The light then continues to the second quarter-wave plate. It is oriented such that its fast and slow axes line up with the slow and fast axes of the first quarter-wave plate respectively. The light then enters the analyzer, whose axis of polarization is parallel to the x-axis. As a result all light perpendicular to the x-axis is extinguished, and the final amplitude is

$$A_{ax} = \frac{k}{2} e^{i(\omega t + 2\alpha)}\left(e^{-i\Delta_s} - 1\right) \qquad 3.12$$

This particular arrangement of optical elements, used in the ESM P&F Lab, produces a dark field. In all, four possible arrangements exist -- two produce dark and two produce light fields (Table 3-1).

The intensity of the emerging light is proportional to the square of the amplitude. In exponential form, this is equal to the amplitude and its conjugate and is given by

$$I = K \sin^2\left(\frac{\Delta_s}{2}\right) \qquad 3.12$$

This implies that the light emerging from a circular polariscope is a function only of the principal stress difference ($\sigma_1 - \sigma_2$). Also, since the intensity is not a function of α, the isoclines have been eliminated from the fringe pattern as stated earlier.

For a dark field with intensity equal to zero,

$$\frac{\Delta_s}{2} = n\pi \qquad 3.13$$

This leads to fringe orders

$$N = \frac{\Delta_s}{2\pi} = n \qquad for \quad (n = 0,1,2,3\ldots) \qquad 3.14$$

Similarly, it can be shown that the fringe order for a light field is

$$N = \frac{1}{2} + n \qquad for \quad (n = 0,1,2,3\ldots) \tag{3.15}$$

Twice as many data points can be obtained if both dark and light fields are used. Since, in practice, slice thicknesses are small, the number of fringes present in data collection is small. Therefore, other methods for obtaining extra data points need to be employed.

3.2.1 Tardy Compensation [4, 33]

Tardy compensation [33] is a technique that extends the fringe analysis to fractions of a fringe order. This is done by rotating the analyzer through an arbitrary angle γ, a schematic of which is shown in Figure 3.4. As a result, the equation of the emerging light vector and the corresponding intensity must be modified to

$$\begin{aligned} A_{a\gamma} = \frac{\sqrt{2}}{2} k e^{i\left(\omega t + \alpha - \frac{\pi}{4}\right)} \{ & \sin\left(\tfrac{\pi}{4} - \alpha\right)\left[e^{-i\Delta_s} \cos\left(\tfrac{\pi}{4} + \gamma\right) - \sin\left(\tfrac{\pi}{4} + \gamma\right)\right] \\ & + i \cos\left(\tfrac{\pi}{4} - \alpha\right)\left[e^{-i\Delta_s} \sin\left(\tfrac{\pi}{4} + \gamma\right) - \cos\left(\tfrac{\pi}{4} + \gamma\right)\right]\} \end{aligned} \tag{3.16}$$

$$I = K\left[1 - \cos(2\gamma)\cos(\Delta) - \cos(2\alpha)\sin(2\gamma)\sin(\Delta)\right]$$

To determine the fringe order, the maximum and minimum intensities must be obtained for any γ. This is done by taking the derivative of the intensity with respect to Δ and α independently, setting them to zero, and solving both equations simultaneously. For the minimum intensity ($I = 0$) it can be shown that

$$\alpha = \frac{n\pi}{2} \tag{3.17}$$

This leads to

$$\Delta = 2\gamma \pm 2n\pi \qquad for \quad (n = 0,1,2,3\ldots) \tag{3.18}$$

This condition requires one of the principal stress axes to coincide with the axis of polarization of the polarizer ($\alpha = 0, \frac{\pi}{2}, \pi, \ldots$). This results in fringe orders of

$$N = \frac{\Delta}{2\pi} = n \pm \frac{\gamma}{2} \qquad for \quad (n = 0,1,2,3\ldots) \tag{3.19}$$

To align the axis of the polarizer with one of the principal stress axes, the fast axis of the two quarter wave plates need to be parallel. This converts the circular polariscope into a plane polariscope, exposing the isoclines so the direction of the principal stresses can be determined. The polarizer, quarter wave plates, and analyzer are then rotated in unison until the axis of the polarizer is parallel to one of the principal stress directions. The quarter wave plates are then crossed again, producing a dark field. Rotating the polarizer will now produce fractional fringe orders, increasing the number of data points. At times, even more data points are necessary and can be achieved by using Post fringe multiplication in parallel to the Tardy method.

3.2.2 Post Fringe Multiplication [4, 20, 22]

Post fringe multiplication [20, 22] is a full field method used to multiply the number of fringes observed in a specimen. This is achieved using two partial mirrors in series, one on either side of the specimen slice (Figure 3.5). The function of a partial mirror is to transmit part of the light beam while reflecting the rest.

Inclining one of the mirrors slightly with respect to the other results in back and forth reflection of light between the mirrors and through the slice. The ray number indicates the number of times the slice has been traversed and is also the amount of fringe multiplication achieved for that ray. Since each ray exits at a different angle with respect to the polariscope, the ray of interest can easily be isolated by blocking the others. For example, consider a multiplication factor of 5 in a dark field. This produces a fringe order sequence of $0, \frac{1}{5}, \frac{2}{5}, \frac{3}{5}\ldots$ For this example, the available data increase by a factor of 5.

3.3 3-D Photoelasticity [4]

In general, the stress freezing process is a three-dimensional photoelastic method. However, planes of symmetry or principal planes can be utilized to reduce the problem to a plane problem. For a cylindrical pressure vessel, slices extracted in the hoop direction (Figure 3.6) results in one of the principal stresses being out of the plane and can be analyzed using two dimensional photoelastic techniques. When loaded in a polariscope, this out of plane stress is aligned with the light beam. As a result, the mathematics governing a circular polariscope, section 0, are valid.

Recall that isochromatics are fringes of constant principal stress difference. To accurately determine this stress difference, the fringe order must be established at every point in the model. This is accomplished by locating the zero order fringe. A zero order fringe exists at a free corner, because the shear stress there is zero. Once the zero order fringe is located, fringe orders at any other point in the specimen can be determined by counting outward from that fringe (Figure 3.7). The stress difference can now be determined at any point as

$$\sigma_{rr} - \sigma_{\theta\theta} = \frac{Nf_\sigma}{h} \tag{3.20}$$

To determine the material fringe constant f_σ, a body with a known stress distribution, such as a four-point bend specimen, must be analyzed (Figure 3.8). The four-point bend specimen has a constant bending moment in the center of the beam that can easily be determined from equilibrium as

$$M = Pb + \frac{W}{2}\left(\frac{L}{4} - a\right) \tag{3.21}$$

The stress is therefore

$$\sigma_{yy} = \frac{Mx}{I} = \frac{nf_\sigma}{t} \qquad with \qquad I = \frac{th^3}{12} \tag{3.22}$$

As a result, the material fringe constant is

$$f_\sigma = \left(\frac{12}{h^3}\frac{x}{N}\right)\left[Pb + \frac{W}{2}\left(\frac{L}{4} - a\right)\right] \qquad 3.23$$

Substituting this into equation 3.20 will produce the stress difference in the specimen slice.

3.4 Fracture Mechanics in Photoelasticity [4, 11, 35, 27, 12, 17]

When evaluating the stress at the tip of a crack, it is necessary to use fracture mechanics due to the stress singularities present. Singularities exist, because a crack is sharp with a tip radius of curvature approaching zero. Stress singularities at a crack tip can be evaluated by introducing the stress intensity factor (SIF) *K*. Three types of stress intensity are defined by the types of loading encountered: modes I, II, and III.

Mode I crack growth, referred to as the opening mode, is due to loading that is perpendicular to the crack surface displacement (Figure 3.9a). The SIF associated with mode I loading is K_I. Mode II crack growth is caused by in-plane shear loading (Figure 3.9b). This type of loading causes the crack surfaces to slide across one another. The SIF associated with mode II loading is K_{II}. Mode III is a tearing mode, which is due to out of plane shear loading (Figure 3.9c). It has a corresponding SIF of K_{III}.

In general, a crack may exhibit all three modes of cracking. Mixed modes (modes I and II) or mode I alone, however, are the most common. In fact, any crack, if given sufficient time, will orient itself so only mode I is present; this is the dominant mode of facture.

For mode I loading of an isotropic linear elastic material, the stress field can be defined as [11]

$$\lim_{r \to o} \sigma_{ij} = \frac{K_I}{\sqrt{2\pi r}} f_{ij}(\theta) \qquad 3.24$$

where f_{ij} is a dimensionless function of theta. The function $f_{ij}(\theta)$ is determined from field equations that satisfy the boundary conditions exactly. The form of this function varies depending on position relative to the crack tip (Figure 3.10).

The area surrounding the crack tip can be divided into three regions: the very near field, the near field, and the far field. To evaluate the SIF in these regions, field equations that are independently valid within each region are used. Westergaard [35] introduced a complex stress function Z(z) that satisfies the Airy stress function in the very near field with

$$Z = \frac{K_I}{\sqrt{2\pi}} z^{-\frac{1}{2}} = \frac{K_I}{\sqrt{2\pi}} r^{-\frac{1}{2}} e^{-i\frac{\theta}{2}} \tag{3.25}$$

As a result, the stresses become

$$\begin{aligned}
\sigma_{rr} &= \mathrm{Re}\, Z - y\, \mathrm{Im}\, Z' - \sigma_0 = \frac{K_I}{\sqrt{2\pi r}} \cos\left(\frac{\theta}{2}\right)\left[1 - \sin\left(\frac{\theta}{2}\right)\sin\left(\frac{3\theta}{2}\right)\right] - \sigma_0 \\
\sigma_{\theta\theta} &= \mathrm{Re}\, Z + y\, \mathrm{Im}\, Z' = \frac{K_I}{\sqrt{2\pi r}} \cos\left(\frac{\theta}{2}\right)\left[1 + \sin\left(\frac{\theta}{2}\right)\sin\left(\frac{3\theta}{2}\right)\right] \\
\tau_{r\theta} &= -y\, \mathrm{Re}\, Z' = \frac{K_I}{\sqrt{2\pi r}} \cos\left(\frac{\theta}{2}\right)\sin\left(\frac{\theta}{2}\right)\cos\left(\frac{3\theta}{2}\right)
\end{aligned} \tag{3.26}$$

where σ_0 is a non-singular stress introduced by Irwin [11] to make theoretical fringe patterns match experimental fringe patterns.

For data restricted to $\theta = 90°$, Smith [27]) introduced an algorithm for experimentally determining the stress intensity factor. For $\theta = 90°$ the stresses become

$$\begin{aligned}
\sigma_{rr} &= \frac{K_I}{4\sqrt{\pi r}} - \sigma_0 \\
\sigma_{\theta\theta} &= \frac{3K_I}{4\sqrt{\pi r}} \\
\tau_{r\theta} &= -\frac{K_I}{4\sqrt{\pi r}}
\end{aligned} \tag{3.27}$$

This simplification can be made, because for mode I crack growth, the isochromatic fringe loops are oriented approximately normal to the crack tip (Figure 3.11). This makes the data easier to obtain, since readings are more accurate in this direction.

The maximum shear stress can now be solved from the previous equations by

$$\left(2\tau_{\max}\right)^2 = \frac{K_I^2}{2\pi r} + \frac{K_I\sigma_0}{\sqrt{\pi r}} + \sigma_0^2 \qquad 3.28$$

thus yielding K_I

$$K_I = \sqrt{\pi r}\left[\sqrt{8\tau_{\max}^2 - \sigma_0^2} - \sigma_0\right] \qquad 3.29$$

Noting that near the crack tip, the non-singular term σ_0^2 is small compared to $8\tau_{max}^2$, the SIF becomes

$$K_I = \sqrt{8\pi r}\tau_{\max} - \sqrt{\pi r}\sigma_0 \qquad 3.30$$

This equation can be simplified by introducing the apparent SIF

$$\left(K_I\right)_{AP} = \sqrt{8\pi r}\tau_{\max} \qquad 3.31$$

Recall from section 3.3 that the maximum shear stress can also be described in terms of photoelastic parameters as

$$\tau_{\max} = \frac{\sigma_1 - \sigma_2}{2} = \frac{Nf_\theta}{2t} = \frac{Nf_\tau}{t} \qquad 3.32$$

where

$$f_\tau = \frac{f_\sigma}{2} \qquad 3.33$$

By combining the equations 3.31 and 3.32, the apparent SIF can be obtained at different locations by measuring r and N.

When $(K_I)_{AP}$ verses $(r/a)^{1/2}$ is plotted, three distinct regions appear. The first region, located right at and adjacent to the crack tip, has a variation of $(K_I)_{AP}$ verses $(r/a)^{1/2}$ that is nonlinear. This nonlinearity is due to plasticity occurring locally at the crack tip. The plasticity is a result of the stress singularities exceeding the materials yield strength. In the second region, $(K_I)_{AP}$ verses $(r/a)^{1/2}$ is linear, and the above equations apply in the context of linear elastic fracture mechanics. When $(K_I)_{AP}$ verses $(r/a)^{1/2}$ is extrapolated back to the y-axis, the intercept corresponds to the K_I value at the crack tip [27]. $(K_I)_{AP}$ verses $(r/a)^{1/2}$ is again nonlinear in the third zone, because the nonsingular term σ_0 is no longer negligible. Therefore, $(K_I)_{AP}$ varies in a nonlinear fashion.

If multiple tests are conducted, the crack geometry and load must be normalized out of the SIF, so meaningful comparisons can be made. The normalized stress intensity factor is

$$F_{nor} = \frac{K_I}{p\sqrt{\pi a}}\sqrt{Q} \tag{3.34}$$

Where p is the stress freezing pressure and Q is a crack shape factor defined as

$$Q = 1 + 1.464\left(\frac{a}{c}\right)^{1.65} \tag{3.35}$$

with a and c being the minor and major axes of the semi-elliptical crack respectively (Figure 3.12). The shape factor Q, first observed by Irwin [12], is the square of an elliptic integral of the second kind, which is due to the fact that surface flaws are generally assumed to be elliptic in shape. Values for Q are often taken directly from tables, but Q from equation 3.35 is an approximation developed by Newman [17] that is commonly used for cracks in pressure vessels whose ratios of a/c are greater than 0.4.

4 Experimental Procedures

4.1 Introduction

The tested specimens fall into two categories -- those with natural cracks and those with V-cut cracks. The natural crack specimens are made by making a small crack in the cylinder. The crack is then grown under pressure to depths that are approximately 9, 18, and 24mm. Specimens containing V-cut cracks are produced by cutting a crack the length of the specimen with depths matching those of the three natural cracks. The V-cut crack specimens represent, as close as is possible in the lab, the plane strain approximation of the natural crack specimens.

In this chapter the experimental procedures for both sets of tests will be discussed in detail. This will include material mechanical information, specimen geometry and test preparation, the stress freezing process, slice extraction, and data extraction using a laser polariscope employing Tardy and Post methods in tandem.

4.2 Material Specifications

4.2.1 PLM-4BR

Three materials are used for casting and bonding the specimens. The first (PLM-4BR), provided by Photoelastic Inc., is used when casting the internal star cylinder and the calibration beam. PLM-4BR is a two-part epoxy resin and, when in liquid form, is composed of a resin and hardener. The resin and hardener are mixed with a mass ratio of 100:7 respectively. This mixture is cured at around 120^{o} F (49^{o} C) for 48 hours. After curing, PLM-4BR is a solid, transparent, photoelastic material. A photoelastic material is

one that when unstressed is optically isotropic. However, when the material is stressed, it becomes optically anisotropic and remains this way until the stresses are removed. This phenomenon is known as temporary double refraction.

PLM-4BR, in addition to being a photoelastic material, is also a diphase material, which means that at elevated temperatures it exhibits different mechanical and optical properties than at room temperature. The temperature at which this transition occurs is known as the critical temperature. For PLM-4BR, this temperature is around 200^{o} F At room temperature the material is a hard solid that behaves in a viscoelastic manner that can be explained by a simple Kelvin model of a spring and dashpot in parallel (Figure 4.1). Above the critical temperature, it is a soft, rubbery solid that is orders of magnitude less resistant to deformation. However, its mechanical response is purely elastic in nature. This reduction of resistance to deformation is due to the fact that the modulus of elasticity is about 0.2% of what it is at room temperature. Thus, the material is about 20 times more fringe sensitive than it is at room temperature. If the material is cooled slowly from above the critical temperature back to room temperature with the load maintained, the large deformations are locked into place even after the load is removed with negligible elastic recovery. This procedure is known as stress freezing and is described in detail by Oppel [18]. Mechanical data for PLM-4BR at room temperature and at critical temperature are shown in Table 4-1. Above the critical temperature, the Poisson's ratio increases to 0.5, and as a result it behaves as an incompressible material.

4.2.2 PMC-1

The second material used for casting and bonding is PMC-1, again provided by Photoelastic Inc. PMC-1 is a two part epoxy used for joining model sections. Before mixing, PMC-1 resin is preheated to 90° F (32°C). It is then mixed with a resin to hardener mass ratio of 100:14 and cured at room temperature for 24 hours. When cured, it is transparent and has a coefficient of thermal expansion similar to PLM-4BR, minimizing stresses caused by thermal expansion.

4.2.3 RTV

RTV 630 is used for making the cast end caps and when bonding RTV to PLM-4BR (provided by Photoelastic Inc.). RTV 630 is a two part epoxy consisting of parts RTV 630-A (the resin) and RTV 630-B (the hardener). Parts A and B are mixed with a mass ratio of 10 to 1 respectively and cured at room temperature for 24 hours. When cured, it is a blue, opaque, flexible solid.

4.3 Specimen Geometry and Preparation

4.3.1 The Internal Star Cylinder

As stated previously, two categories of test specimen exist -- the natural crack and the machined V-cut crack. The specimen geometries for both test categories are identical. However, preparation for the natural crack differs greatly from that of the V-cut. Both categories will be discussed.

The specimen geometry is that of a six-point internal star cylinder configuration shown in Figure 4.2. The internal star cylinders are 376.0mm long*, 151.56mm in diameter, and 37.08mm from fin tip to cylinder edge. The length of 376mm is sufficient to ensure that end effects do not influence the data in the region of interest (the center of the specimen).

4.3.1.1 Natural Crack

The first step in the preparation process for the natural crack specimens is to initiate the crack. This is accomplished by drilling a hole directly across from one of the fin tips at the halfway point of the tube. To ensure the crack is perpendicular to the surface of the fin tip, the hole must be drilled as close to straight as possible. The crack is

* Specimen 3 was 335.75mm long.

then started by striking a sharp heavy duty blade with a hammer (Figure 4.3). By centering the blade on the fin tip so the blade is parallel to the fin surface, a longitudinal crack normal to the fin surface is produced. The crack growth can be described by two phases. The first is dynamic growth, which is where rapid crack growth occurs. The second phase occurs when the crack reaches a critical depth. At this point, crack propagation slows rapidly, and the crack comes to rest. The shape of a natural crack is that of a semi-ellipse with major and minor axes of length *2c* and *a* respectively (Figure 4.4).

The hole is then filled with a 6.56mm diameter PLM-4BR plug (made by the ESM machine shop), which is bonded in place with PMC-1. The purpose of the plug is to minimize the stress concentration at the hole. This stress concentration, however, does not have any effect on the stress at the crack tip, since it is located on the opposite side of the specimen. In fact the effect of the hole is not observed past the adjacent fins.

4.3.1.2 V-Cut Crack

To make the V-cut crack, a fixture to hold the test specimen during machining was required. The fixture provided a stationary platform that ensured the crack would be machined centered on and perpendicular to the fin's surface (Figure 4.5a). Before the crack is machined, the model was first sawed in half lengthwise down the tube. This provided room enough for the 203.20mm diameter, 2.5mm thick, 30° beveled circular saw blade to machine a crack to a maximum depth of 24mm (Figure 4.5b). The cracks are machined the length of the tube minus a small length on either end. These are left uncut to provide strength when the specimen is under pressure to ensure the crack does not grow and penetrate at the specimen ends.

The two halves of the specimen are then glued back together using PMC-1 resin. Much care must be taken during this process to ensure that a proper seal is achieved. For the end caps to fit properly, 1.25mm thick shims are spaced between the halves. These ensure that the thickness lost during sawing is recovered in the bonded specimen. This is difficult in practice because the PMC-1 epoxy is fluid when first mixed. PMC-1 must partially cure (1.5 hours for a 10 gram container) before application, so it will not flow

out from between the two halves. This is further complicated by the fact that the end caps must be bonded at the same time while the PMC-1 is still liquid. Curing the PMC-1 before inserting the caps would create issues with fit.

4.3.2 End Caps

Each specimen requires two RTV 630 end caps, which are cast negatives of the internal star cylinder. The caps have a 63.5mm tall finned section attached to a 22.2mm tall by 151.56mm diameter base. Preparation for specimen end cap sets is similar for the natural and V-cut cracks. The only difference is that the finned sections for V-cut specimens are cut down to 19.05mm, making their insertion easier and effectively increasing the region not affected by the end. For each set of caps, a 6.35mm hole is drilled down the center of one cap for air supply access.

To bond the caps to the specimen, the specimen surfaces are lightly abraded with 280 grit sand paper to provide a better bonding surface and cleaned with acetone and alcohol. The specimen surfaces are then primed with SS4120 silicone primer and left to dry completely. The fin surfaces of the end caps are coated with silicone release agent for smooth entry, and the horizontal surface of the base is coated with 20 grams of RTV 630 epoxy. The end caps are then inserted into the specimen by applying a light uniform pressure across the surface of the cap. A 20 pound weight is placed on top of the specimen during the curing process to ensure the caps remain in contact with the specimen and bond completely. Last, a 6.35mm copper tube is inserted into the drilled end cap and bonded in place with RTV 630 epoxy. A schematic showing the fit between the cylinder, end caps, and copper tube is shown in Figure 4.6.

4.3.3 Calibration Beam

The calibration beam is used in a four-point bend test to determine the material fringe constant f_σ and the critical temperature. Three calibration beams cast by Photoelastic Inc. to dimensions of 152.4mm long, 25.4mm tall, and varying thickness are provided with each internal star specimen and made from the same epoxy batch. Thus,

any discrepancies between batches (cure temperature, age, moisture…) are essentially normalized out. The thickness variation of the beam depends on the amount of material used in the casting process and the amount of material that must be shaved off to achieve a uniform thickness. Thicknesses are on average 10.42mm.

One of the beams is drilled through the thickness with four 6.35mm diameter holes located at 12.7 and 25.4 inches from either end of the beam. A schematic is shown in Figure 4.7. These holes provide points at which to apply the loads for the bend test. The beam's length is sufficient to achieve a pure bending moment in the midsection. As a result, the fringes at the center of the beam will be close to parallel and nearly equally spaced.

4.4 Stress Freezing

The stress freezing method developed by Oppel [18] is the method of locking in model deformations and the associated optical response in a photoelastic material. The calibration beams under four-point bending and pressurized specimens were all subject to a stress freezing cycle in a Blue M POWER-O-MATIC 70 Photoelasticity, Drying, and Annealing temperature controlled oven.

The calibration beam is hung in the temperature controlled oven under four-point bending with an appropriate load applied. The load is chosen such that when the beam is above the critical temperature, enough fringes are present to accurately determine the material fringe constant f_σ. Testing has shown that five pounds is sufficient to produce around 10 fringes above and below the neutral axis of the beam. The specimen is then placed in the oven with the copper tubing attached to a compressed air supply outside of the oven (Figure 4.8). The specimen is now ready to start the stress freezing process.

The stress freezing process consists of three stages. The stages are controlled with an aluminum cam that spirals inward as the oven heats and outward when cooled. The rate of temperature increase or decrease (the temperature ramp) was controlled manually for each stage by adjusting the cam rotation rate.

In the first stage, an initial pressure of about 10 kPa was applied to keep the crack open during the entire process. The oven temperature was increased from room temperature to just above the critical temperature of approximately 220° F at a rate of 7 to 8° F (13.3 to 13.9° C) per hour. The critical temperature was monitored by watching the fringes in the calibration beam. As the calibration beam passed the critical temperature, the number of fringes increased dramatically. Heating was then stopped, and the specimen was soaked at this temperature for three hours. This second stage ensured that the specimen achieved a uniform temperature throughout. During the soak, internal pressure was slowly applied to the specimen. The amount of applied pressure was monitored on the pressure gauge and controlled by opening the pressure regulator valve. For the V-cut crack, no crack growth was required, so a constant pressure (the stress freezing pressure, P_{sf}) large enough to ensure the presence of fringe patterns was applied. The stress freezing pressure was between 20 and 50 kPa.

For the three natural crack specimens, elevated pressures were used to grow the cracks to approximately 9, 18, and 24mm respectively. This was done by slowly increasing the pressure until crack propagation occurred (between 122 and 170 kPa). The pressure was then maintained, and the crack was grown to the desired maximum depth. When the maximum depth was reached, the pressure was reduced by approximately one-third to the stress freezing pressure, which ranged from 20 to 50 kPa. If the stress freezing pressure was too high, further crack growth could occur, and no data could be collected for cracks that grew and penetrated the outer wall (Figure 4.9). The stress freezing pressure was maintained throughout the remainder of the process, leaving stresses in the model elevated for subsequent data collection.

The third stage in the stress freezing process is cooling. In this stage, the oven was cooled at around 0.7 to 0.8° F per hour until it reached 140° F. The specimen was well below its stress freezing temperature at this point. As a result, the deformations and corresponding optical effects occurring at elevated temperatures were locked in. The cooling rate was then increased to 2° F per hour until the oven reached room temperature. The specimens were then removed from the oven and sliced for analysis. A plot of the temperature vs. time and pressure vs. time for the stress freezing process is shown in Figure 4.10.

4.5 Slice Extraction and Data Collection

To extract individual slices, a cube containing the entire crack was first machined from the model. Individual slices were then removed using a diamond wafer saw tangential to the crack front. This ensured that one of the principal stresses was out of the plane of the slice. As a result, 2-D photoelasticity can be utilized, since the effect of the out of plane stress is embedded in the in-plane stresses. Mathematically this is equivalent to the plane problem formulated in section 3.4.

Since the crack front is a straight line in the section of interest, the removed sections for each V-cut specimen are parallel with respect to each other (Figure 4.11a). The crack front for the natural crack is semi-elliptical in shape; therefore, each slice is rotated relative to the center line of the crack front (Figure 4.11b). The thickness of the natural crack slices must remain small relative to the model dimensions (less than 1mm) to ensure that stresses are essentially constant in magnitude and direction throughout the slice thickness.

Once removed, they are kept in a sealed container filled with index matching fluid. This keeps the slices from absorbing moisture, which would alter their stress state. Stress intensity data were collected by mounting the specimen slices in the multiplication unit of the refined laser polariscope (Figure 4.12) designed by Epstein [5, 6]. Post and Tardy compensation techniques were then used in parallel to extract data points along an isoclinic, rotated so its alignment was perpendicular to the crack axis. On average multiplication factors of 3 with Tardy rotations of 18° were sufficient to produce enough data points. This combination produces reading increments of one-thirteenth of a fringe order. It should be noted that the material fringe constant f_σ, used in the determining the SIF must be increased by 10% to account for difference in wavelength between the diffuse light polariscope (used to determine the fringe constant) and the laser polariscope (used to collect fringe data in the specimen slices).

5 Results and Conclusions

5.1 Introduction

Data have been collected for six specimens, three natural crack models grown to depths of a = 8.13, 14.6, and 19.6 mm and V-cut crack models cut to the same depth. Data were then analyzed using methods described in chapter 4 by applying the mathematical algorithms of chapter 3. Results of the SIF will be presented for each case and compared with:

1) Guozhong, Kangda, and Dongdi (GKD) [9] modified boundary element method solution to a circular cylinder containing a semi-elliptic crack.
2) Bowie and Freese's [2] boundary collocation solution to a circular cylinder containing a crack extending the length of the bore (plane strain solution).
3) Experimental results from Smith, Constantinescu, and Liu [29] for off-axis cracks started parallel to the fin surface.

These comparisons will yield a potential relation for estimating the plane strain SIF for the finned cylinder models for use in motor grain design. This will be accomplished by comparing the SIF of the semi-elliptic and V-cut cracks of the finned cylinder experiments measured at the deepest point of penetration to corresponding cracks in the numerical work mentioned above.

5.2 Test Conditions and General Comments

Six tests have been conducted, three natural crack models and three V-cut crack models, to study the behavior of propagated cracks of varying depths and geometries at the geometric center of the crack border. For ease of comparison, the test conditions, crack geometries, and material characteristic constants are shown in Table 5-1.

Natural cracks originating from the axis of symmetry of the fin were planar, grew in that plane, and experienced mode I stress fields everywhere around their flaw border. They grew readily under internal pressure with no unusual effects, maintaining their semi-elliptic shape. Hence, the elliptic integral of the second kind (defined in section 3.4) was adopted to normalize the crack geometry effect on the SIF distribution. A typical crack profile and cross section is shown in Figure 5.1. It is interesting to note that the ratio of crack depth to half crack length *a/c* varies by only a small amount, from 0.60 to 0.65. This fact is useful for judging crack depth during growth due to the fact that it is much easier to see and measure the crack length than the depth. The relatively constant *a/c* ratio also indicates that cracks grow in a uniform fashion, thus yielding the same shape at any point in their growth.

The V-cut specimens in general exhibited no crack growth, with the exception of model 6b, which grew and penetrated the outer edge. Stress intensity data were collected for this specimen, however, photoelastic data were difficult to read and unreliable due to low stresses resulting from the pressure drop caused by penetration. As such, no data for this model were considered. However, general conclusions can be made about the shape of the crack during failure. This will be discussed in later sections.

It should be noted that the same elliptic integral used to normalize geometric effects for the natural crack was used on the V-cut specimens. This was done strictly for comparison purposes. Using this approximation on a long crack is not entirely accurate, since the crack front is not semi-elliptic in shape and the *a/c* ratios for the long cracks are outside the range of intended use. The influence of using Q as a normalization factor has little effect in the SIF magnitude, because as $a/c \to 0, \quad Q \to 1$. However, this may in fact underestimate the effect of shape in the normalized SIF, and care must be taken when interpreting results.

For each crack, slices of constant thickness were removed normal to the crack border, the locations of which are shown in Figure 4.11. The variation in SIF along the crack border was obtained by averaging the data at corresponding locations on either side of the crack centerline. It should be pointed out that through thickness variations of stresses can occur in a slice, especially for slices extracted along a curved border. Photoelastic readings work to average these effects. The fact that the slices are cut thin for natural crack specimens and normal to the crack border also reduces the variation.

5.3 SIF Results

SIF values were determined by using the methods of chapter 4 and then applying the algorithms of chapter 3. In short this was done by photoelastically analyzing each slice to determine fringe orders at locations near the crack tip. It was then possible to obtain the maximum shear stress distribution used in the stress optic law to determine stress intensity data. Figure 5.2 shows a typical fringe pattern. Note the fringe loops are perpendicular to the crack tip, so only a mode I stress field is present.

$(K_I)_{AP}$ was then calculated and plotted versus $(r/a)^{1/2}$ in order to determine the linear zone. The SIF (K_I) is the intercept obtained by extrapolating this linear region to the y-axis, $r = 0$. To compare data between different tests, the crack geometry and loading were normalized by dividing by $p(\pi a/Q)^{1/2}$. A typical plot of normalized SIF (F_{AP}) versus $(r/a)^{1/2}$ is shown in Figure 5.3, where F_{AP} is the normalization of $(K_I)_{AP}$. Thus F is the intercept obtained by extrapolating the linear region of this plot to the y-axis. Numerical data for the normalized SIF (F), the SIF (K_I), and the zone of linearity $(r/a)^{1/2}$ are shown in Table 5-2 for both V-cut and natural crack specimens at different locations along the crack border. A typical linear data zone for a specimen slice is shown in Figure 5.4. It should be noted that for model 2, the SIF increases for the reading taken away from the center. Normally, off center SIF values are expected to be lower than those at the center. However, these data still fall within the ±6% experimental error.

The variation in normalized SIF versus a/t for the natural and V-cut models is shown in Figure 5.5 and Figure 5.6 respectively with data taken at the centerline of the

crack front. The normalized SIF for the natural crack models is largest in magnitude for the shallow crack, model 1, and decreases by 12.5% to a constant value for the deeper cracks, models 2 and 3. The V-cut crack models have the opposite trend (Figure 5.6), with the shallow crack, model 4, having the lowest normalized SIF and increasing by 11.7% to a constant value for the deeper cracks, models 5 and 6. When Figures 5.5 and 5.6 are shown on the same graph (Figure 5.7), the experimental results for the V-cut case are equal to or greater than that of the natural crack with the values for the two shallow crack models being essentially the same. This implies the existence of a substantial dominant boundary effect in this region.

The variation in normalized SIF along the crack border for the V-cut specimens is shown in Figure 5.8. SIF data were collected from the V-cut crack specimen at 0", 1", and 4" intervals on either side of the crack centerline to determine possible variation in SIF along the crack length. In general the SIF is not constant; it decreases by 12.5% for the extreme values of model 6. This implies that the ends do have an affect on the SIF away from the crack centerline. A linear regression generally shows only a slight decrease in normalized SIF, with values just outside the ±6% expected from experimental error.

5.4 Comparisons with Analytical and Experimental Work

Analytical solutions to SIFs in circular cylinders containing part-through and through cracks have been presented in chapter 2. The work of GKD [9] on semi-elliptic cracks in circular cylinders and the work of Bowie and Freese [2] on long cracks extending the length of the bore in circular cylinders provide the largest range of SIF data versus model and crack geometry for direct comparison. The geometry chosen for the numerical comparison was the same as the experimental work, with $t/R_i = 1.0$ ($R_i/R_o = 0.5$) where R_i is measured from the center of the cylinder to the fin tip for the finned cylinder and a/t and a/c corresponding to values from the experimental specimens. Table 5-3 lists the normalized SIF F and the SIF K_I for numerical and experimental data with the above geometry.

For semi-elliptic cracks, the normalized SIF versus *a/t* for the numerical data of GKD and these experimental data are shown in Figure 5.9. It can be seen that the data qualitatively have the same trends. The SIF starts out high and dips into a relatively constant region for *a/t* between 0.2 and 0.55. Smith and his associates [29] obtained results similar to these experiments from semi-elliptic off-axis cracks inserted parallel to the fin axis in finned cylinders of the same geometry. Figure 5.10 shows the normalized SIF for tests performed by Smith for *a/c* and *a/t* similar to these experiments. These off-axis cracks originate from the point of highest stress on the fin tip. Such cracks contain mixed mode loading (modes I and II), and as a result, require larger stresses to cause growth. Therefore, a crack initiated on the axis of symmetry of the fin represents a more critical crack case than an off-axis crack.

The normalized SIF versus *a/t* for the numerical data of Bowie and Freese and these experimental data (both for models containing long cracks) are shown in Figure 5.11. The data of Bowie and Freese have similar trends to those of semi-elliptic data, starting out high then decreasing. However, instead of flattening out, they begin to rise again for *a/t* greater than about 0.2. The experimental data are expected to have similar trends to those of their semi-elliptic counterparts. However, as noted earlier, the exact opposite trend is noted, where they start out low and then increase to a relatively constant value. The use of the shape factor *Q* in the normalization scheme is believed to be one of the reason for this discrepancy. It was assumed that the shape factor would be sufficient for normalizing. However, factors used for normalizing that don't actually represent the case in hand can lead to erroneous results. For instance, compare the cross section of the actual cracked region to that of the assumed semi-ellipse. When using the shape factor in normalization, the actual area is underestimated by 15.5% for the shallowest crack and 12% for the deepest crack. This is illustrated in Figure 5.12, which shows a scaled drawing of the actual cross section and the corresponding semi-elliptic cross section for both the shallow and deep cracks. The result of using the shape factor for normalization is that it underestimates the shape of the crack, which in turn does not correctly emphasize the importance of the geometry in the problem. Since there is some question as to what is appropriate for normalizing this geometry, it proves to be more advantageous to compare a normalized SIF containing the geometric effects. This is shown in Figure 5.13 where

the SIF with divided pressures is plotted versus *a/t* for the experimental and numerical cases of a long crack in a cylinder. These results show the experimental data more closely match the trends of the numerical data, with the magnitude increasing as *a/t* increases. However, this still does not take into account the geometric differences and is not at all adequate for comparisons made between different crack types. Therefore, for comparison sake, the shape factor Q was retained between the long and short cracks.

From the analytic solutions, a linear relation has been hypothesized for determining the plane strain estimation for the normalized SIF in a finned cylinder, F_{PSE}. Namely,

$$F_{PSE} = F_{EXP} \frac{F_{BF}}{F_{GKD}} \tag{5.1}$$

where F_{EXP} is the experimental result from the V-cut crack in a finned model, and F_{BF}/F_{GKD} is the ratio of corresponding Bowie and Freese's plane strain solution and GKD's semi-elliptic solution. Table 5-4 shows data for the experimental, numerical, and plane strain estimation cases. Clearly, the data for the plane strain estimation are higher than the corresponding V-cut case, thus representing a worst case scenario for a crack in a finned cylinder. The plane strain case may be the most extreme case, but experiments have shown it is not the most likely situation. Tests performed with semi-elliptic cracks in finned cylinders have shown that when the crack grows and penetrates the outer boundary, it grows only slightly more while still retaining its semi-elliptic shape. This leads to the conclusion that the extreme case of plane strain is conservative and does not accurately represent the physical situation. Therefore, using a semi-elliptic crack in motor grain design is more appropriate.

5.5 Summary

In order to better understand the influence of an internal surface crack on a thick-walled six-finned cylinder, some photoelastic analysis has been completed. From the

results of these tests and their comparison with analytical solutions, several conclusions can be drawn and are summarized as follows:

- The cracks grew in a self-similar manner (i.e., $a/c \approx$ constant).
- The normalized SIF values for the long V-cut cracks were equal to or greater than those of the semi-elliptic cracks of the same depth.
- Shallow cracks are dominated by internal boundary effects; as a result, the normalized SIF for a shallow V-cut crack is essentially equal to that of a shallow semi-elliptic crack a finned cylinder.
- Variations of normalized SIF along the crack border of a V-cut crack in a finned cylinder decrease only slightly as one moves away from the center. As a result, this case only loosely approximates plane strain.
- Normalized SIF for experimental results from semi-elliptic cracks in finned cylinders shows similar trends to the numerical work from their circular cylinder counterparts. The normalized SIF starts out high for small a/t and decreases by 12.5% to a relatively flat region for a/t between 0.2 and 0.6.
- Using the shape factor Q on a crack front that is not semi-elliptic in shape results in a normalization that does not correctly take into account geometric effects in cylinders with long cracks, such as the V-cut-finned cylinder. As a result, care must be taken in the interpretation of these results.

- From the comparisons between numerical and experimental data, a simple linear relationship was developed for estimating the plane strain in a cracked-finned cylinder. SIFs are highest for this case, and as such, this solution constitutes the worst case scenario for a cracked fin.
- Tests where model penetration has occurred show that under normal loading conditions, a crack will propagate to the boundary and stop growth shortly after penetration, while remaining approximately semi-elliptic in shape. As a result, the use of a semi-elliptic crack in motor grain design should prove to be more realistic and accurate.

6 References

1 Atluri, S.N., and Kathiresan, K.: *3D Analysis of Surface Flaws in Thick-Walled Reactor Pressure Vessels Using Displacement-Hybrid Finite Element Method,* Nuclear Engineering and Design, vol. 51, pp. 163-176, 1979.

2 Bowie, O.L. and Freese, C.E.: *Elastic Analysis for a Radial Crack in A Circular Ring,* Engineering Fracture Mechanics, vol. 4, pp. 315-321, 1972.

3 Bunker, H.F.: *A Novel Principal for the Computation of Stress Intensity Factors*, Z. Angewandte Mathemat. Mechan., vol. 50, no. 9, pp. 529-546, 1970.

4 Dally, J.W., and Riley, W.F.: *Experimental Stress Analysis: Second Edition,* New York: McGraw-Hill, pp. 339-521, 1978.

5 Epstein, J.S.: *On the Variation of the First Classical Eigenvalue of Fracture Mechanics in the Three Dimensional Transitory Stress Field,* Ph.D. Dissertation, Virginia Tech, 1983.

6 Epstein, J.S., Post, D., and Smith, C.W.: *Three Dimensional Photoelastic Measurements with Very Thin Slices,* Experimental Techniques, pp. 34-37, Dec. 1984.

7 Francis, E.C., Lindsey, G.H., and Parmertrer, R.R.: *Pressurized Crack Behavior in Two-Dimensional Rocket Motor Grains*, Journal of Spacecraft, vol. 9, no. 6, pp. 415-419, June 1972.

8 Francis, E.C. et al.: *Viscoelastic Fracture of Solid Propellant in Pressurization Loading Conditions,* Journal of Spacecraft, vol. 11, no. 10, pp. 691-696, 1974.

9 Gouzhong, C., Kangda, Z., and Dongdi, W.: *Stress Intensity Factors for Internal Semi-Elliptical Surface Cracks in Pressurized Thick-Walled Cylinders using the Hybrid Boundary Element Method,* Engineering Fracture Mechanics, vol. 52, no. 6, pp. 1055-1064, 1995.

10 Hult, J.: *On the Measurement of Stress in Solids,* Trans. Chalmers Univ. of Tech., Gothenburg, Sweden, no. 280, 1963.

11 Irwin, G.R.: *Fracture I*, in S. *Flugge (ed.) Handbunch der Physik VI*, Springer-Verlag, New York, pp. 558-590, 1958.

12 Irwin, G.R.: *Crack Extension Force for a Part Through Crack in a Plate,* Journal of Applied Mechanics, Trans. ASME Series E, vol. 29, no. 8, pp. 265-268, Dec. 1962.

13 Kirkhope, K.J., Bell, R., and Kirkhope, J.: *Stress Intensity Factor Equations for Single and Multiple Cracked Pressurized Thick-Walled Cylinders*, Int. J. Pres. Ves. & Piping, vol. 41, pp. 103-111, 1990.

14 Maxwell, J.C.: *On the Equilibrium of Elastic Solids*, Trans. R. Soc. Edinburgh, vol. XX, part 1, pp. 87-120, 1853.

15 Mindlin, R.D.: *Analysis of Doubly Refracting Materials with Circularly and Elliptically Polarized Light*, J. Opt. Soc. Am., vol. 27, pp. 288-291, 1937.

16 Mindlin, R.D.: *A Review of the Photoelastic Method of Stress Analysis*, J. Appl. Phys., vol. 10, pp. 222-241and 273-294, 1939.

17 Newman, J.C. Jr.: *Fracture Analysis of Surface and Through Cracked Sheets and Plates,* Journal of Engr. Frac. Mech., vol. 5, no. 3, p. 686, Sept. 1973.

18 Oppel, G.: *Polarisationsoptische Untersuchung Raumlicher Spannungs - und Dehnungszustande*, Forsch. Gerb. Ingenieurw., vol. 7, pp. 240-248, 1936.

19 Parker, A.P.: *The Mechanics of Fracture and Fatigue: An Introduction,* New York: E. & F. N. Spoon Ltd., pp. 49-88, 1981.

20 Post, D.: *Isochromatic Fringe Sharpening and Fringe Multiplication in Photoelasticity*, Proc. SESA, vol. XII, no. 2, pp. 143-156, 1955.

21 Post, D.: *Photoelastic Evaluation of Individual Principal Stresses by Large Field Absolute Retardation Measurements*, Proc. SESA, vol. XIII, no. 2, pp. 119-132, 1956.

22 Post, D.: *Fringe Multiplication in Three-dimensional Photoelasticity*, J. Strain Analysis, vol. 1, no. 5, pp. 380-388, 1966.

23 Raju, I.S., and Newman, J.C. Jr.: *Stress-Intensity Factors for Internal and External Surface Cracks in Cylindrical Vessels,* Journal of Pressure Vessel Technology, vol. 104, pp. 293-298, November 1982.

24 Rastrelli, L.U., and DeHart, R.: *Measurements of Strain in Solid Propellant Grains,* JANNAF 20th meeting Bull., vol. II, 1961.

25 Rice, J.R.: *Some Remarks on the Elastic Crack-tip Stress Fields*, Int. J. of Solids Structures, vol. 8, no. 6, pp. 751-758, 1972.

26 Shen, G., and Glinka, G.: *Weight Functions for a Semi-Elliptical Crack in a Finite Thickness Plate*, Theoretical and Applied Fracture Mechanics, vol. 15, pp. 247-255, 1991.

27 Smith, C.W.: *Use of Three Dimensional Photoelasticity and Progress in Related Areas*, Experimental Techniques in Fracture Mechanics, ch. 1, SESA monograph, no. 2, pp. 3-58, 1975.

28 Smith, C.W., Constantinescu, D.M., and Liu, C.T.: *SIF Distributions in Cracked Photoelastic Rocket Motor Studies; Preliminary Results,* Proceedings of the SEM Annual Conference on Experimental and Applied Mechanics, pp.105-108, June 2001.

29 Smith, C.W., Constantinescu, D.M., and Liu, C.T.: *Stress Intensity Factors and Crack Paths for Cracks in Photoelastic Motor Grain Models,* Proceedings of ASME International Mechanical Engineering Conference and Exposition, IMECE2002-32078, pp.1-8, 2002.

30 Smith, C.W., Hansen, J.D., and Liu, C.T.: *Preliminary Experiments for Evaluating 3-D Effects on Cracks in Frozen Stress Models,* Proceedings of ASME International Mechanical Engineering Congress and Exposition, IMECE2003-43489, 2003.

31 Sutton, G.P.: *Rocket Propulsion Elements,* John Wiley & Sons, p. 287, 1986.

32 Tan, C.L., and Fenner, R.T.: *Elastic Fracture Mechanics Analysis by the Boundary Integral Equation Method,* Proc. R. Soc. London, A 369, pp. 243-260, 1979.

33 Tardy, M.H.L.: *Methode Pratique d'examen de Measure de la Birefringence des Verres d'optique*, Rev. Opt., vol. 8, pp. 59-69, 1929.

34 Wang, L.: *Investigations into Deep Cracks in Rocket Motor Propellant Models,* Masters Thesis, Virginia Tech, 1990.

35 Westergaard, H.M.: *Bearing Pressures and Cracks,* Journal of Applied Mechanics, vol. 61, pp. A49-A53, 1939.

36 Wilson, H.B. Jr.: *Stresses Owing to Internal Pressure in Solid Propellant Rocket Grains,* ARS Journal, vol. 31, no. 3, pp. 309-317, March 1961.

37 Yan, A.M., and Dang, H.N.: *Stress Intensity Factors and Crack Extension in a Cracked Pressurized Cylinder,* Engineering Failure Analysis, no. 4, pp. 307-315, 1994.

38 Zheng, X.J., Glinka, G., and Dubey, R.N.: *Calculation of Stress Intensity Factors for Semi-Elliptical Cracks in a Thick-Wall Cylinder*, Int. Journal of Pressure Vessel and Piping, vol. 62, pp. 249-258, 1995.

39 Zheng, X.J., Kiciak, K., and Glinka, G.: *Weight Functions and Stress Intensity Factors for Internal Surface Semi-Elliptical Cracks in Thick-Walled Cylinder*, Engineering Fracture Mechanics, vol. 58, no. 3, pp. 207-221, 1997.

Appendix A Figures

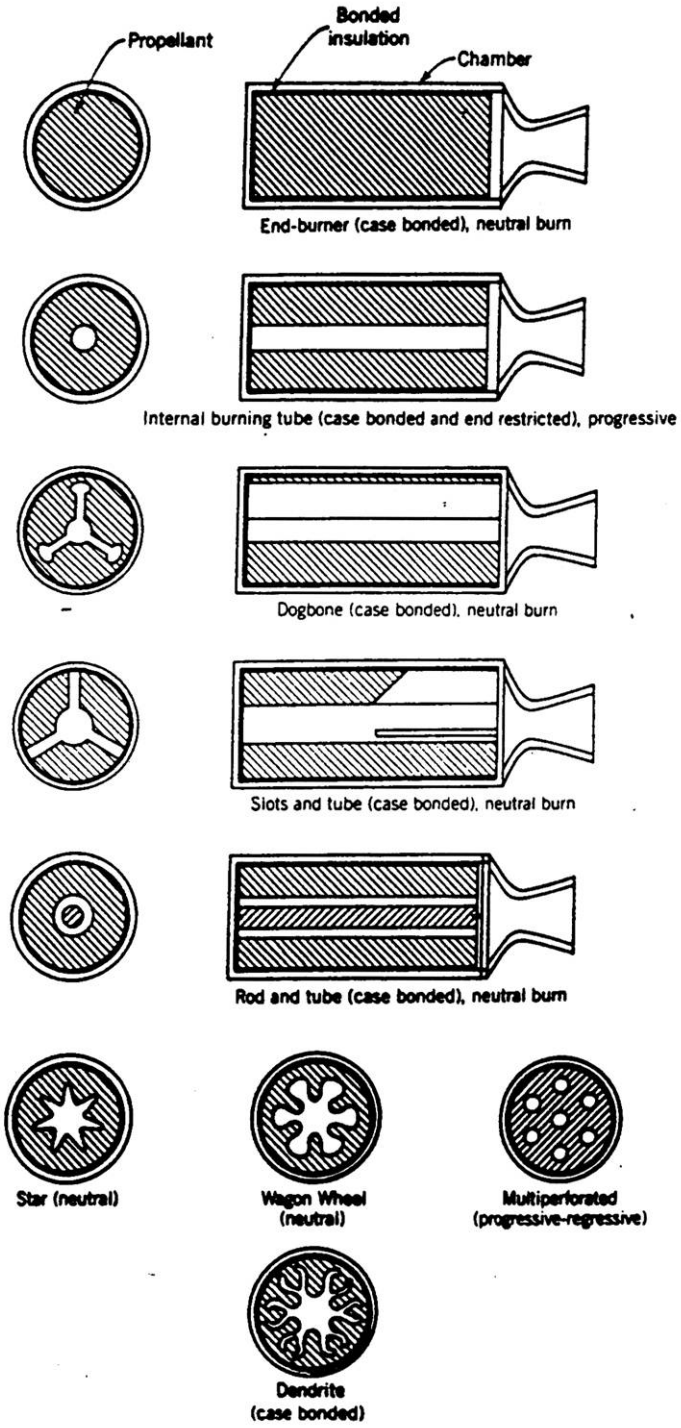

Figure 1.1: Propellant grain geometries. (Adapted from a figure [Sutton 86])

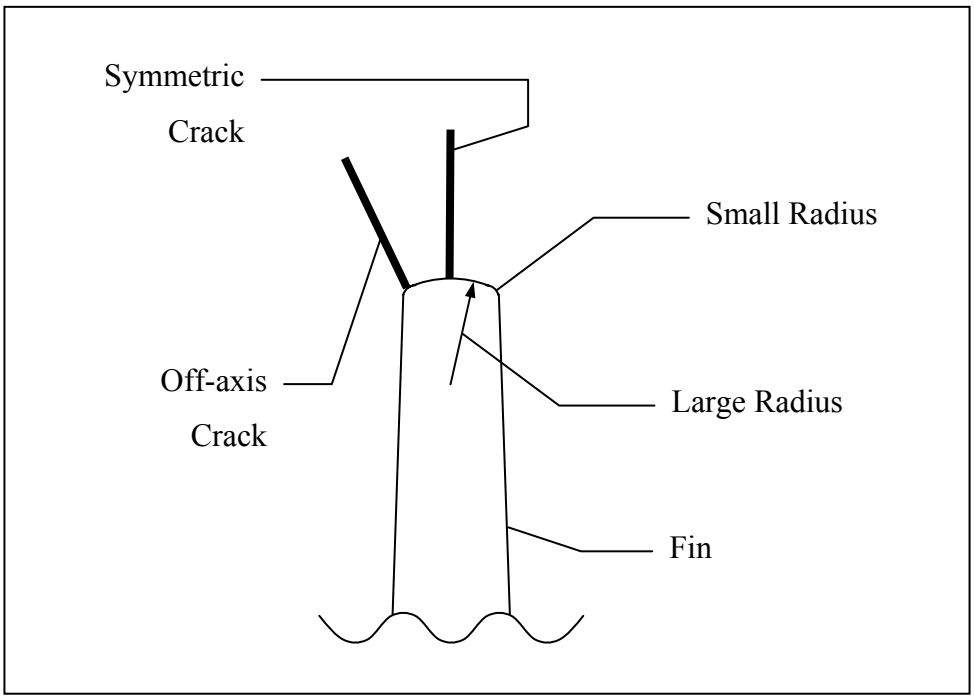

Figure 1.2: Schematic of cracks emanating from the centerline of a fin tip (symmetric crack) and from the coalescence of two radii (off-axis crack).

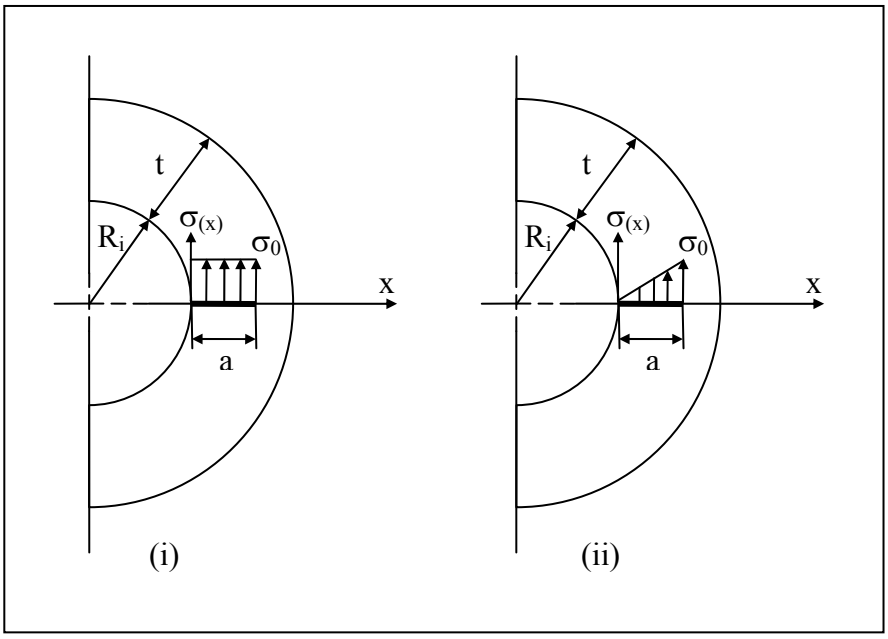

(a)

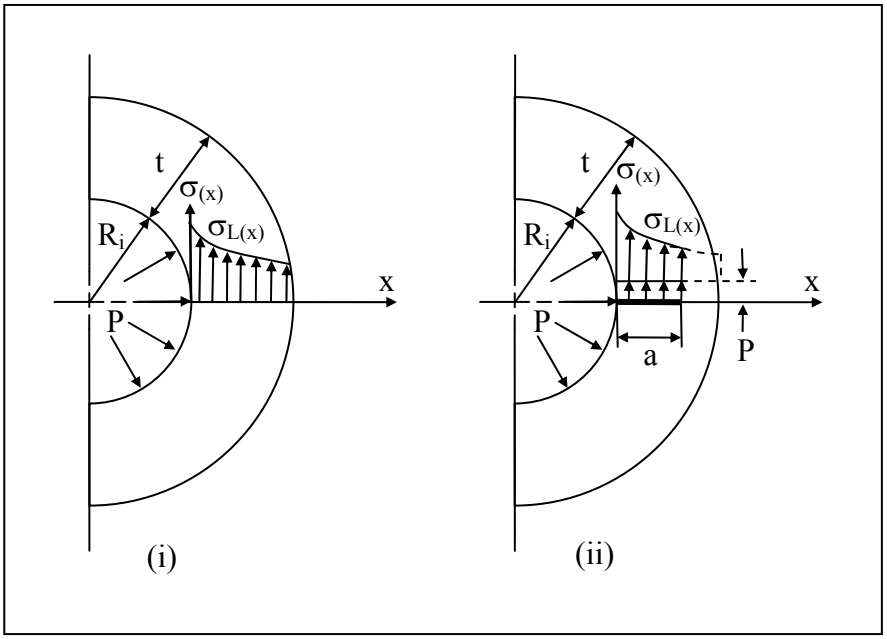

(b)

Figure 2.1: Schematic of (a) a reference stress fields for a semi-elliptic internal surface crack for (i) a uniform tensile stress field and (ii) a linear tensile stress field and (b) a stress distribution due to internal pressure for (i) a Lame stress distribution in a thick walled cylinder and (ii) crack face loading due to pressure. (Adapted from a figure [Zheng, Glinka, and Dubey 95])

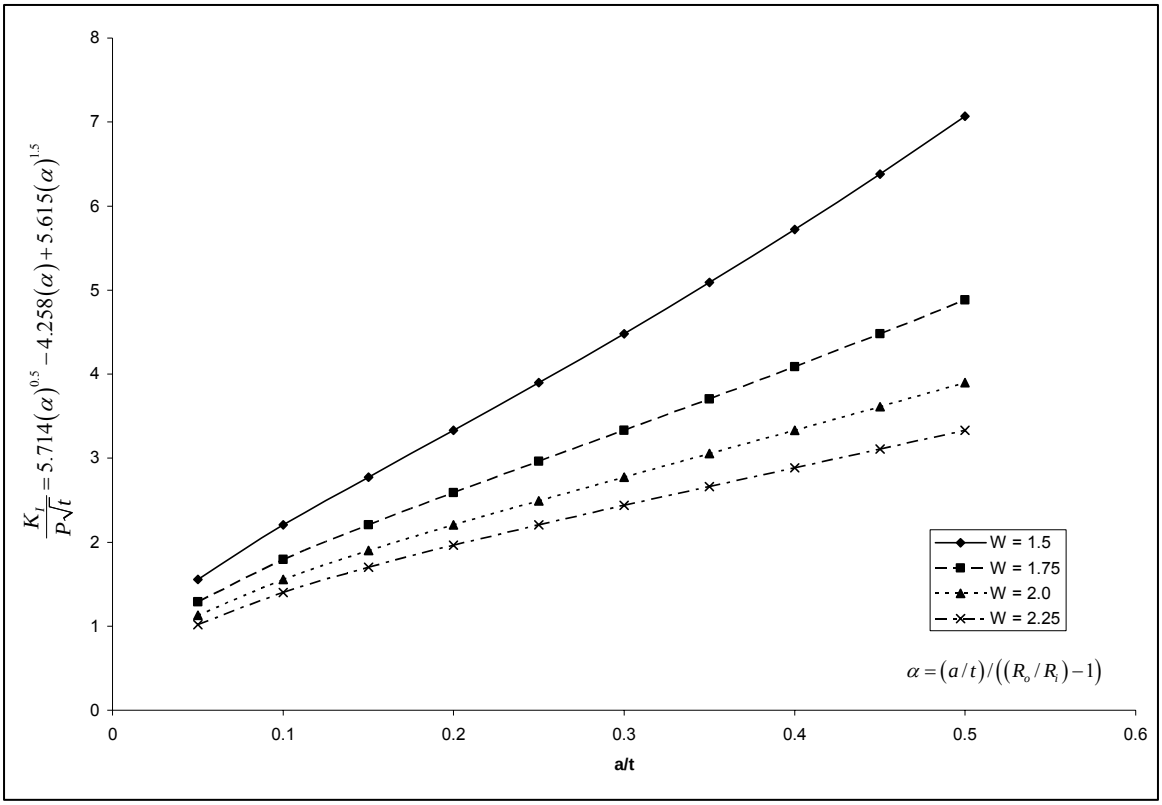

Figure 2.2: Normalized SIF vs. a/t for a long crack in a circular cylinder. (Data from [Kirkhope, Bell, and Kirkhope 90])

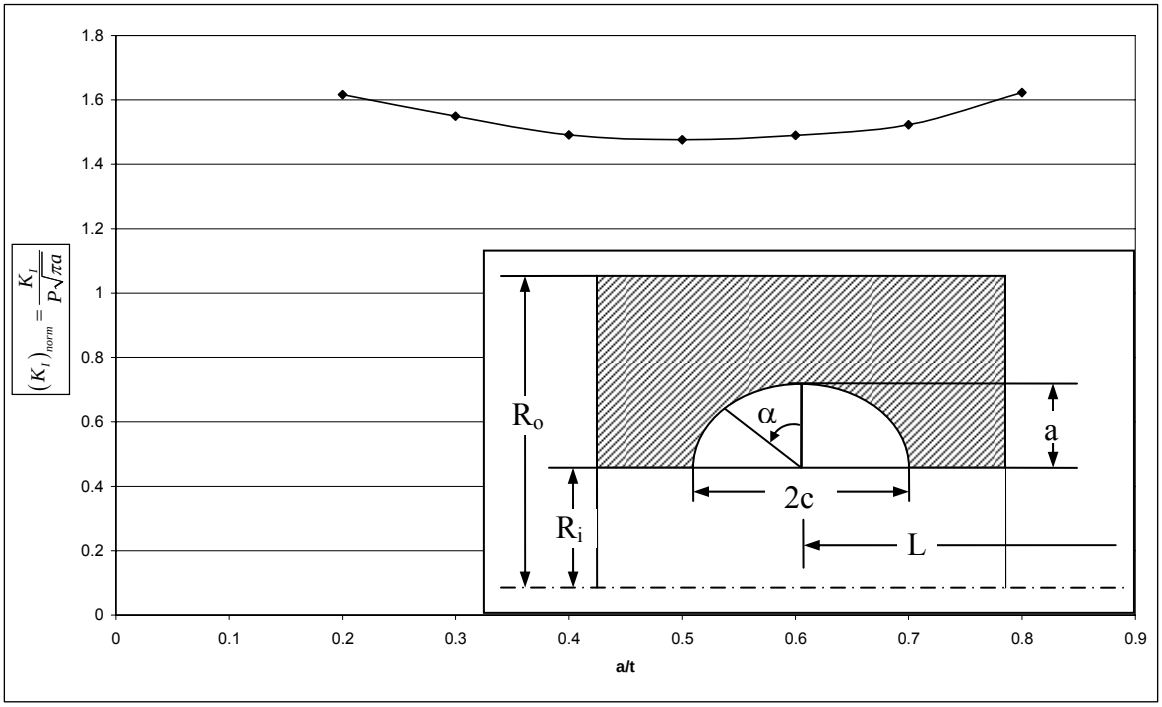

Figure 2.3: Normalized SIF vs. a/t for semi elliptical surface cracks for $\alpha = 0°$, $R_o/R_i = 2$, a/c = 0.8, and $\nu = 0.3$, with crack and specimen geometry. (Data from [Tan and Fenner 79])

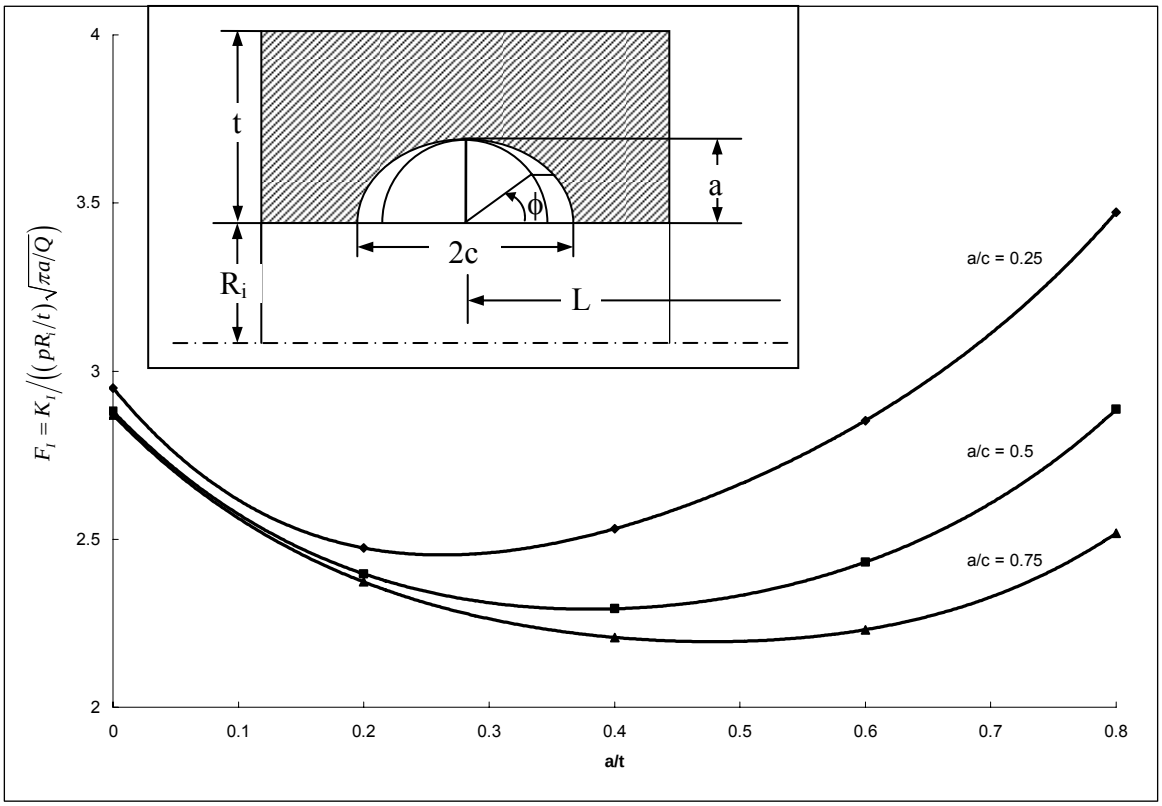

(a) $t/R_i = 1.0$ and geometry used by GKD

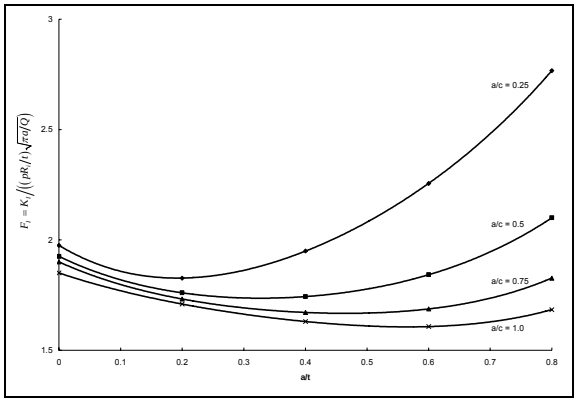

(b) $t/R_i = 0.5$

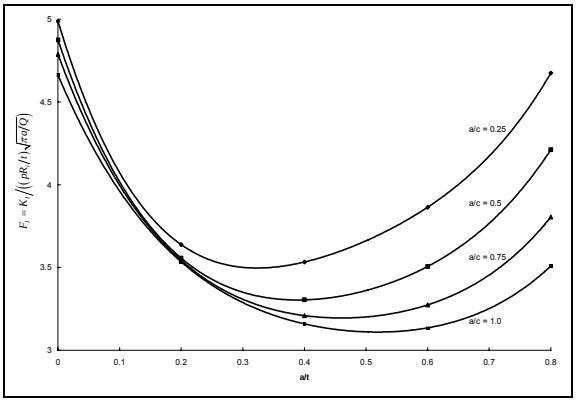

(c) $t/R_i = 2.0$

Figure 2.4: Normalized SIF at $\phi = \pi/2$. (Data from [Gouzhong, Kangda, and Dongdi 95])

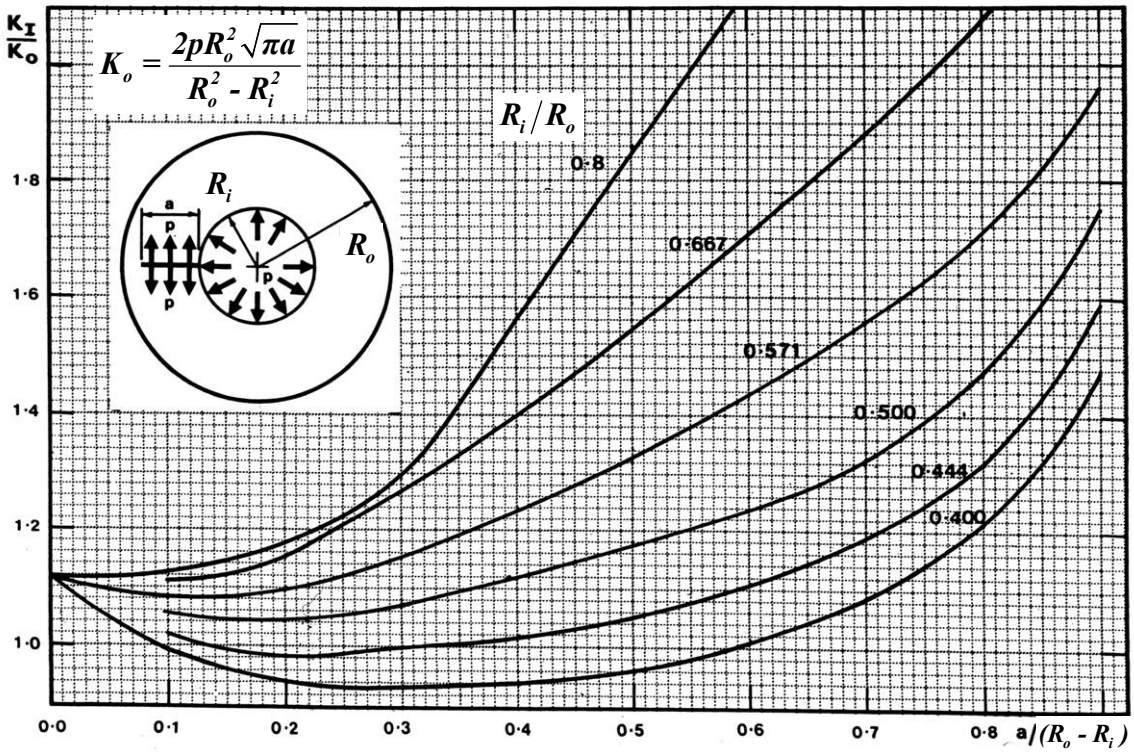

Figure 2.5: Plot of the normalized SIF verses $a/(R_o-R_i)$, plane strain case, with model geometry. (Adapted from a figure [Bowie and Freese 72])

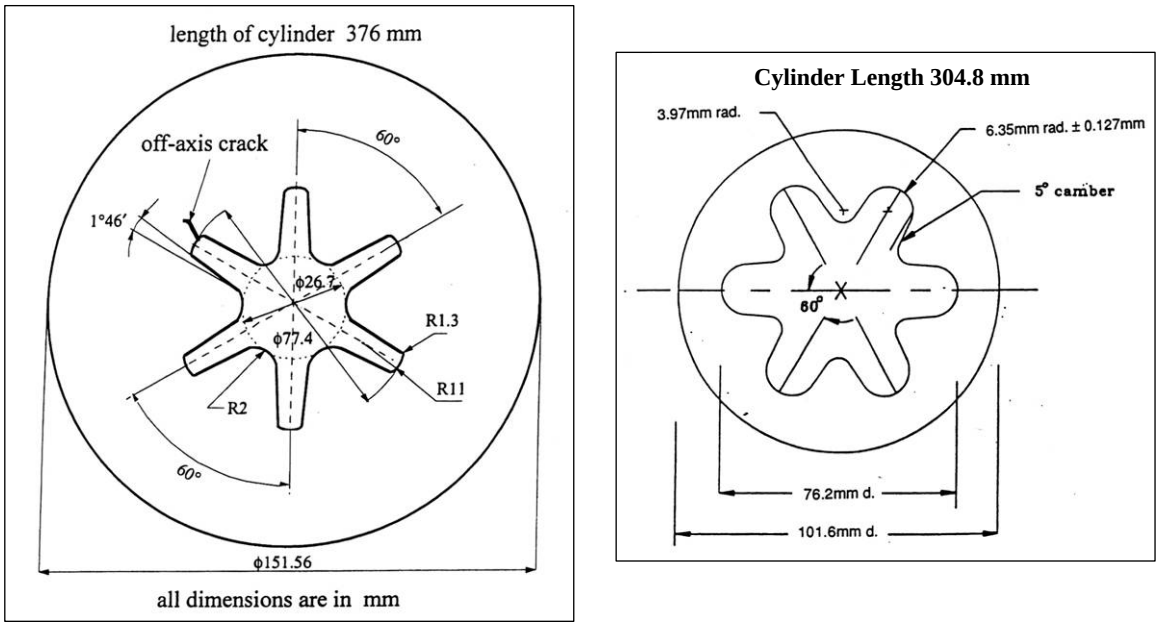

Figure 2.6: Typical geometries used by Smith and his associates in photoelastic analysis. (Adapted from a figure [Smith, Constantinescu, and Liu 02] and [Wang 90])

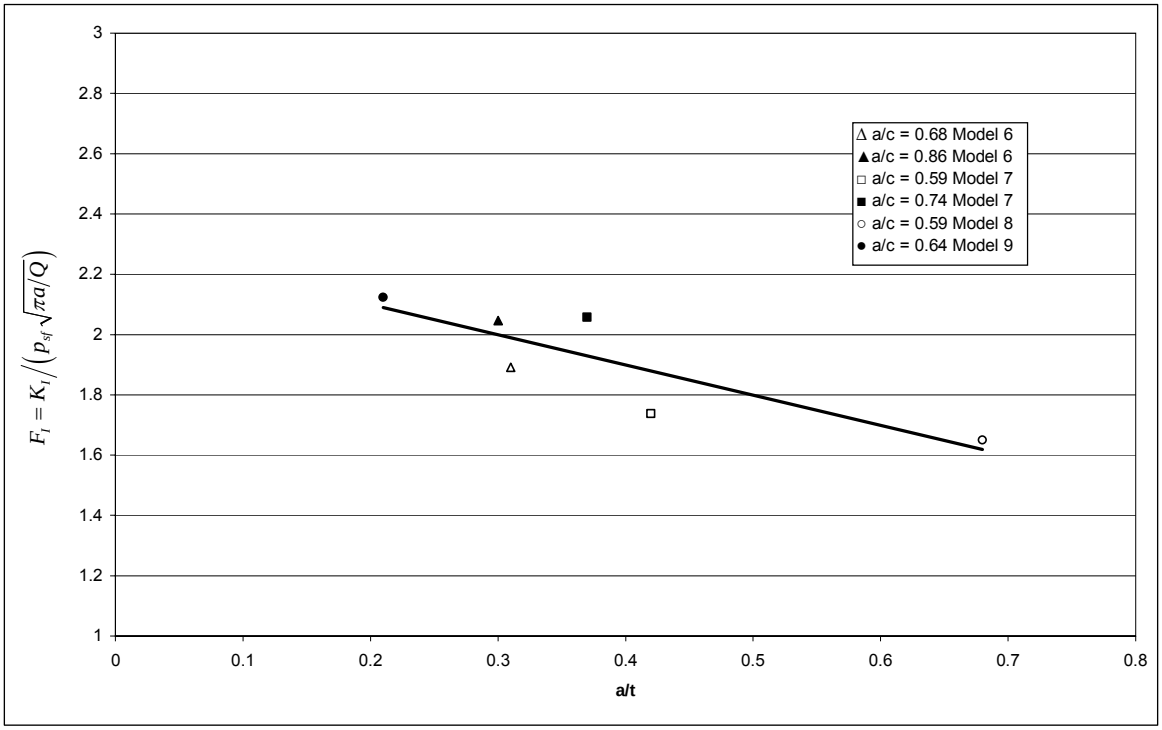

Figure 2.7: Effect of part-through crack depth on normalized SIF for off-axis cracks inserted parallel to the fin axis. (Data from [Smith, Constantinescu, and Liu 02])

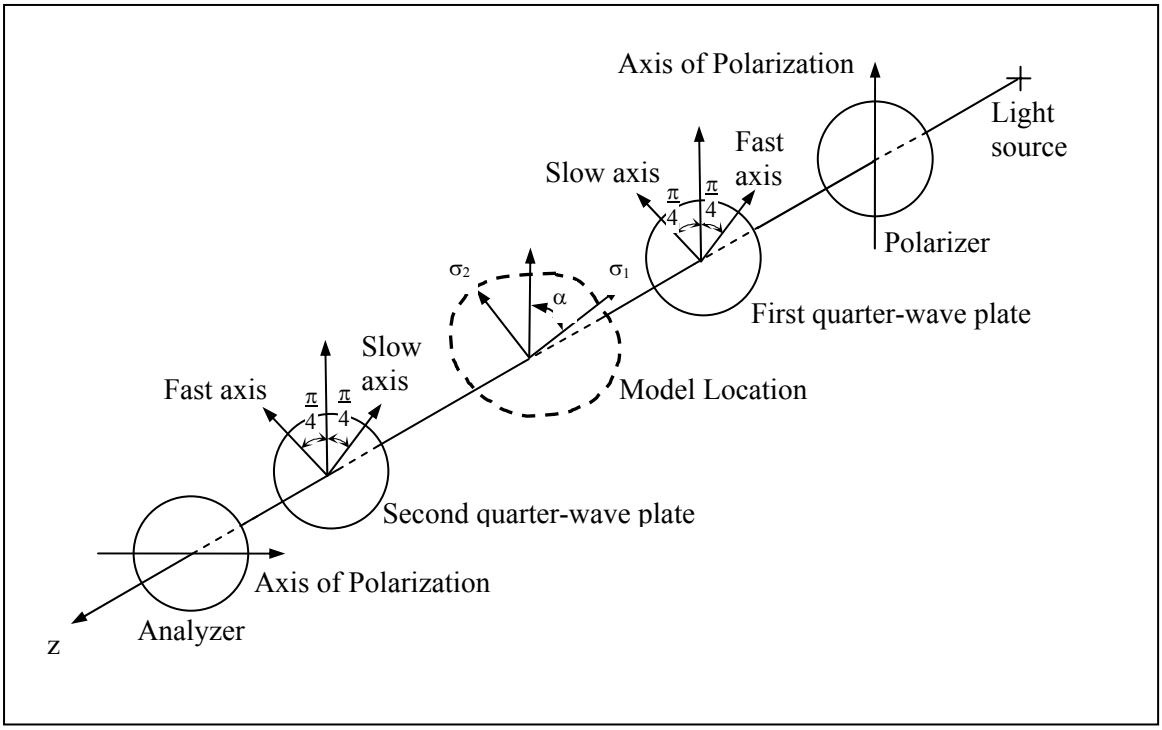

Figure 3.1: Schematic of a circular polariscope setup. (Adapted from a figure [Dally and Riley 78])

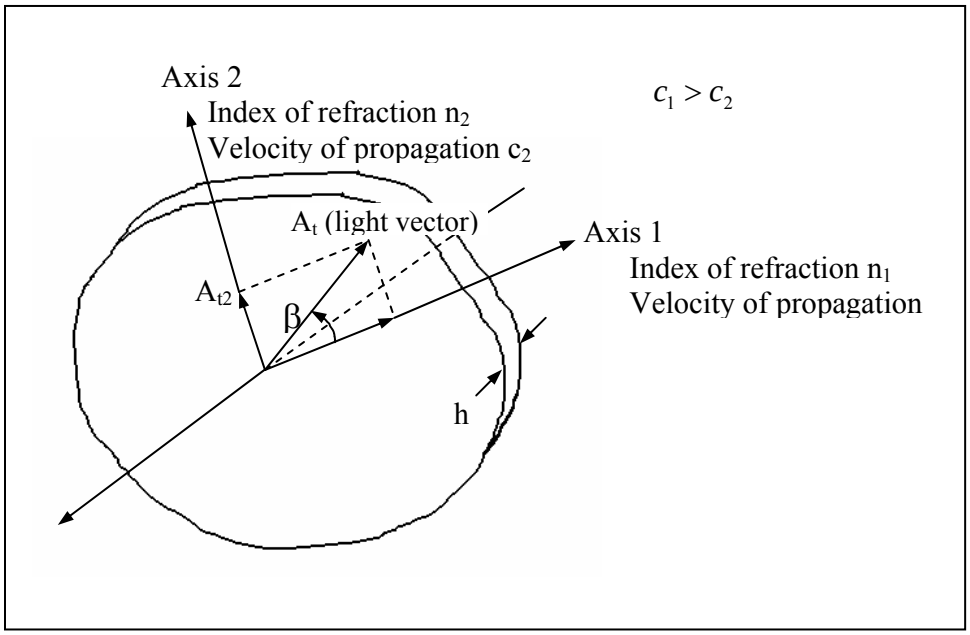

(a)

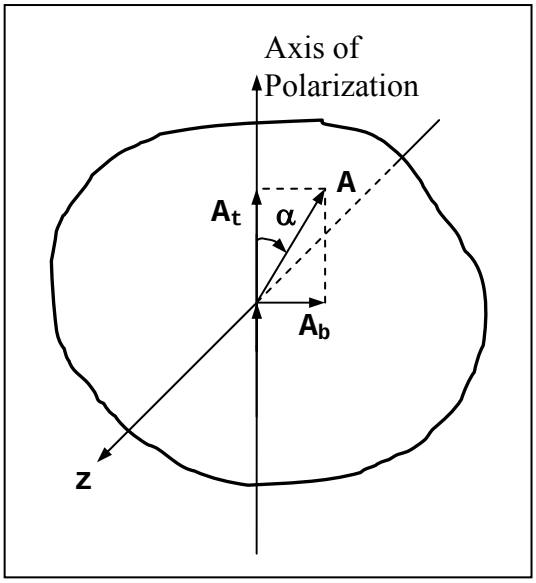

(b)

Figure 3.2: Schematic of (a) Polarizer with axis of polarization in the y-direction (b) Quarter-wave plate (β = π/4). (Adapted from a figure [Dally and Riley 78])

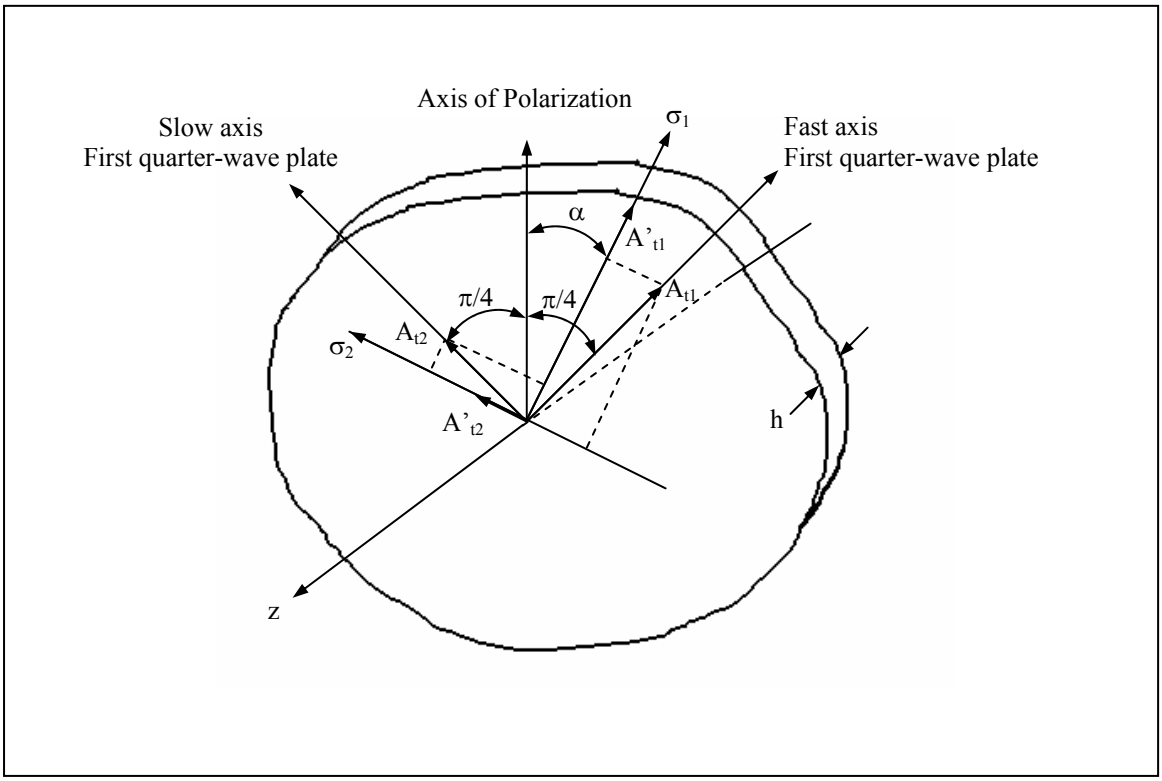

Figure 3.3: Schematic of the decomposition of the light vectors into components along the principal stress directions. (Adapted from a figure [Dally and Riley 78])

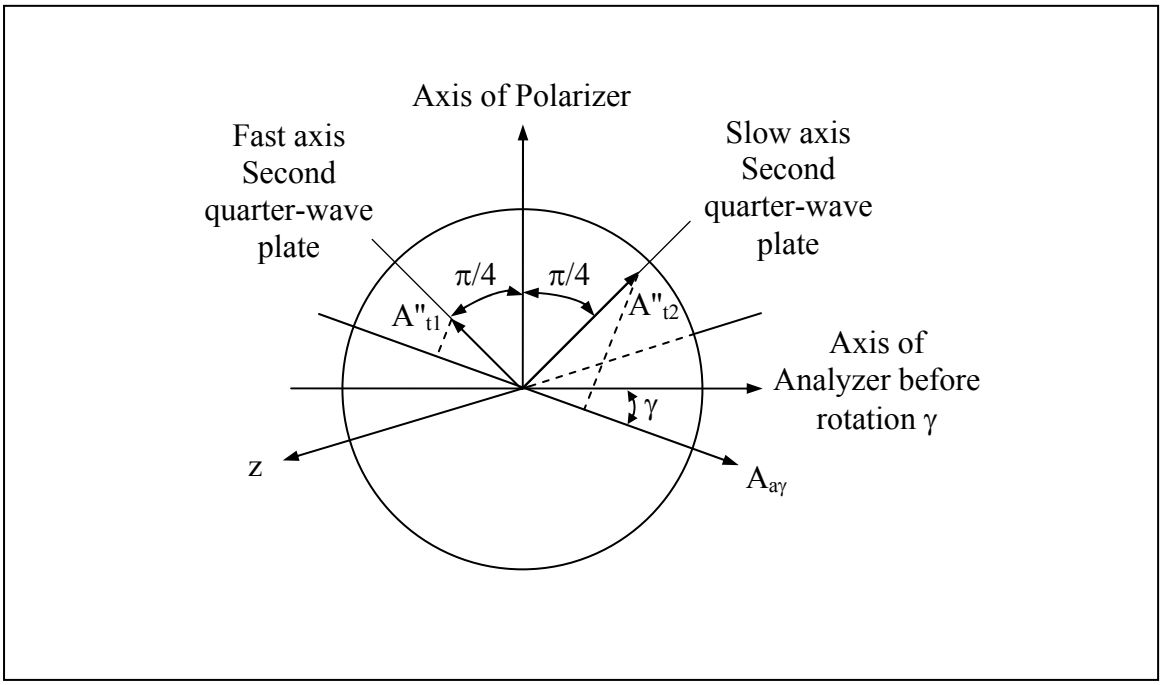

Figure 3.4: Schematic of the analyzer decomposition of the light vectors employing Tardy compensation. (Adapted from a figure [Dally and Riley 78])

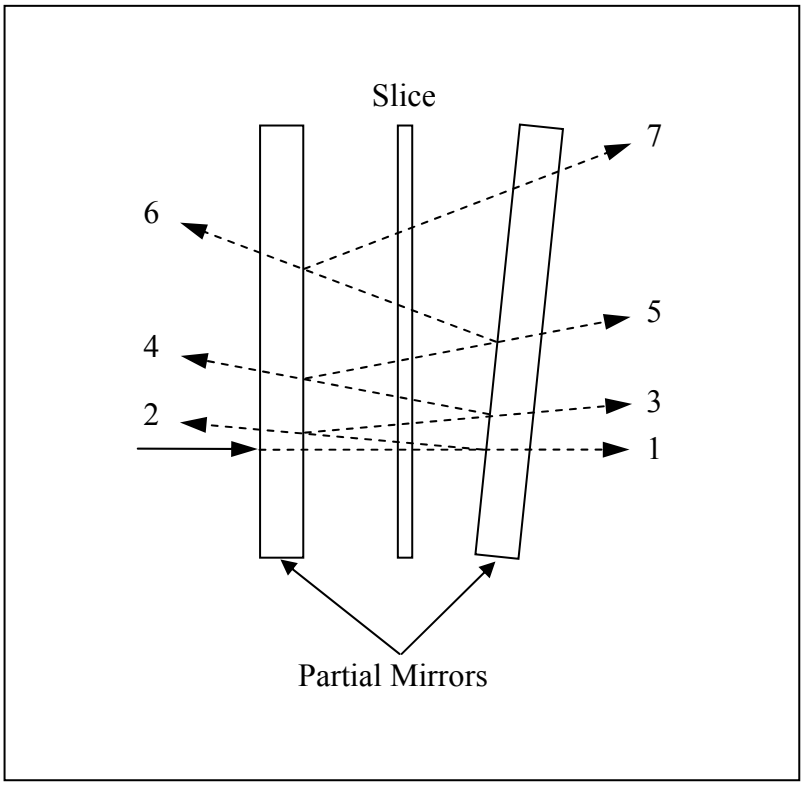

Figure 3.5: Schematic, Post fringe multiplication. (Adapted from a figure [Dally and Riley 78])

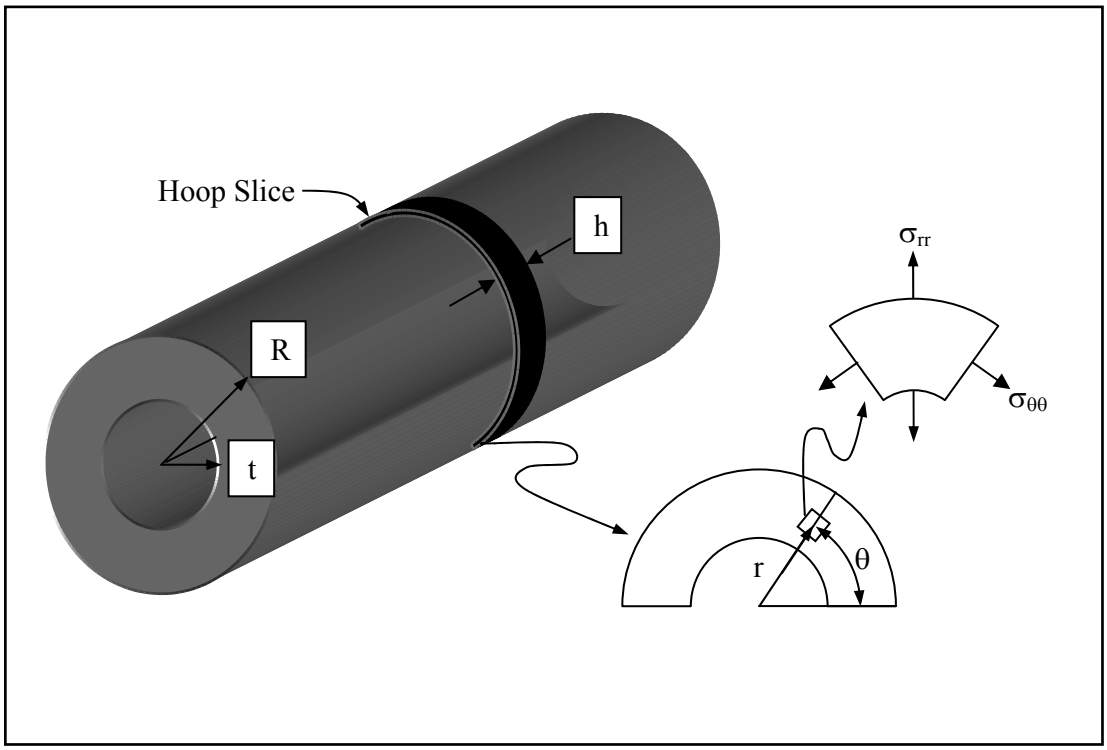

Figure 3.6: Schematic, hoop slice in a circular cylinder.

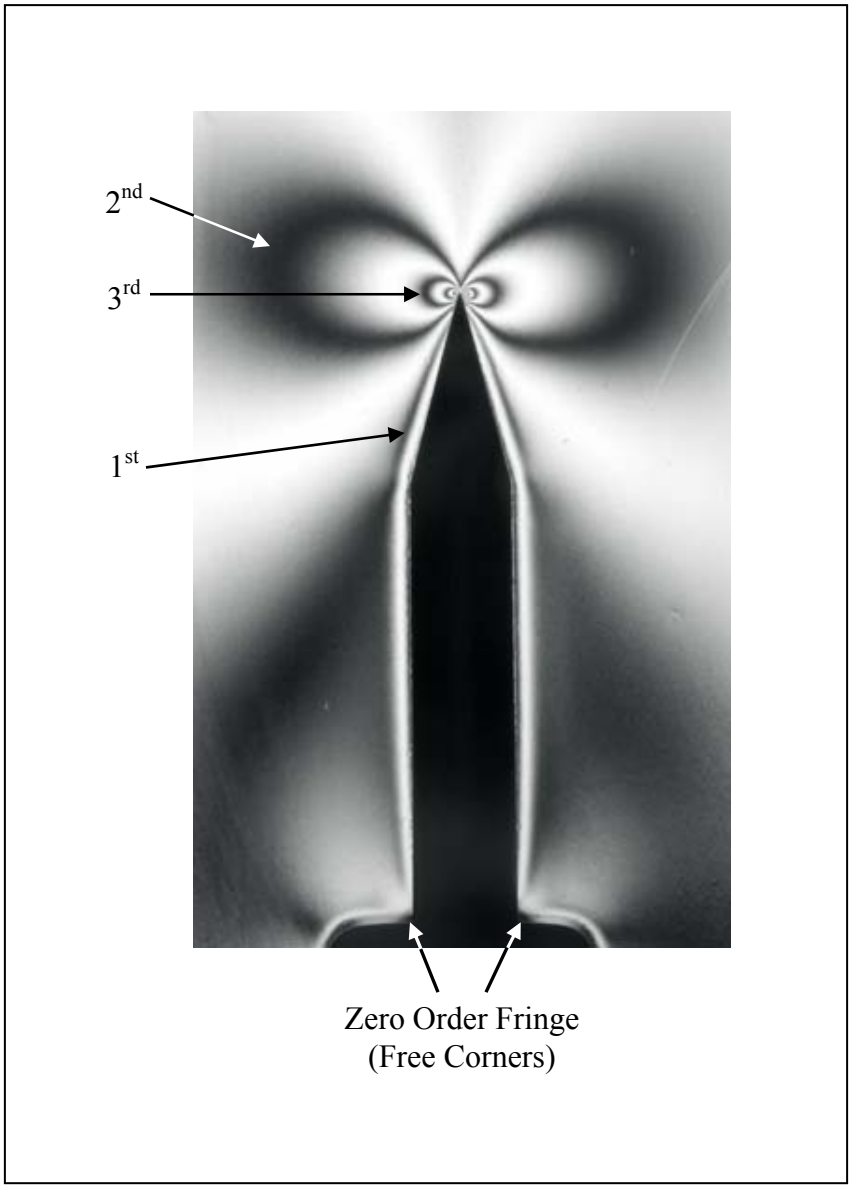

Figure 3.7: Photograph of isochromatic fringe patterns with fringe order locations (6 fringes total), dark field, no fringe multiplication.

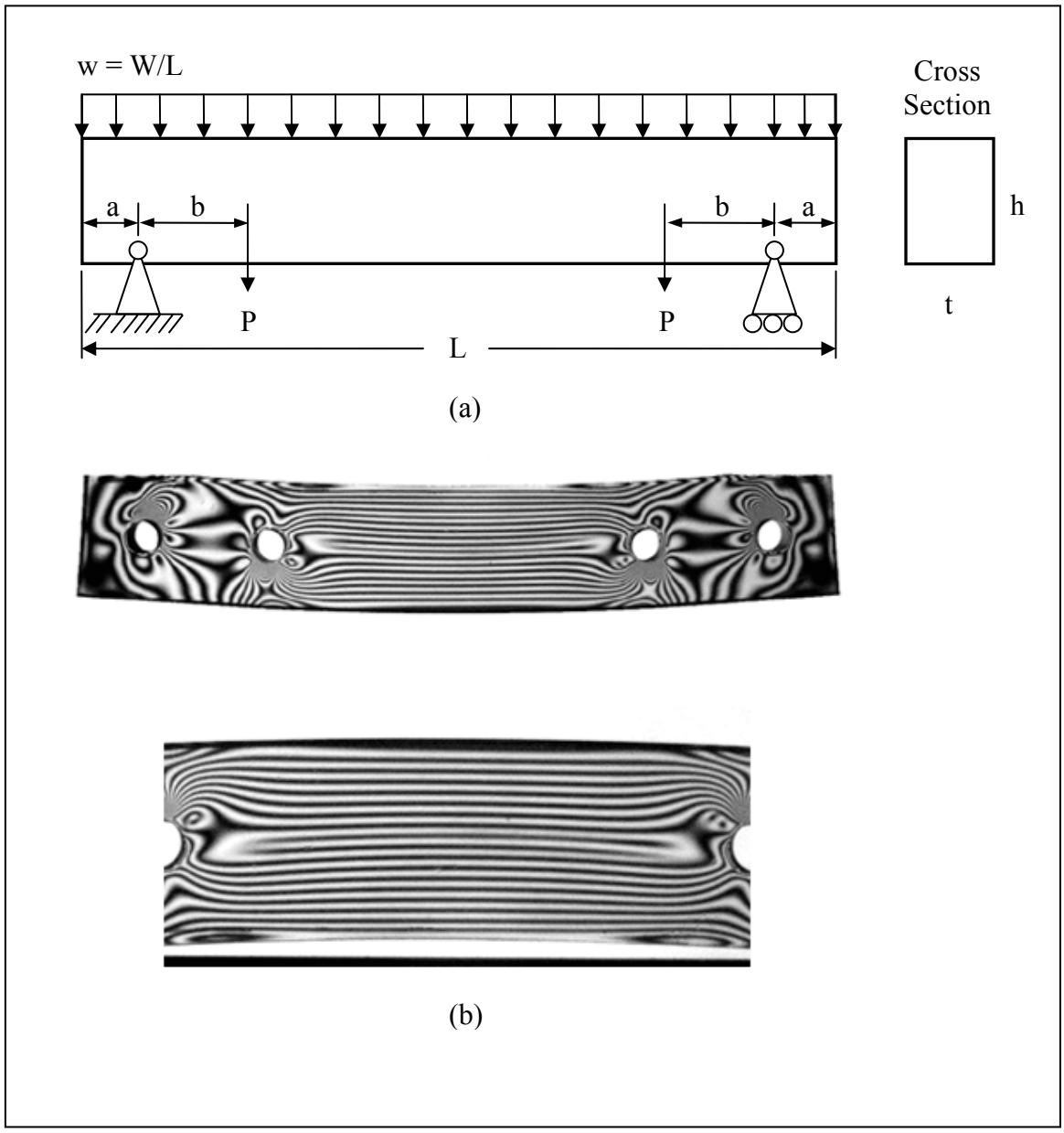

Figure 3.8: (a) Schematic of a calibration beam loading and (b) global and local calibration beam photographs of typical isoclinic fringes patterns.

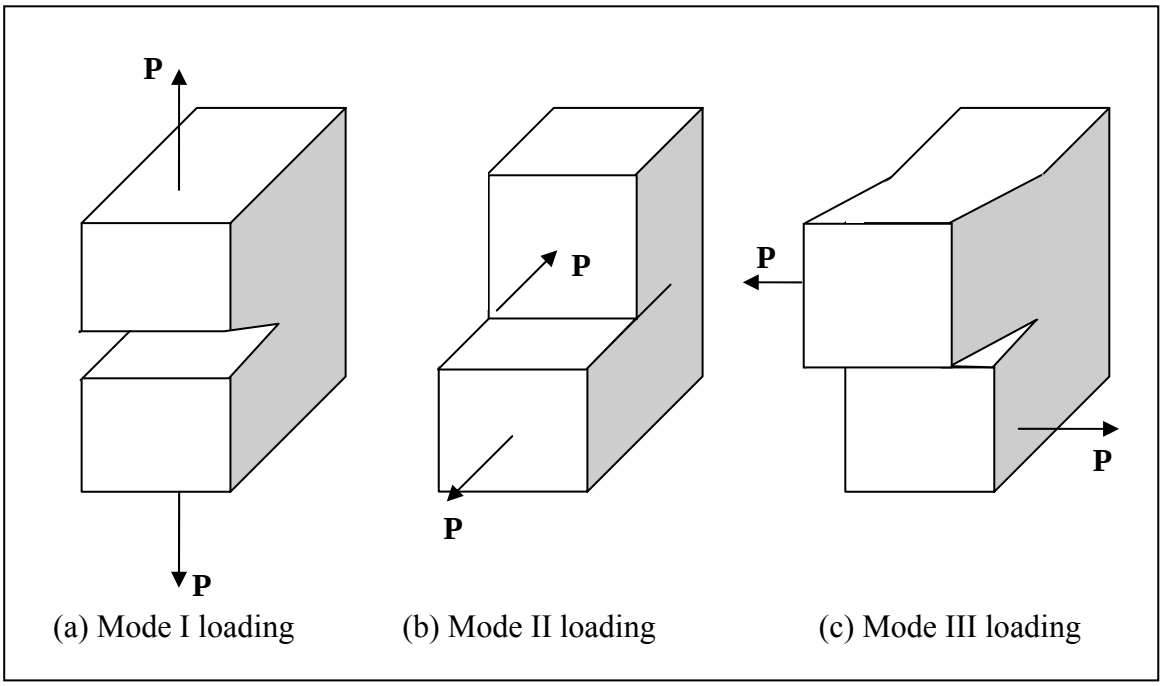

Figure 3.9: Schematic of three possible crack growth modes (a) Mode I – tensile loading, (b) Mode II – in plane shear loading, and (c) Mode III – transverse shear loading.

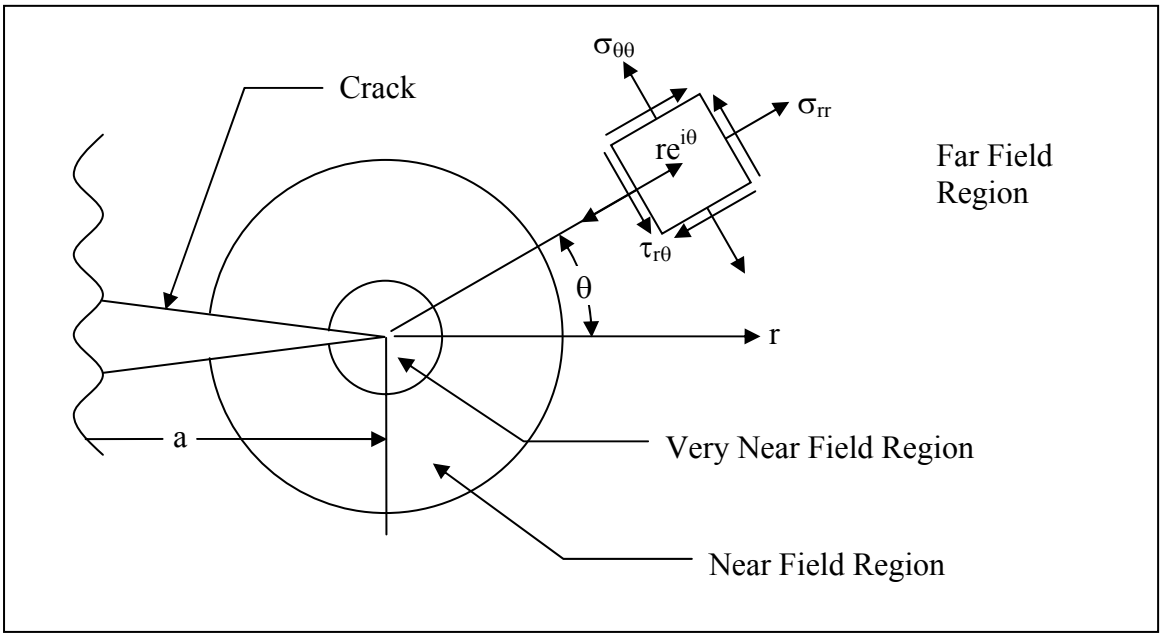

Figure 3.10: Schematic of crack regions and local coordinate system.

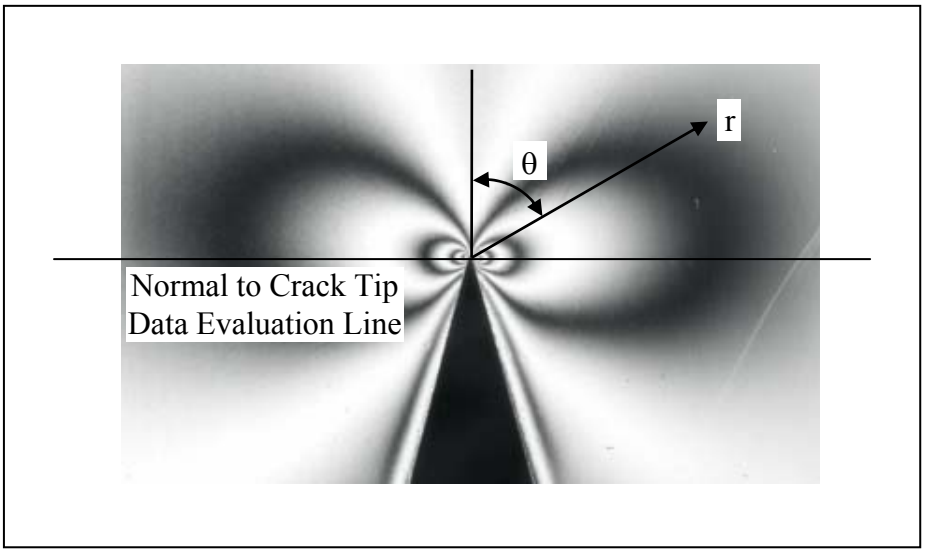

Figure 3.11: Photograph of isochromatic fringe patterns for mode I crack growth, with the isochromatic fringe loops oriented approximately normal to the crack tip.

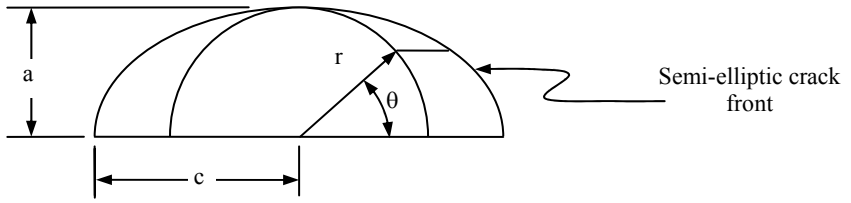

The Stresses:

$$\lim_{r \to o} \sigma_{ij} = \frac{K_I}{\sqrt{2\pi r}} f_{ij}(\theta)$$

The Normalized Stress Intensity Factor:

$$F_{nor} = \frac{K_I}{p\sqrt{\pi a}} \sqrt{Q}$$

The Apparent Stress Intensity Factor:

$$(K_I)_{AP} = \sqrt{8\pi r}\tau_{\max}$$

The Shape Factor:

$$Q = 1 + 1.464\left(\frac{a}{c}\right)^{1.65}$$

Figure 3.12: Schematic of a typical semi-elliptic crack front.

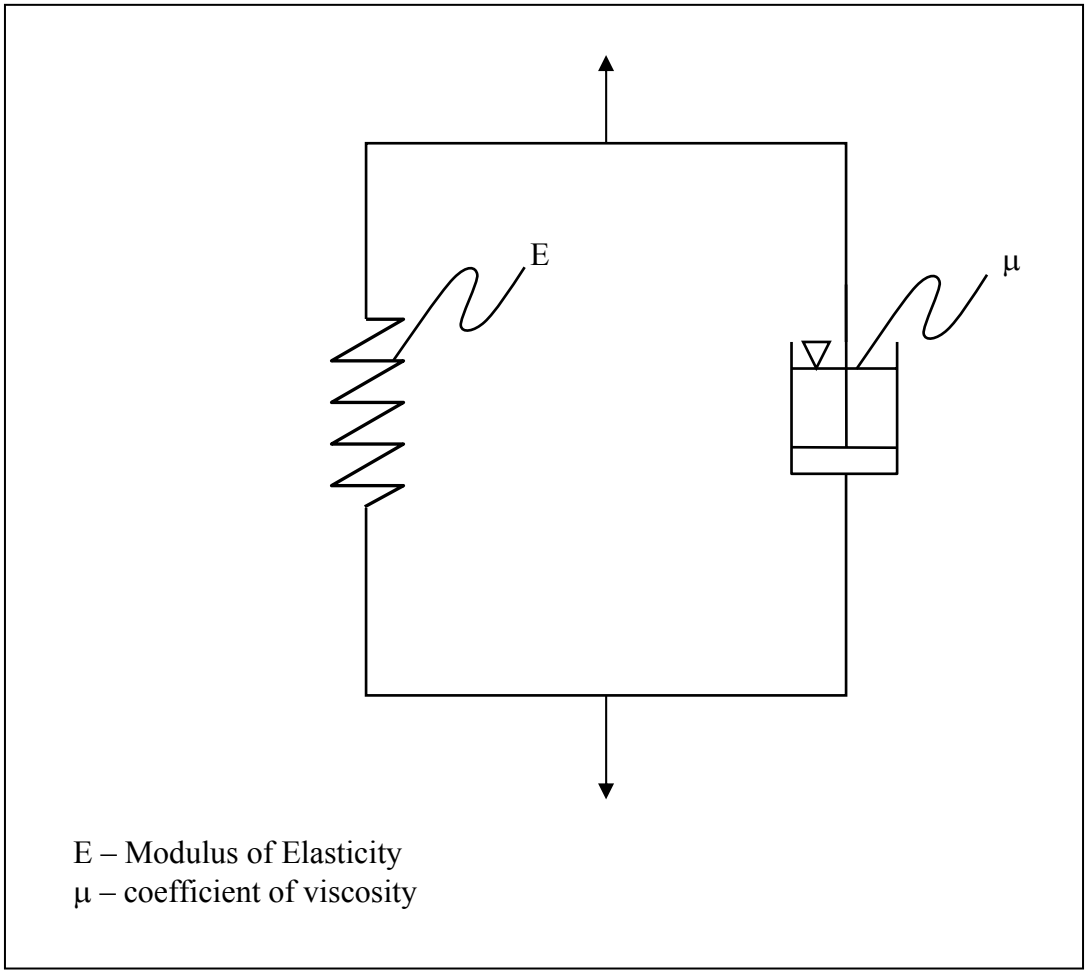

Figure 4.1: Kelvin Model of PLM-4BR solid at room temperature.

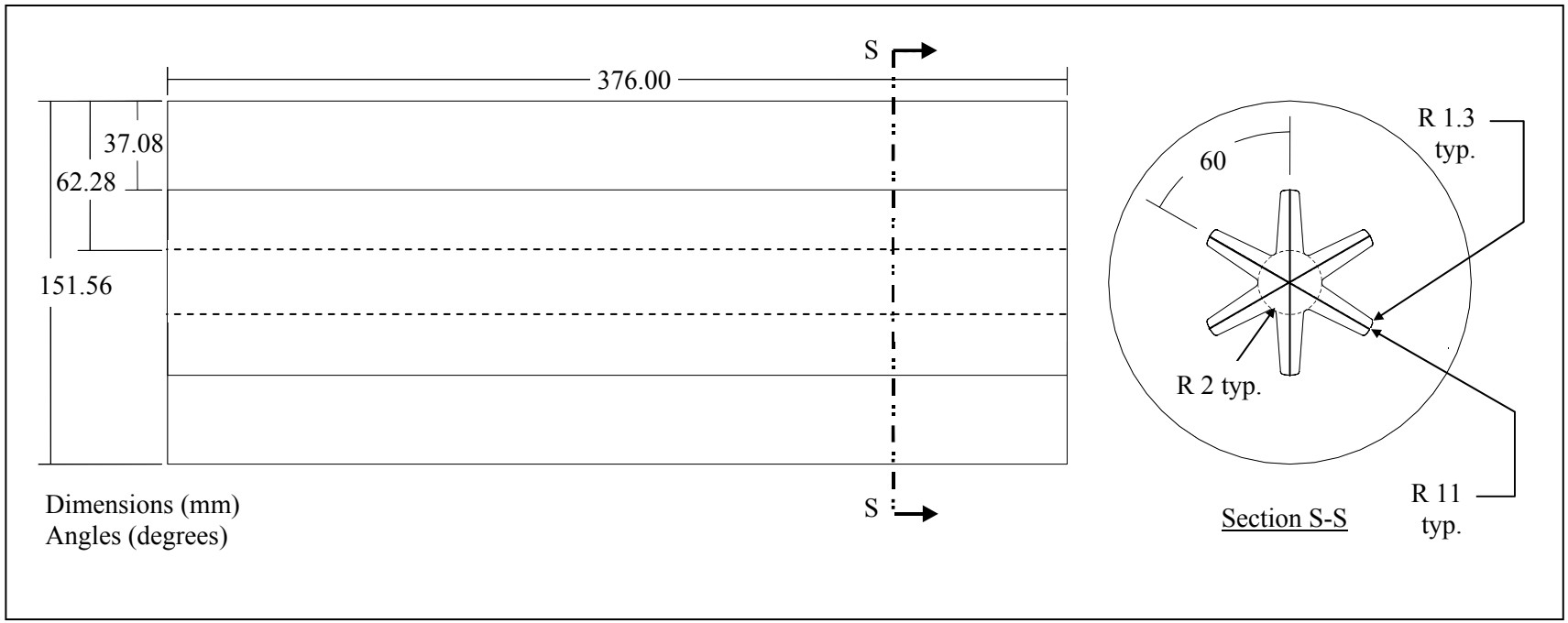

Figure 4.2: Schematic of the internal star circular cylinder.

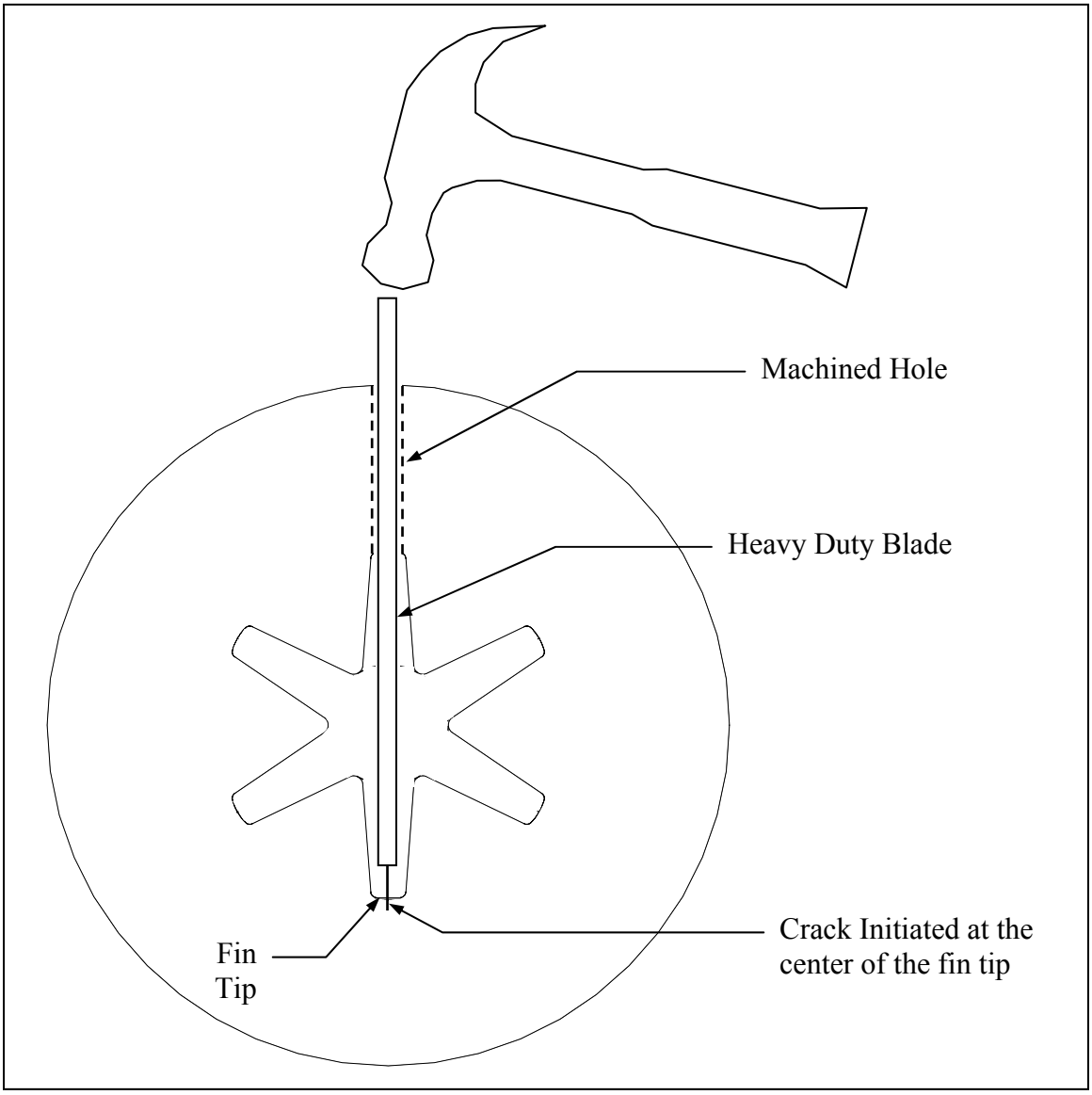

Figure 4.3: Schematic, longitudinal natural crack initiation.

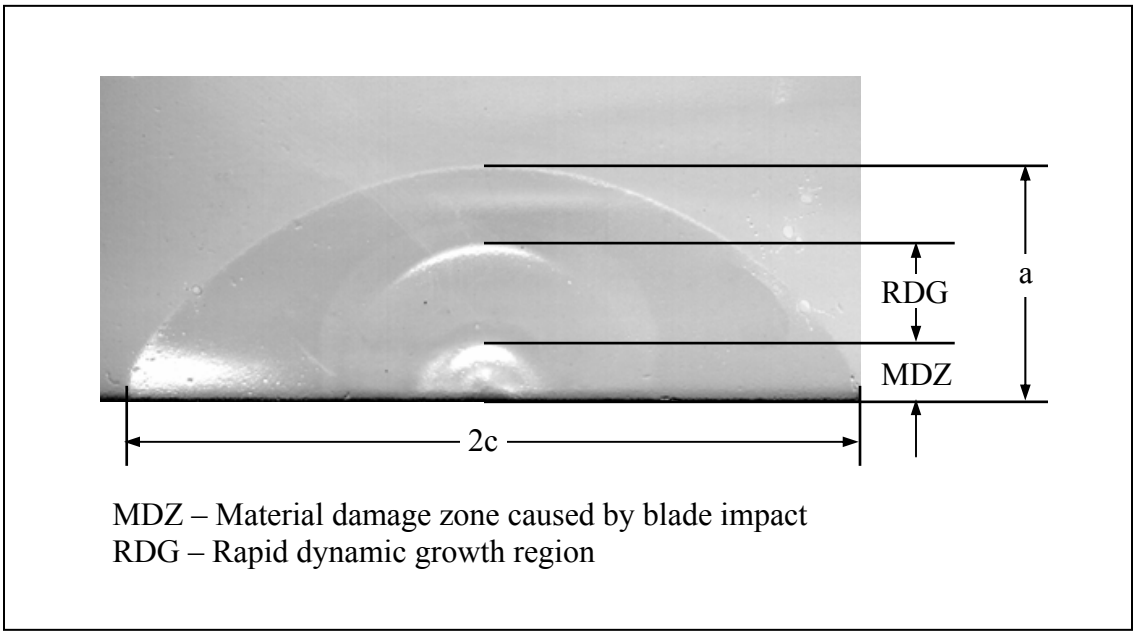

Figure 4.4: Typical semi-elliptic natural crack grown under pressure.

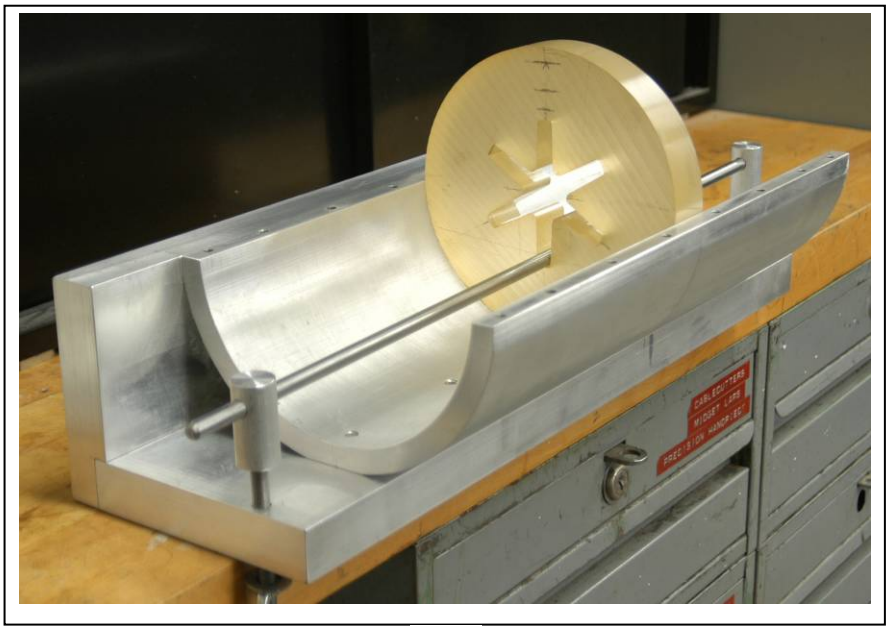

(a)

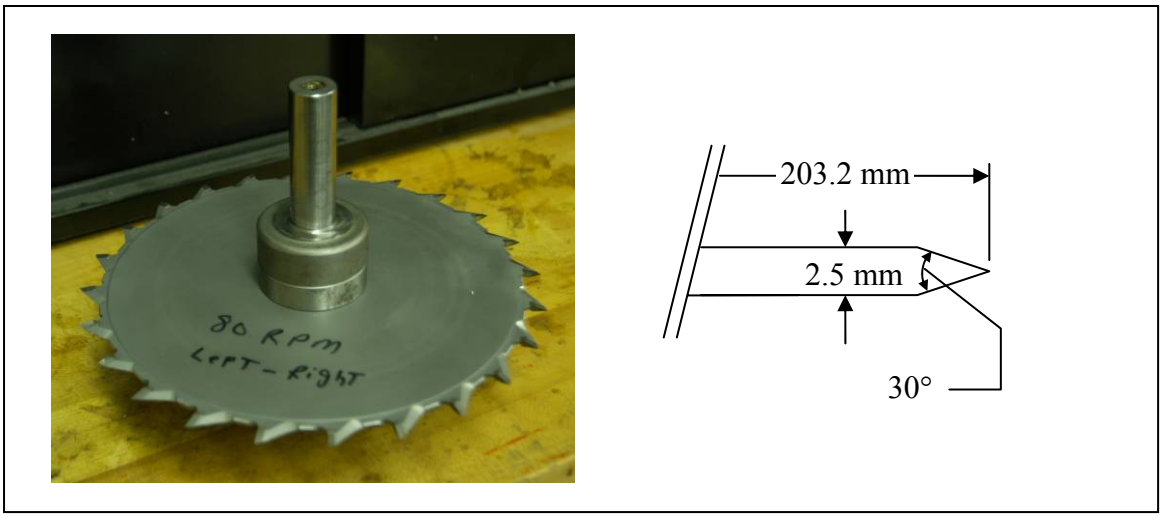

(b)

Figure 4.5: (a) Test fixture for machining and, (b) saw blade for making V-cut crack.

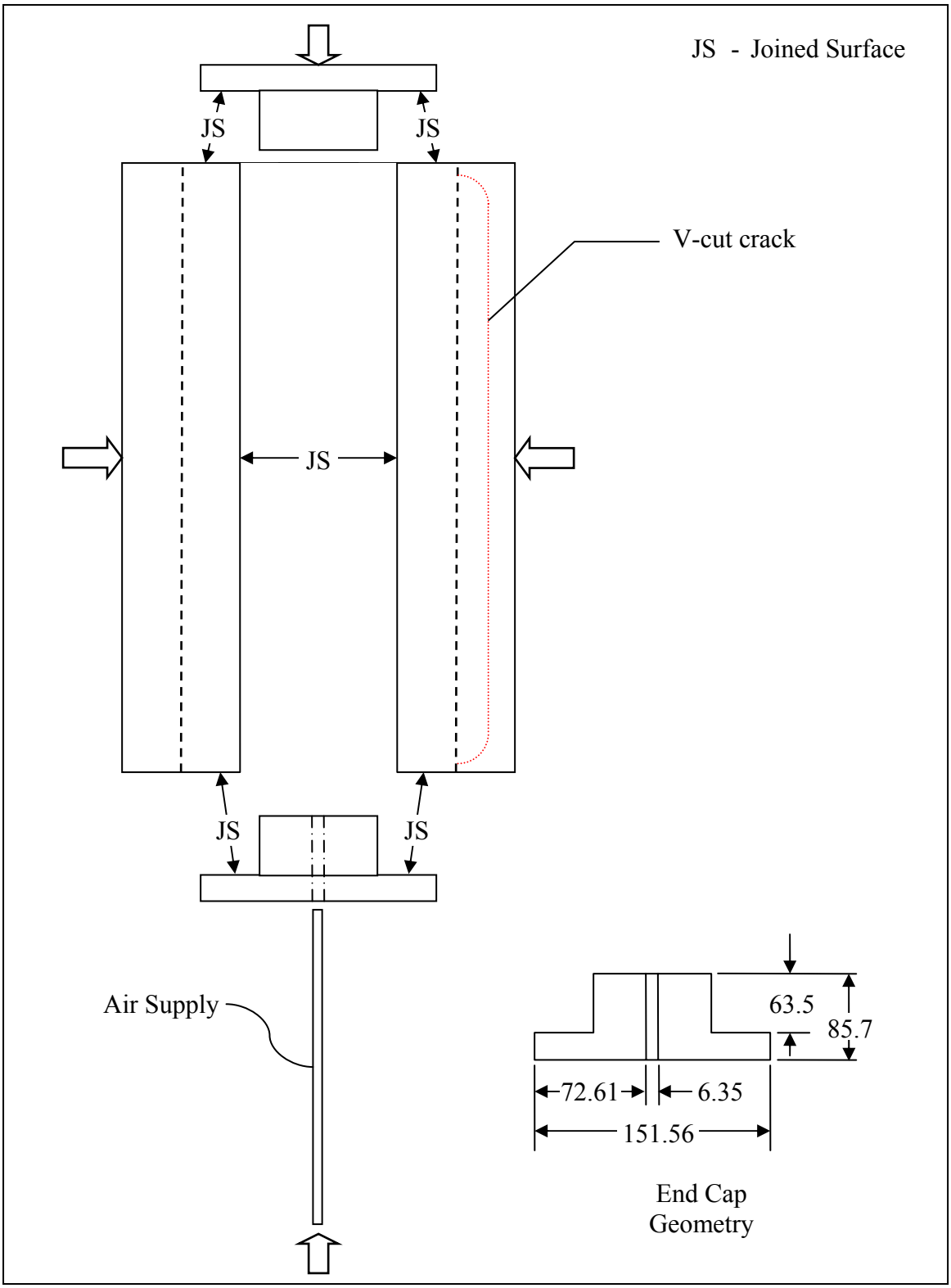

Figure 4.6: Schematic of the joining process for a V-cut specimen.

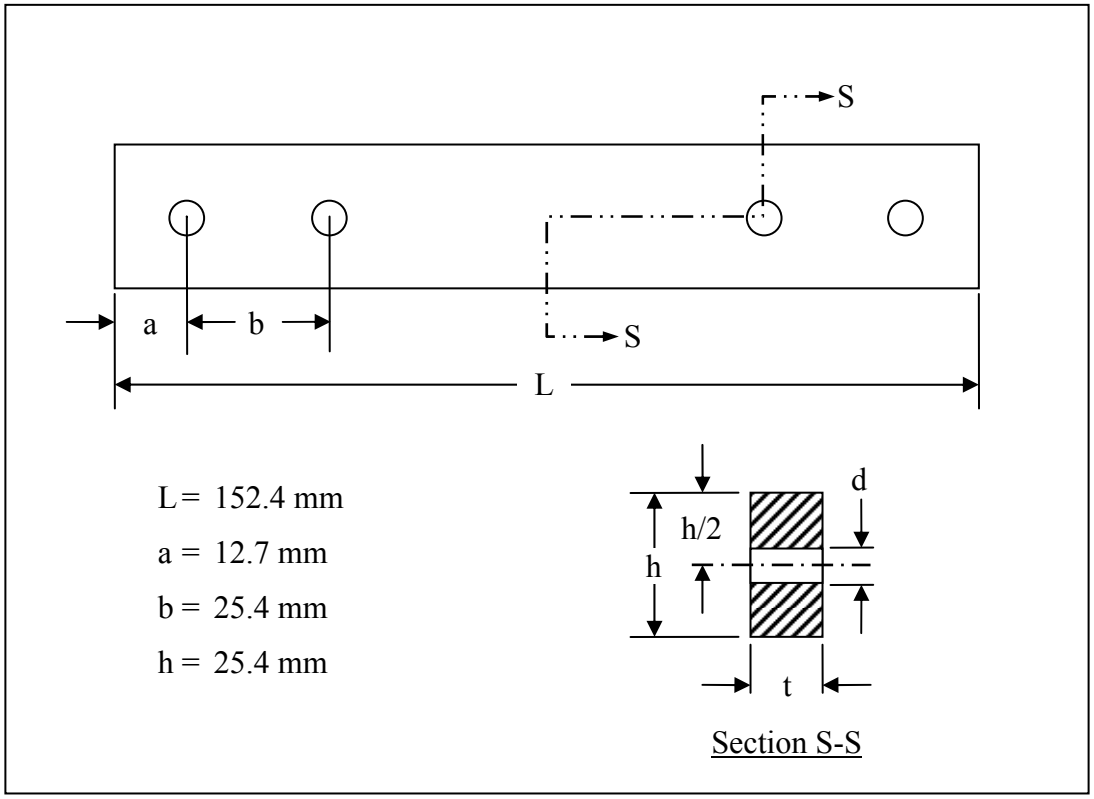

Figure 4.7: Schematic of calibration beam geometry.

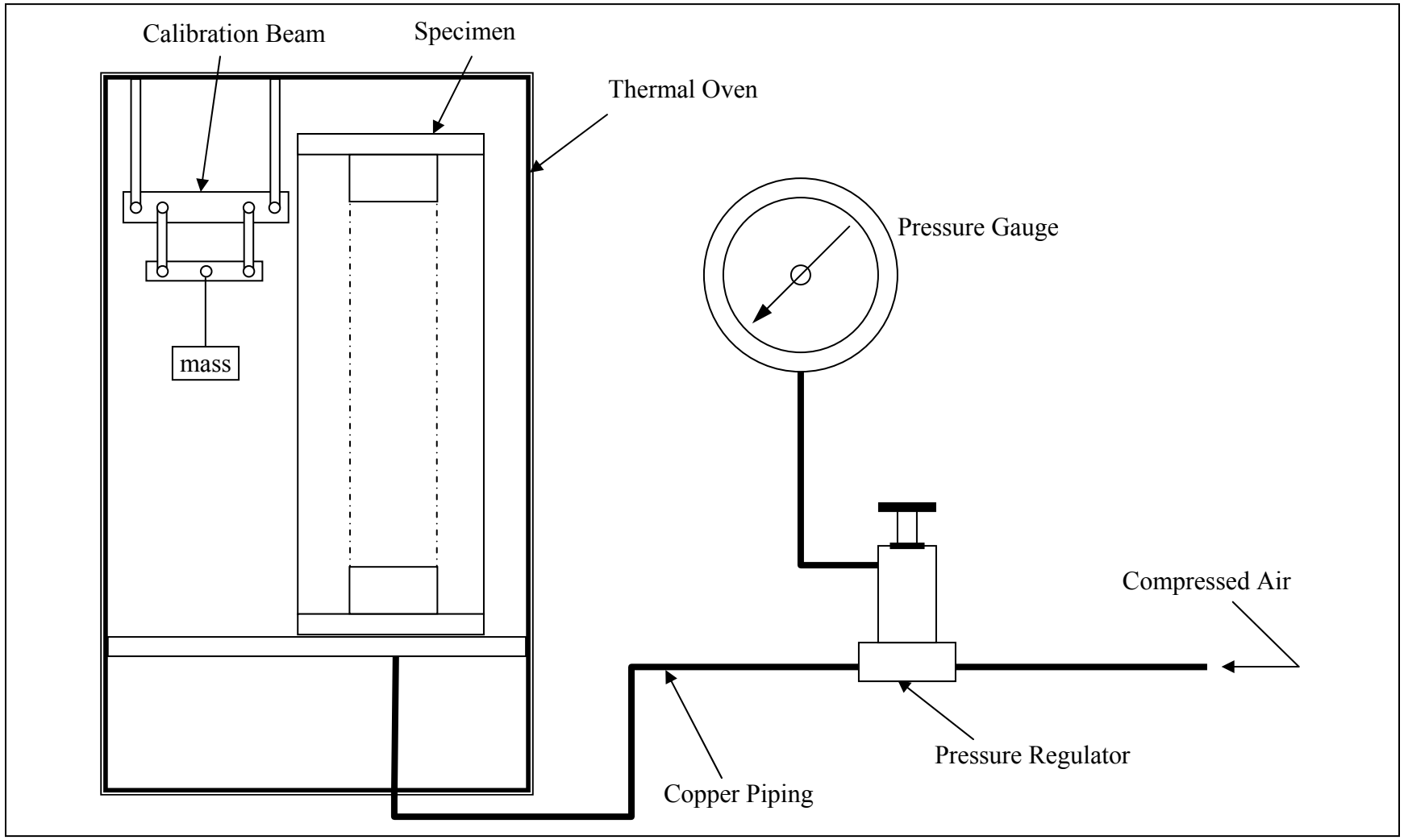

Figure 4.8: Schematic of the thermal oven setup.

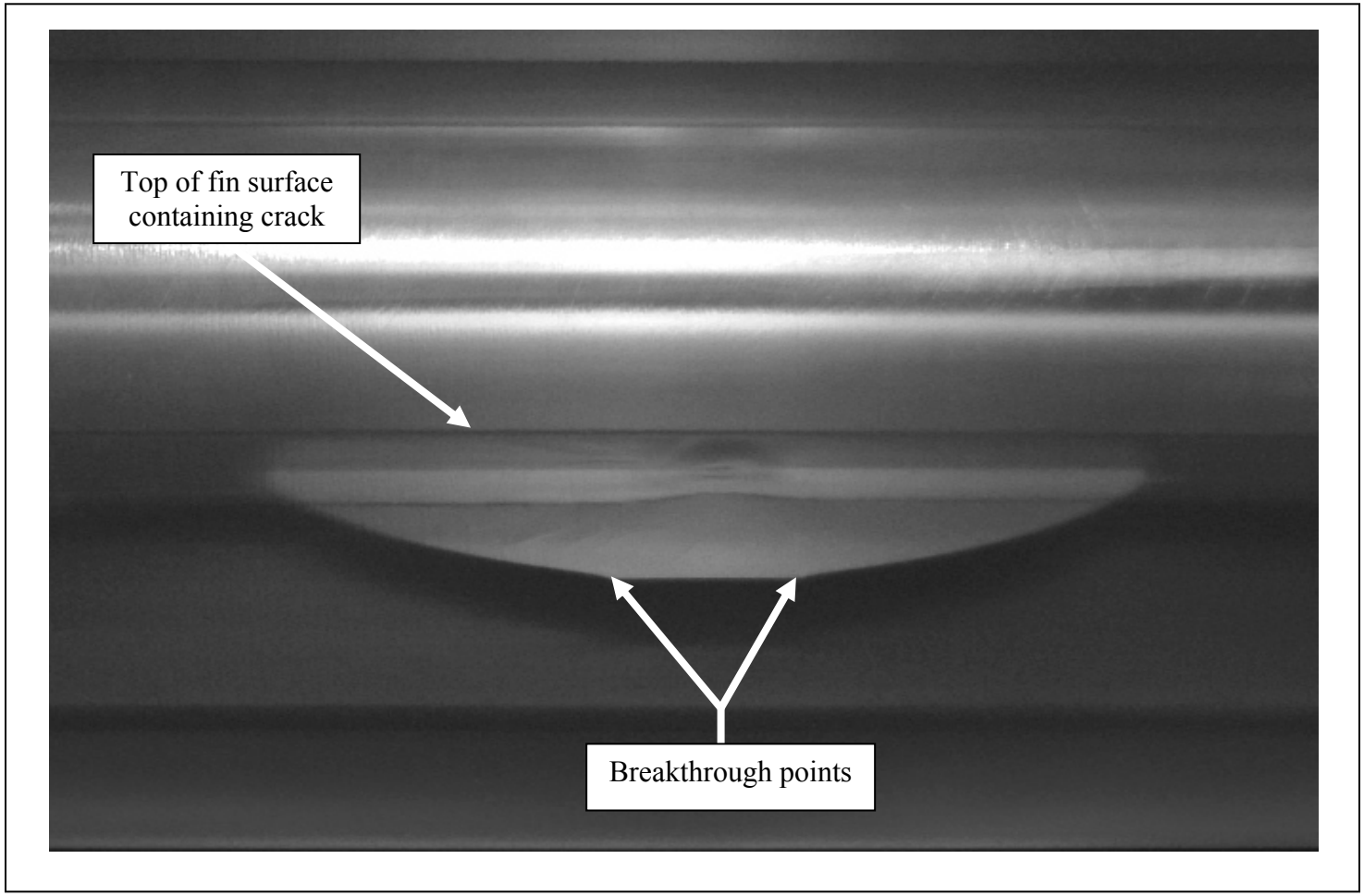

Figure 4.9: Specimen 3a crack growth and penetration showing breakthrough points.

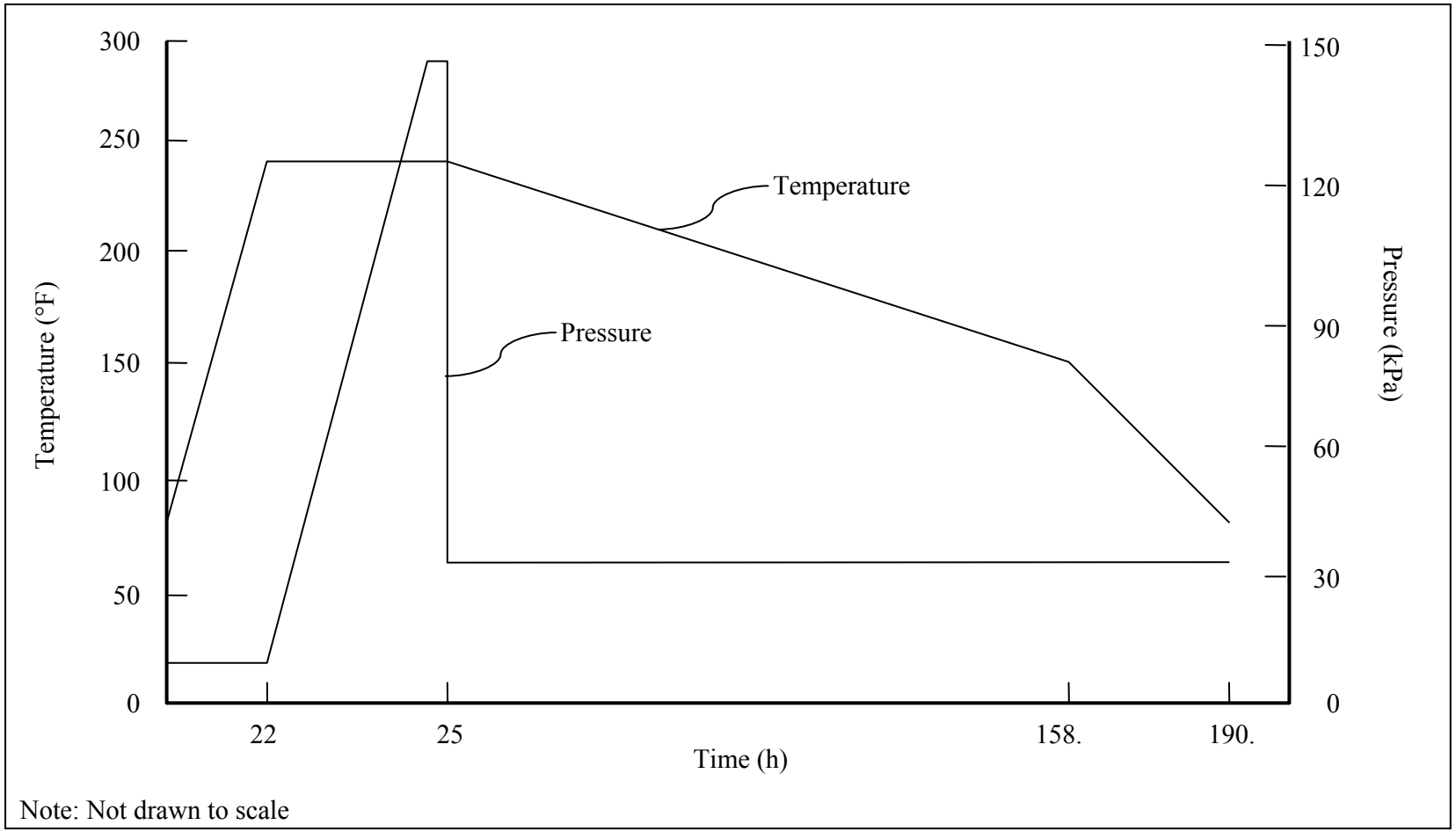

Figure 4.10: Typical Pressure and Temperature variations in the stress-freezing cycle, for a natural crack specimen.

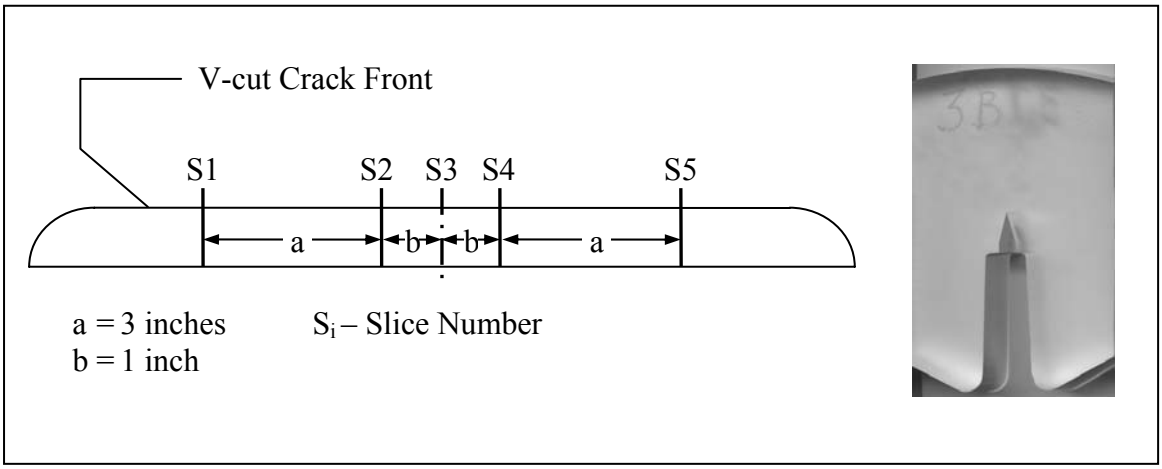

(a)

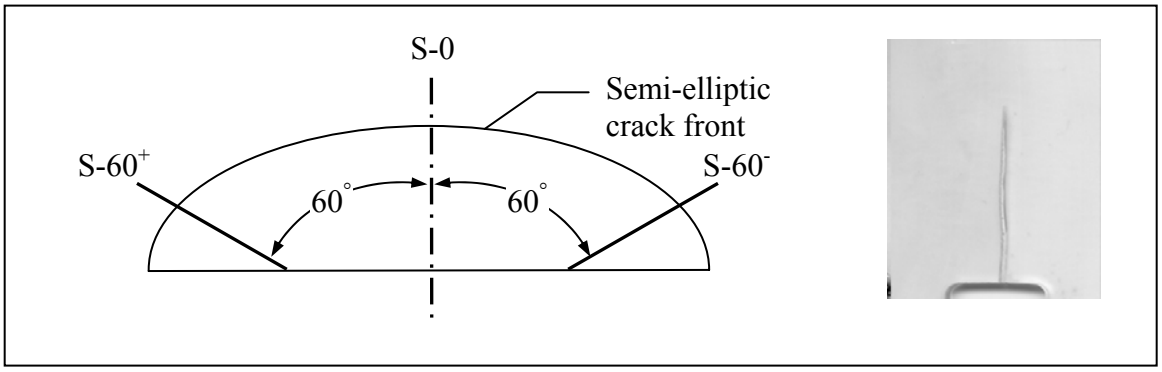

(b)

Figure 4.11: Slice extraction schematic for (a) V-cut crack and (b) natural semi-elliptic crack fronts including typical slice section pictures.

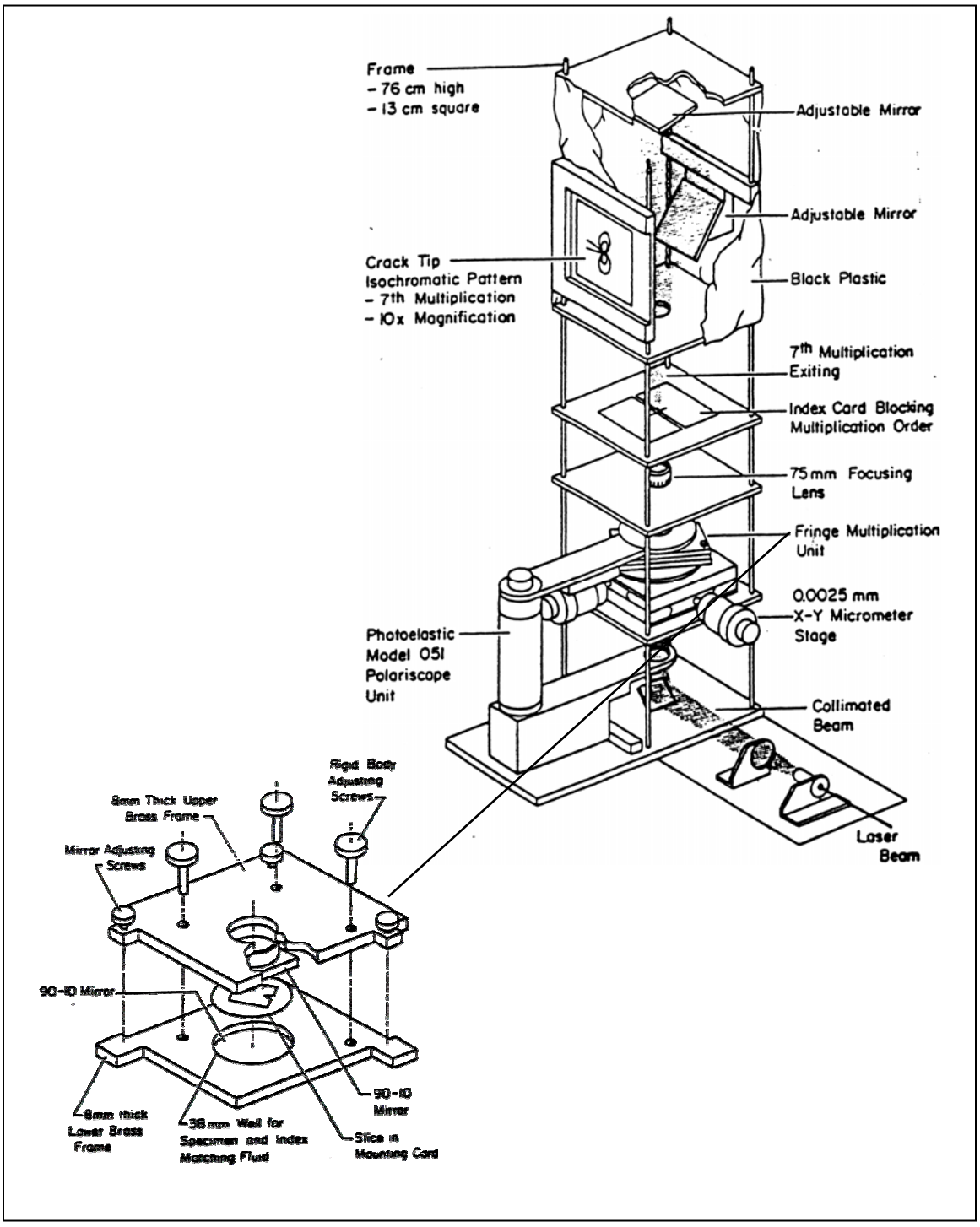

Figure 4.12: Refined polariscope with blowup of multiplication unit. (Adapted from a figure [Epstein, Post, and Smith 84])

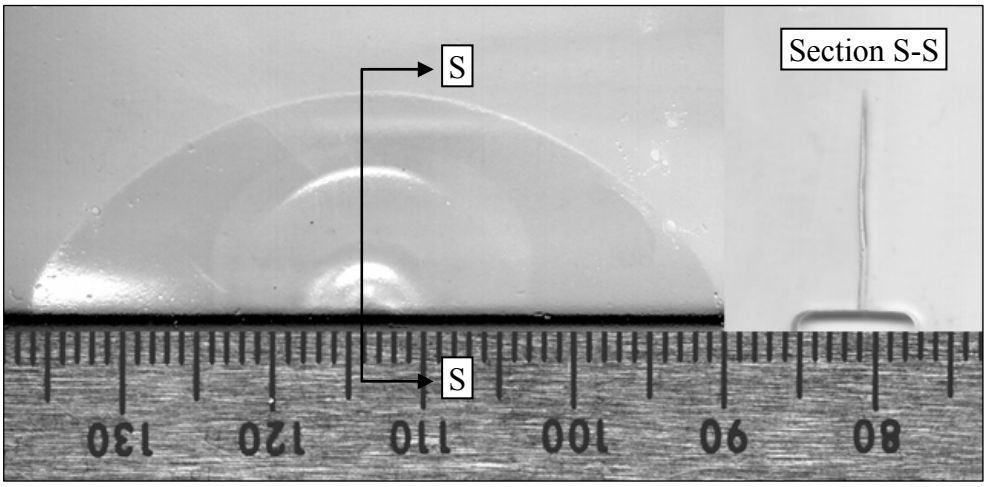

Figure 5.1: Photograph of a typical semi-elliptic crack profile and cross section.

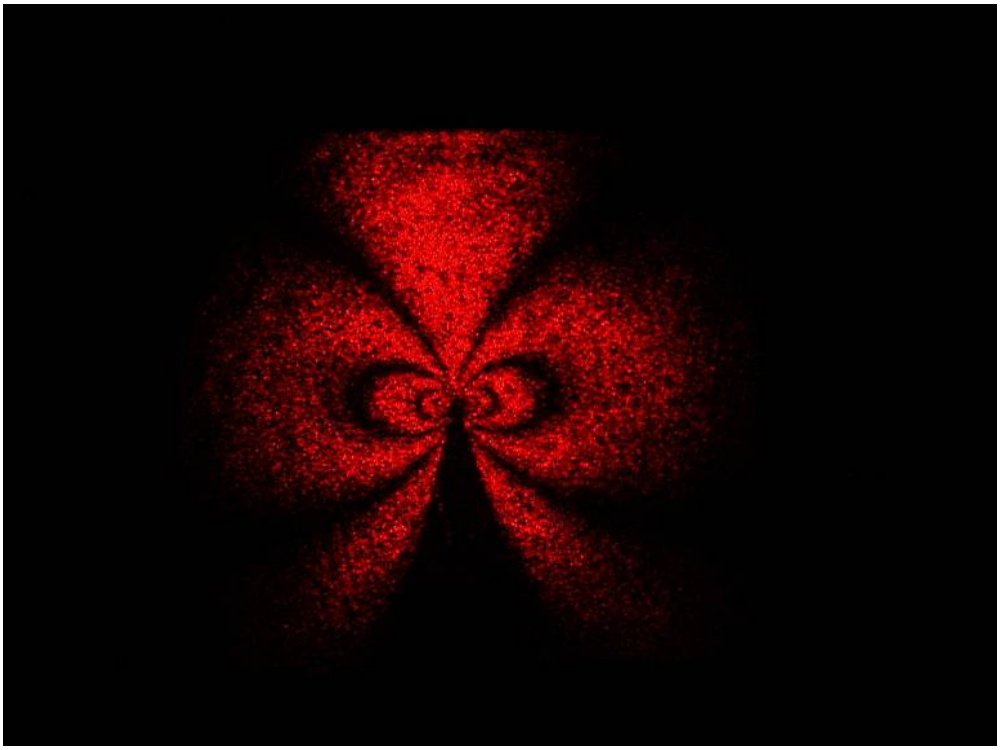

Figure 5.2: Typical fringe pattern of a V-cut specimen slice, Mode I loading only. The photograph was taken in a laser circular polariscope with no fringe multiplication.

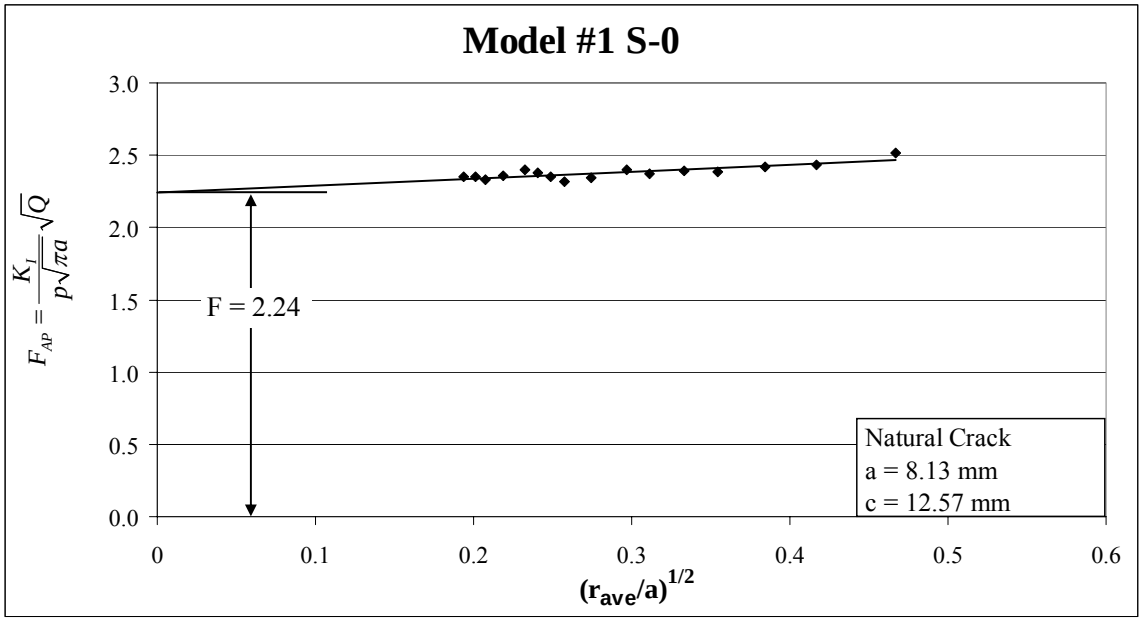

Figure 5.3: Typical plot of F_{AP} vs. $(r_{ave}/a)^{1/2}$.

Model 6
(Slice thickness = 4.29 mm)

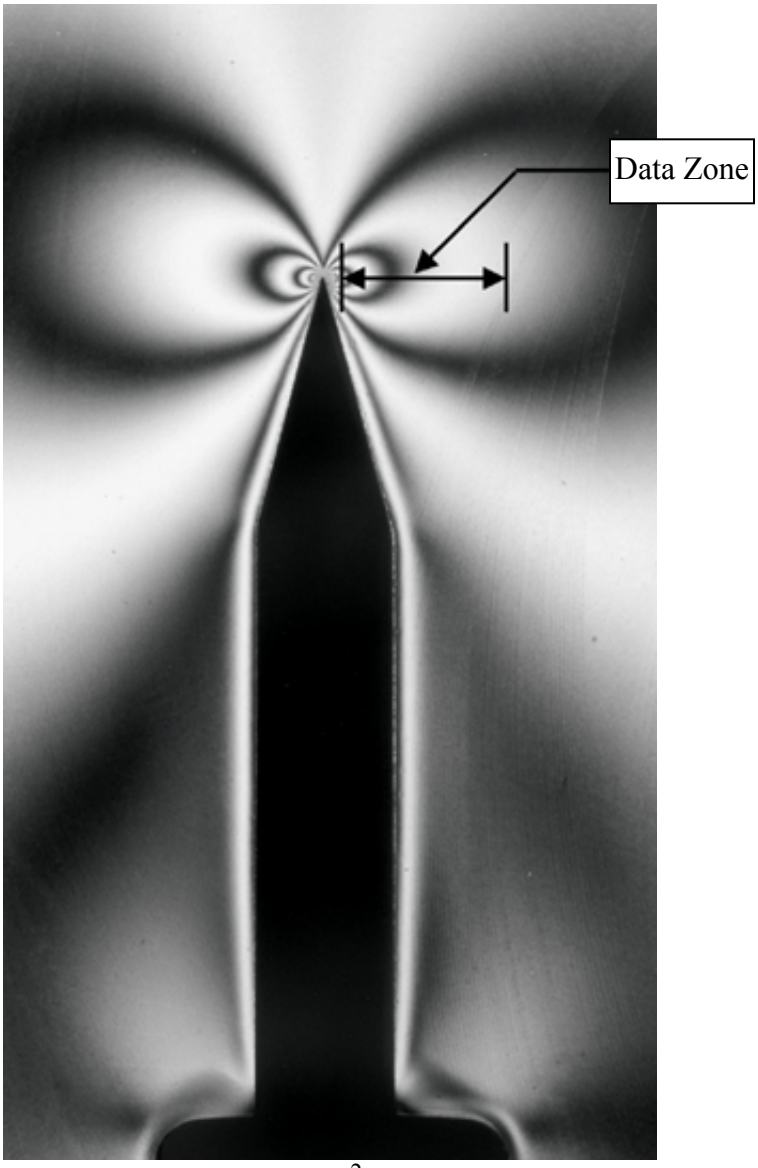

P_{sf}: 2.3×10^{-2} MPa
c: 175.30 mm
a: 19.6 mm
Data zone: $(r_{ave})_2 - (r_{ave})_1 = 4.2635 - 0.4564 = 3.807$ mm

Figure 5.4: Typical linear data zone for a V-cut slice.

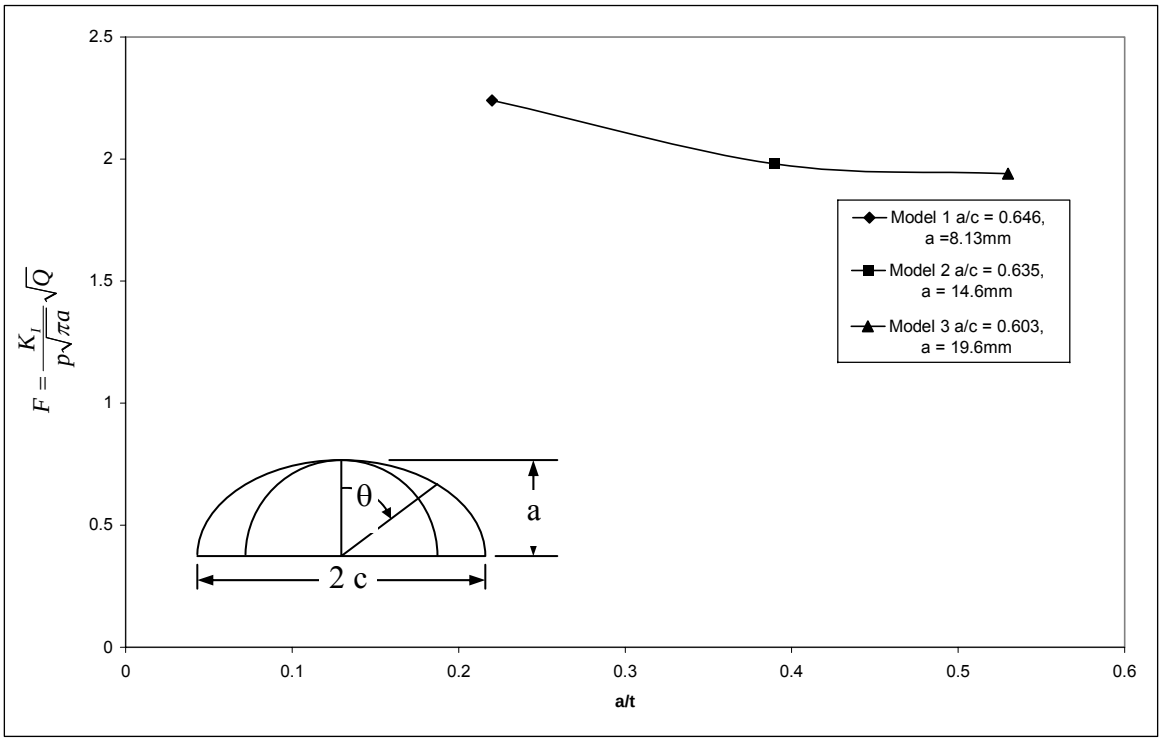

Figure 5.5: Variation of the normalized SIF for natural crack models 1-3 at the deepest point (θ = 0).

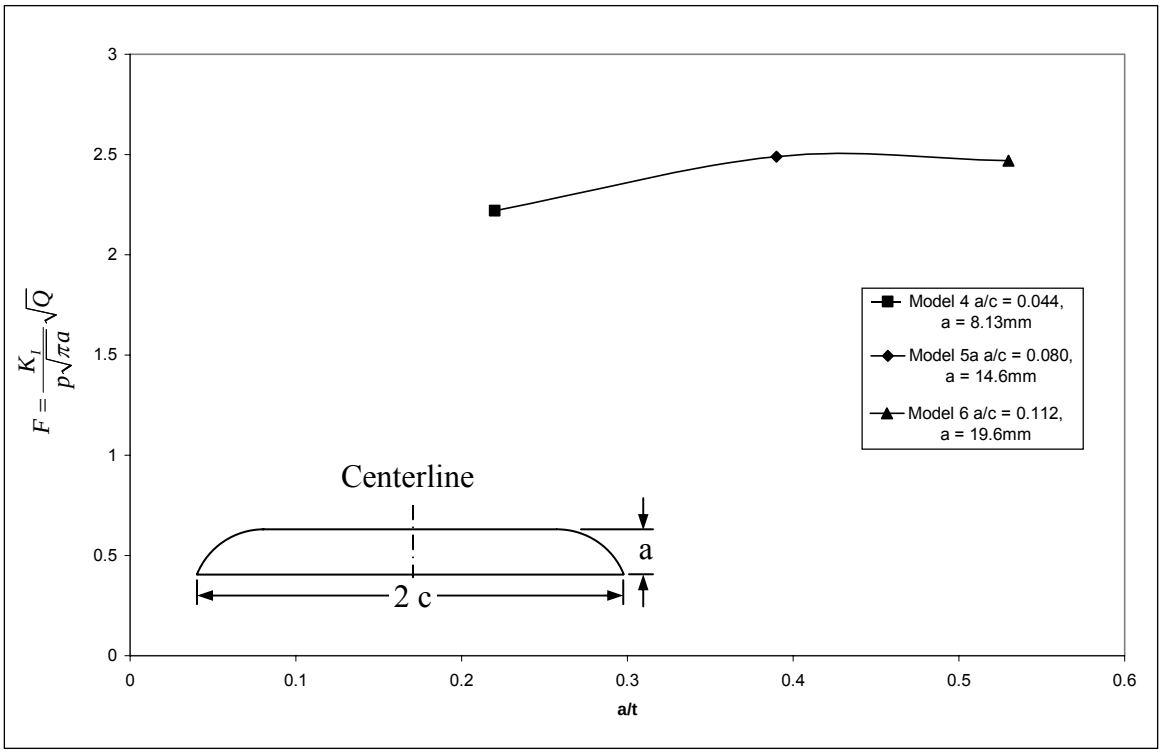

Figure 5.6: Variation of normalized SIF for V-cut models 4-6 at the centerline of the crack front.

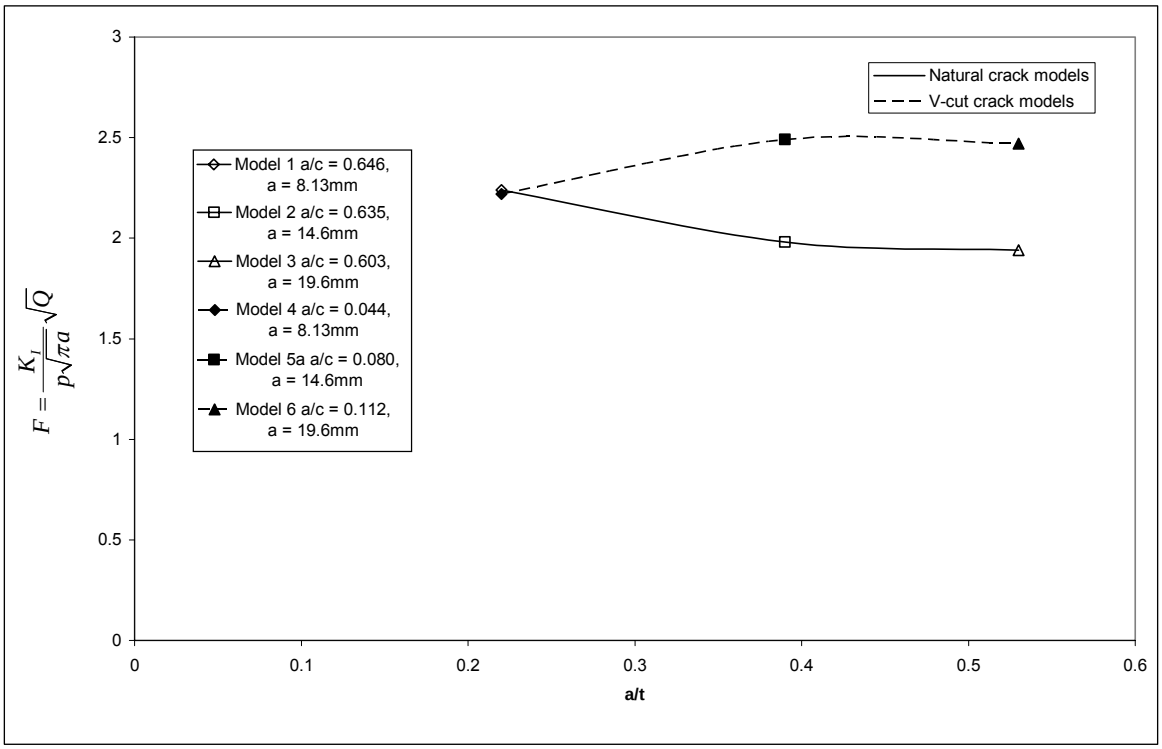

Figure 5.7: Normalized SIF for the natural and V-cut specimens at their centerlines.

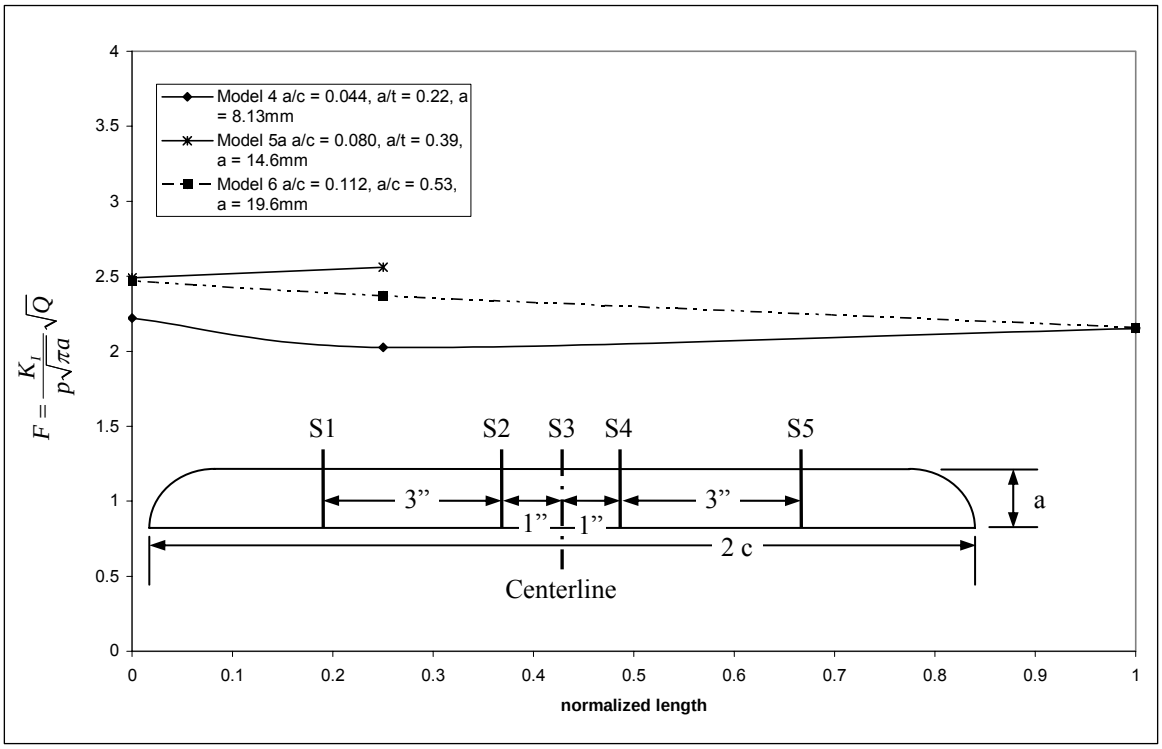

Figure 5.8: Variation of normalized SIF verses normalized length (distance from centerline divided by 4”) for V-cut crack models 4-6.

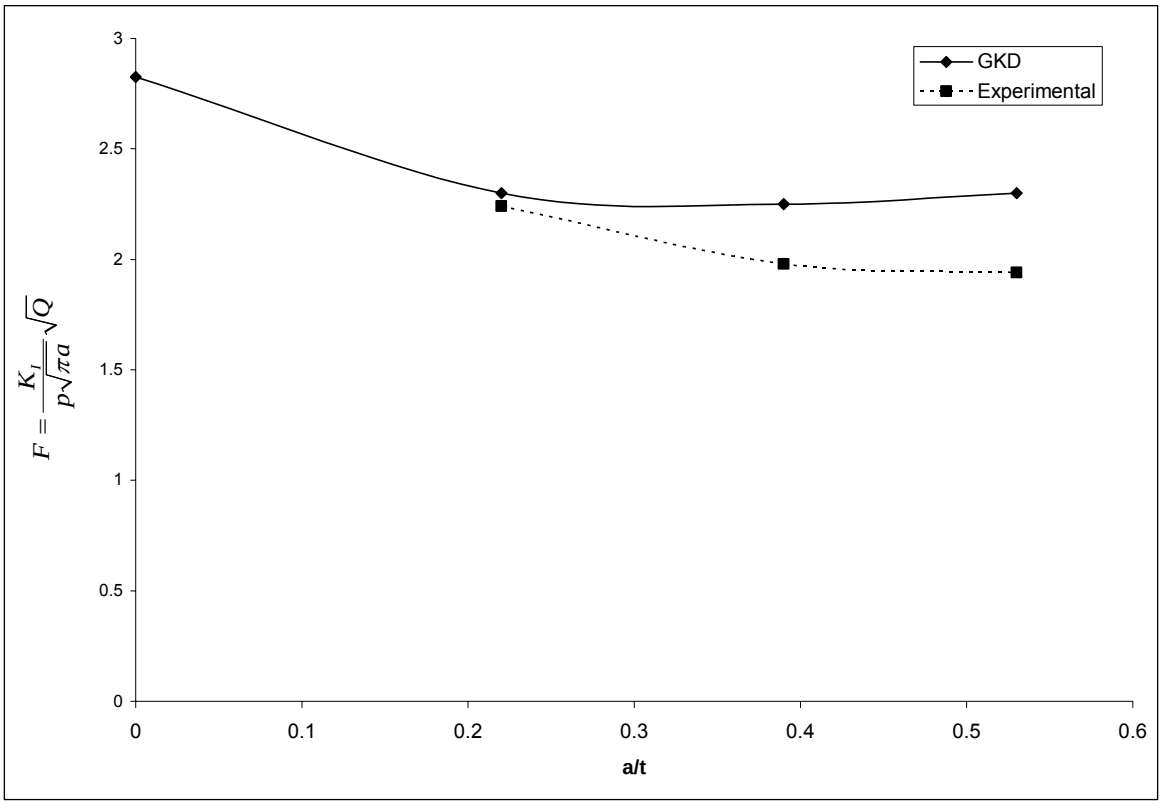

Figure 5.9: Normalized SIF for numerical data from semi elliptic cracks in circular cylinders (data from [Gouzhong, Kangda, and Dongdi 95])and experimental data from internal star cylinders with R_i/R_o = 0.5.

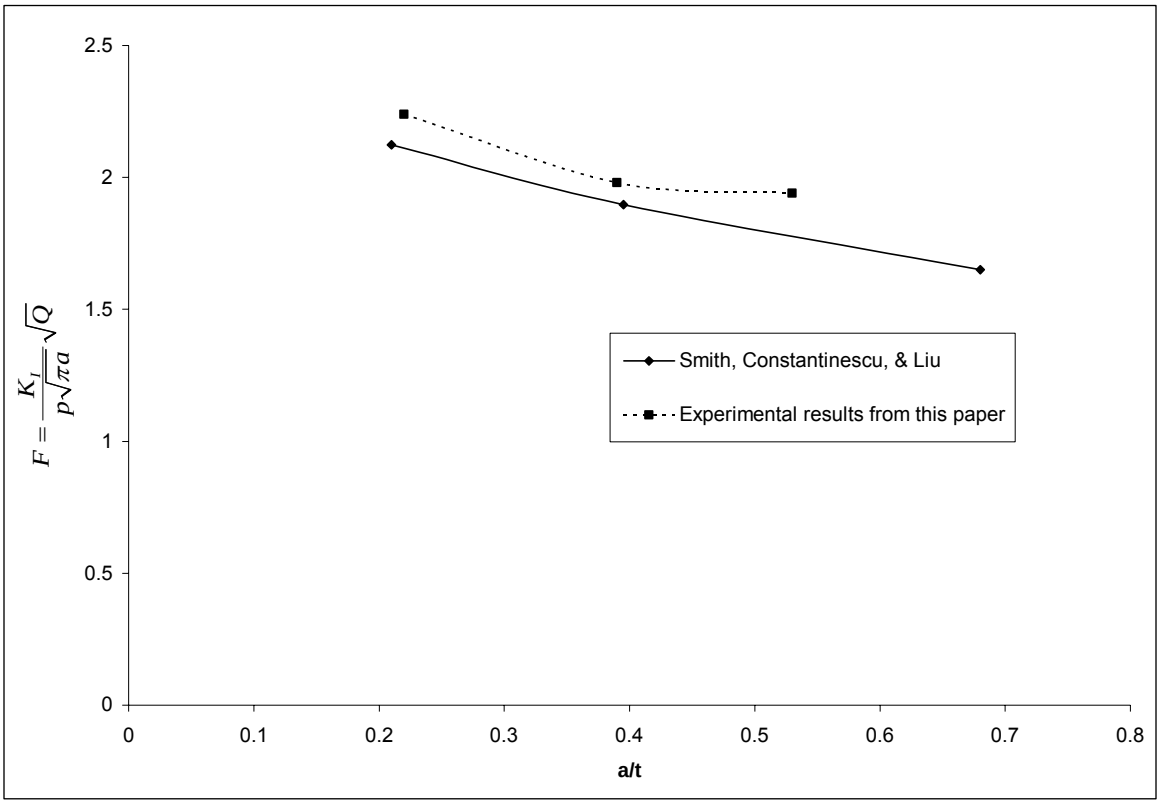

Figure 5.10: Comparison of experimental results from tests performed on internal star circular cylinders containing semi-elliptic cracks. Cracks were inserted off-axis parallel to the fin surface in the tests data from [Smith, Constantinescu, and Liu 02].

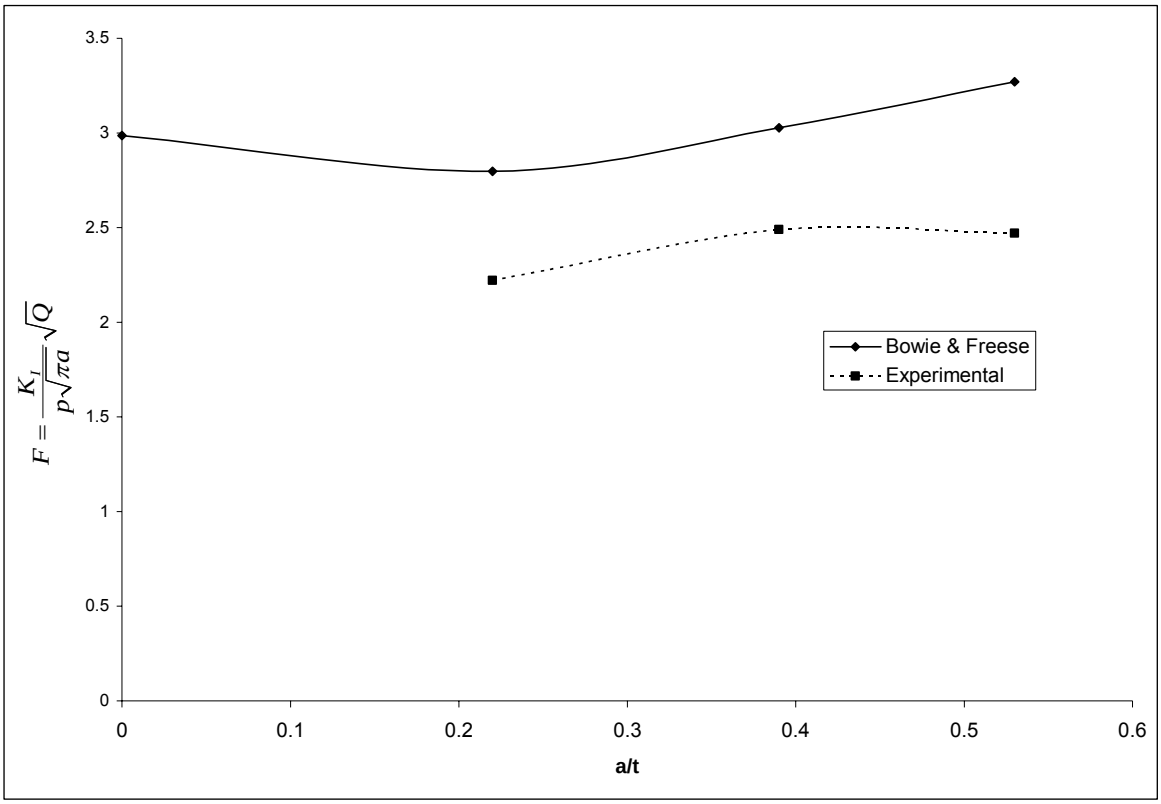

Figure 5.11: Normalized SIF for numerical data from long cracks in circular cylinders (data from [Bowie Freese 72]) and experimental data from long cracks in internal star cylinders with R_i/R_o = 0.5.

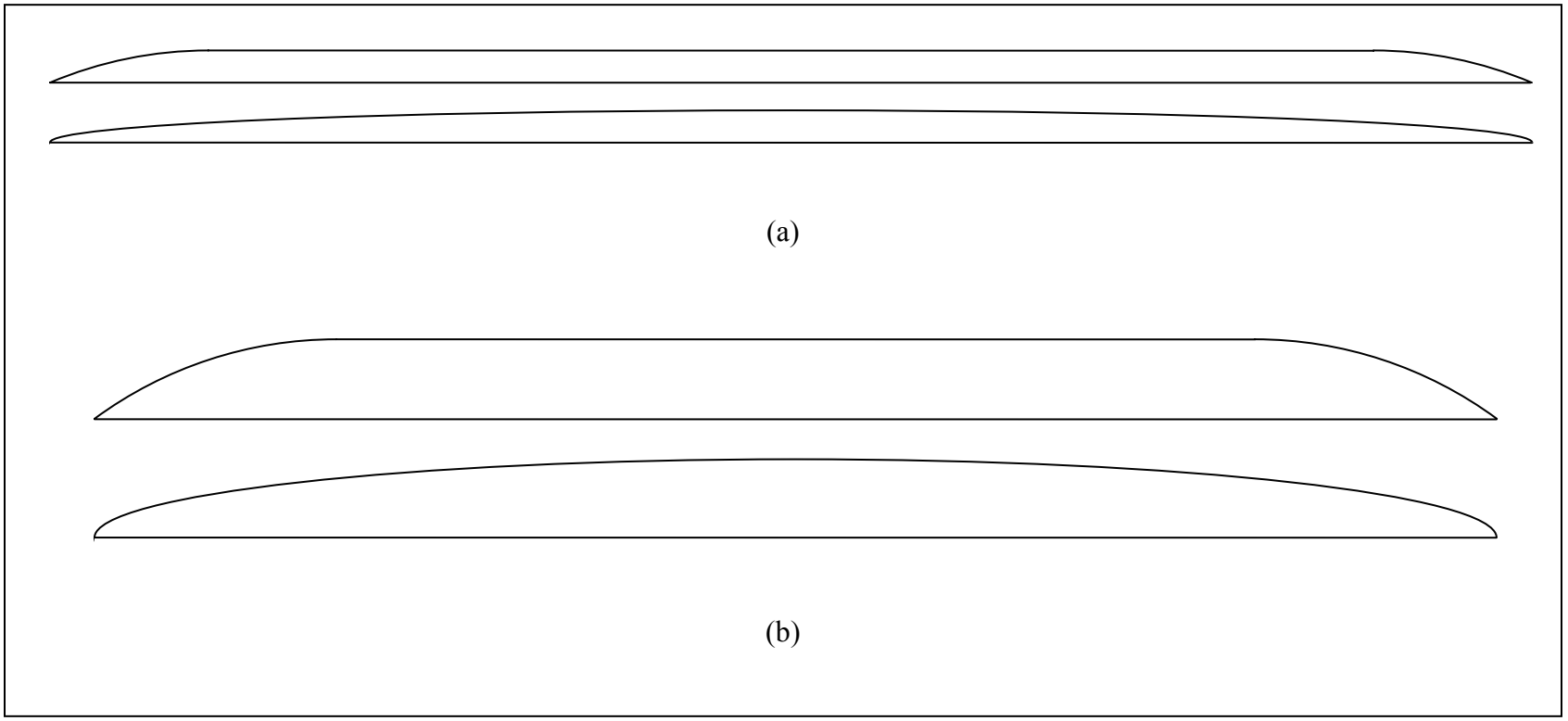

Figure 5.12: Actual (top) and semi-elliptic (bottom) cross-sections for (a) the shallow crack with a = 8.13mm and c = 184.8mm and (b) deep crack with a = 19.6mm and c = 175mm. Drawn to scale.

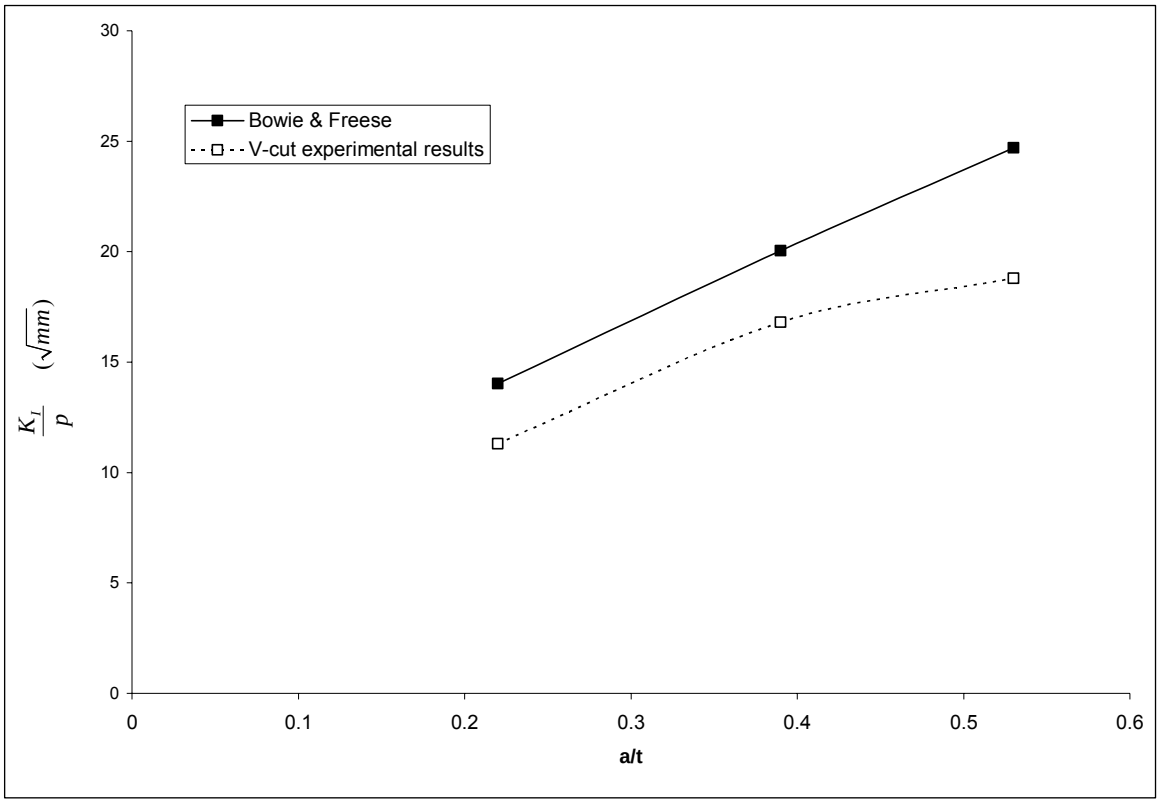

Figure 5.13: SIF with pressure normalized out for the experimental and numerical data from the long crack models (numerical data from [Bowie and Freese 72]).

Appendix B Tables

Table 2-1: Normalized stress intensity factors ($K_I / P\sqrt{\pi a}$)for semi-elliptical surface cracks in pressurized cylinders with R_o/R_i = 2, a/c = 0.8, and ν = 0.3.

α[1] (deg)	0	15	30	45	60	75	90
a/t \ $2\alpha/\pi$	0.0	0.167	0.333	0.5	0.667	0.833	1.0
0.2	1.617	1.604	1.588	1.565	1.565	1.604	1.782
0.3	1.55	1.546	1.532	1.515	1.528	1.613	1.707
0.4	1.492	1.473	1.469	1.455	1.481	1.573	1.684
0.5	1.477	1.45	1.447	1.432	1.468	1.551	1.677
0.6	1.49	1.48	1.46	1.463	1.473	1.582	1.703
0.7	1.523	1.511	1.48	1.457	1.47	1.576	1.727
0.8	1.623	1.607	1.582	1.526	1.52	1.536	1.669

Source: data in [Tan and Fenner 79]

[1] α is defined in Figure 2.3

Table 2-2: Normalized SIF, $F_I = K_I \Big/ \left(\left(pR_i/t \right) \sqrt{\pi a/Q} \right)$ for semi-elliptical surface cracks in pressurized thick-walled cylinders.

			ϕ (degree) defined in Figure 2.4					
t/R_i	a/c	a/t	5	15	30	50	70	90
1.00	0.25	0.2	1.589	1.734	2.002	2.276	2.434	2.474
		0.4	1.685	1.800	2.033	2.294	2.473	2.531
		0.6	1.807	1.891	2.112	2.440	2.737	2.853
		0.8	1.889	1.945	2.178	2.649	3.201	3.472
	0.50	0.2	2.070	2.037	2.112	2.263	2.363	2.397
		0.4	2.113	2.041	2.073	2.184	2.265	2.293
		0.6	2.278	2.156	2.156	2.271	2.384	2.432
		0.8	2.490	2.319	2.311	2.503	2.755	2.886
	0.75	0.2	2.434	2.347	2.303	2.327	2.359	2.373
		0.4	2.397	2.276	2.197	2.187	2.201	2.208
		0.6	2.496	2.331	2.219	2.200	2.220	2.231
		0.8	2.697	2.482	2.354	2.372	2.463	2.518

Source: data in [Gouzhong, Kangda, and Dongdi 95]

Table 2-3: Summary of the application ranges of the solutions to circular cylinders.

Name	a/t	a/c	t/R_i	Method	Crack Type
Glinka & Shen	0.0 – 0.8	0.2 – 1.0	0.5 and 0.25	WF	part-through
Atluri & Kathiresan	0.5 and 0.8	0.2 and 1.0	0.5 and 1.0	FEM	part-through
Raju &Newman	0.2 – 0.8	0.2 – 1.0	0.1 and 0.25	FEM	part-through
Tan & Fenner	0.2 – 0.8	0.8	1.0 and 2.0	BEM	part-through
GKD	0.2 – 0.8	0.25 – 1.0	0.5, 1.0, and 2.0	BEM	part-through
Kirkhope, Bell & Kirkhope	0.05 – 0.5	---	0.5 – 1.25	FEM	through
Yan & Dang	0 – 1.0	---	0.25 – 1.5	BEM	through
Bowie & Freese	0.1 – 0.9	---	0.25 – 1.5	BC	through

Ri - Inner Radius
Ro - Outer Radius
t - Ro-Ri
a - Crack Depth
c - Half Crack Length

WF - Weight Function
BEM - Boundary Element Method
FEM - Finite Element Method
BC - Boundary Collocation

Table 3-1: Possible arrangements of the circular polariscope.

Arrangement	Quarter-wave plates	Polarizer and analyzer	Field
1*	Crossed	Crossed	Dark
2	Crossed	Parallel	Light
3	Parallel	Crossed	Light
4	Parallel	Parallel	Dark

* Arrangement shown in Figure 3.1and used in ESM P&F Lab

Table 4-1: Mechanical Properties for PLM-4BR.

Temperature	Modulus of Elasticity, *E* ksi (GPa)	Stress Optical Constant, *"C"* psi/fringe/in (kPa/fringe/m)	Tensile Strength psi (MPa)	Coef. of Expansion PPM/°F (PPM/°C)	Poisson's Ratio ν
Room Temperature 72°F (22°C)	405 (2.8)	60 (10.5)	9000 (60)	39 (70)	0.36
Stress Freezing Temperature 180-210°F (82-99°C)	2.0 (0.014)	1.7 (0.31)	>200 (>1.5)	90 (162)	0.500

Source: data in [Measurements Group Inc. bulletin S-116-H, 92]

Table 5-1: Test Conditions and Crack Geometries.

Model name	P_{max} (kPa)	P_{sf} (kPa)	a (mm)	a/c	a/t	T_{sf} (°F)	f_σ (kPa/Fringe/mm)
1[+]	121	41	8.13	0.646	0.22	205	0.355
2[+]	129	46	14.6	0.635	0.39	205	0.357
3[+2]	167	28	19.6	0.603	0.53	200	0.355
4[*]	41	41	8.13	0.044	0.22	205	0.354
5[*]	41	41	14.6	0.080	0.39	205	0.356
6[*]	23	23	19.6	0.112	0.53	210	0.356

T_{sf} - Stress freezing temperature

f_σ - Material fringe constant

P_{max} - Maximum pressure

P_{sf} - Stress freezing pressure

a - crack depth

c - half crack length

t - distance between fin tip and cylinder wall

[+] Natural crack specimens

[2] Cylinder length 335.75mm

[*] V-cut crack specimens

Table 5-2: Results of stress intensity data for the three natural and four V-cut crack specimens.

Slice ID	M1-S-60$_{ave}$	M1-S-0	M2-S-60$_{ave}$	M2-S-0	M3-S-60$_{ave}$	M3-S-0
Linear Zone $(r/a)^{1/2}$	0.208-0.450	0.194-0.467	0.171-0.386	0.187-0.434	--	0.120-0.245
K_I	0.3415	0.358	0.506	0.473	--	0.329
F	2.14	2.24	2.11	1.98	--	1.94

Slice ID	M4-S1/5$_{ave}$	M4-S2/4$_{ave}$	M4-S3	M5-S1/5$_{ave}$	M5-S2/4$_{ave}$	M5-S3
Linear Zone $(r/a)^{1/2}$	0.284-0.493	0.194-0.471	0.223-0.544	--	0.182-0.523	0.176-0.601
K_I	0.447	0.421	0.463	--	0.709	0.689
F	2.15	2.025	2.22	--	2.56	2.49

Slice ID	M6-S1/5$_{ave}$	M6-S2/4$_{ave}$	M6-S3
Linear Zone $(r/a)^{1/2}$	0.136-0.543	0.227-0.471	0.153-0.466
K_I	0.378	0.415	0.432
F	2.16	2.37	2.47

Mi - Model number, 1-3 are natural crack models, 4-6 are V-cut crack models
S-x$_{ave}$ - Average data from location x which is defined in Figure 4.11
K_I - SIF
F - Normalized SIF

$$F = \frac{K_I}{p\sqrt{\pi a}}\sqrt{Q}$$

Table 5-3: Numerical and experimental normalized SIF corresponding to experimental geometry listed below with R_i/R_o = 0.5 evaluated at the centerline of the crack.

Model	a/c	a/t	$(F_I)_{Exp}$	$(K_I)_{Exp}$	$(F_I)_{BF}$	$(K_I)_{BF}$	$(F_I)_{GKD}$	$(K_I)_{GKD}$
1	0.646	0.22	2.24	0.36	2.77	0.57	2.34	0.37
2	0.635	0.39	1.98	0.47	2.99	0.93	2.25	0.54
3	0.603	0.53	1.94	0.33	3.17	0.70	2.27	0.39
4	0.044	0.22	2.22	0.46	2.77	0.57	2.70	0.56
5	0.08	0.39	2.49	0.69	2.99	0.83	2.65	0.73
6	0.112	0.53	2.47	0.43	3.17	0.57	2.70	0.48

Subscript key:

Exp - Experimental

BF - Bowie & Freese

GKD - Guozhong, Kangda, & Dongdi

Table 5-4: Experimental data with plane strain estimations for finned cylinders.

Model	a	a/c	a/t	$(F_I)_{EXP}$	$(F_I)_{BF}$	$(F_I)_{GKD}$	$(F_I)_{PSE}$
1	8.13	0.646	0.22	2.24	2.77	2.34	2.65
2	14.6	0.635	0.39	1.98	2.99	2.25	2.63
3	19.6	0.603	0.53	1.94	3.17	2.27	2.71
4	8.13	0.044	0.22	2.22	2.77	2.70	2.28
5	14.6	0.08	0.39	2.49	2.99	2.65	2.81
6	19.6	0.112	0.53	2.47	3.17	2.70	2.90

$(F_I)_{EXP}$ - Experimental results for finned models

$(F_I)_{BF}$ - Bowie Freese's plane strain solution to a long crack in a circular cylinder

$(F_I)_{GKD}$ - GKD's solution to a semi-elliptic crack in a circular cylinder

$(F_I)_{PSE}$ - Plane strain estimation for long cracks in finned models